THE EFFECTS OF STRUCTURE AND COMPOSITION ON THE HARDNESS OF BIOGENIC AND SYNTHETIC SINGLE CRYSTAL CALCITE

A Dissertation

Presented to the Faculty of the Graduate School

of Cornell University

In Partial Fulfillment of the Requirements for the Degree of

Doctor of Philosophy

by

Miki Eugene Kunitake

August 2015

THE EFFECTS OF STRUCTURE AND COMPOSITION ON THE HARDNESS OF BIOGENIC AND SYNTHETIC SINGLE CRYSTAL CALCITE

Miki Eugene Kunitake, Ph. D.

Cornell University 2015

Biologically controlled minerals are often intimately associated with occluded organic components that regulate composition and morphology, and induce complex hierarchical structures. This integration of strong but brittle inorganic with tough but compliant organic also enables these hybrid tissues to have remarkable mechanical properties considering the starting materials. Unfortunately, this complexity also makes is difficult to isolate the individual effects of structure and composition on the mechanical response of the system.

Here, we develop methods using synthetic mineralization to examine the effects of crystallographic orientation and additive content, on the hardness of single crystal calcite to gain insight into biomineralization. Using quasistatic depth sensing nanoindentation, we compare the hardness of synthetic calcite crystals incorporating magnesium, amino acid, or agarose additives to biogenic calcite from the prismatic layer of the mollusk *Atrina rigida* and geologic calcite in the form of Iceland spar.

The hardness of single crystal calcite on the (001) face, varies with azimuthal angle; about 7% for Iceland spar and 20% for biogenic calcite. Additionally, this range in hardness increases with higher additive content. Hardness also increases by 30, 70 and 20% by adding magnesium, amino acids, and agarose polysaccharides,

respectively, equaling the ~70% difference between biogenic and geologic calcite. Hardness can be reduced by thermal decomposition of the polysaccharide reinforcement, though the final hardness is still greater than pure geologic calcite.

The variations in hardness with azimuthal angle and additive content are consistent with a hardening mechanism based on hindered dislocation motion.

BIOGRAPHICAL SKETCH

Miki Eugene Kunitake was born in 1978 to Eugene and Yutaka Kunitake in San Antonio, Texas. He learned resourcefulness from his Mother, born in 1937 in Japan, and creativity from his Father, a farmer from Hawaii turned Navy dentist. During his childhood, his parents limited television time to two hours a week, shared between his two elder siblings, Hiroko and Koichi. It was probably because his siblings chose MacGyver and Mission Impossible as the two TV shows, that he enjoyed trying to design experiments from scratch, and began an education focused on chemistry. During the other 166 hours that he was not watching television, he was encouraged to dig holes in the ground for composting, practice the piano, and hit rocks into the canyon with a baseball bat.

In 1996, he began his undergraduate studies at Yale University, where he studied the in-situ crystallization of benzoin crystals under J. Michael McBride, graduating with a B.S. in chemistry in 2000. He also continued his joy of hitting things with a bat by playing on the graduate summer softball team. Here, he met Lara Estroff, a chemistry graduate student, and future thesis advisor.

After graduation, he changed directions and went into the Navy for four years to teach thermodynamics and reactor principles to enlisted nuclear power students, eventually becoming division director of the thermodynamics division for one year. However, he knew that he would like to go back into research, and so applied to UC Berkeley's chemistry program in 2004. Though after two years studying the energetics of electrons during gas phase catalysis under Gabor Somorjai, and silicon nanowire growth under Peidong Yang, he was unable to make any breakthroughs, and left with a master's degree.

Coincidentally though, Lara Estroff had started up a research lab at Cornell in

2006, and having heard of this, he applied to the materials science and engineering program starting in the summer of 2007. He began a project in collaboration with Shefford Baker that combined his childhood hobby of digging holes with his academic background in crystal growth, and began making nano-indents in synthetic and biogenic calcite.

After graduation, he will begin a glass process engineering job at Corning, and hopefully, find more softball teammates.

Dedicated to Mom and Dad

ACKNOWLEDGEMENTS

I really appreciate the collaborative spirit found at Cornell. There have been so many professors, colleagues and friends with whom I discussed scientific questions and whose wisdom has guided my research. I am really thankful for their perspectives.

First, I would like to thank my advisor Professor Lara Estroff. She gave me a home from which I could explore research directions. Whether it was by networking through Gordon conferences or research collaborations around the world, I always felt welcome to think about scientific experimental possibilities and ask for the advice of other researchers. I would also like to thank her for her insight and breadth of knowledge in guiding my research.

I would like to thank Professor Shefford Baker for his support in helping me learn nanoindentation and mechanical testing. Additionally, his organizational clarity and meticulous grammar have pushed me to be a better writer. I am sorry that I've made your red pen cry so much ink!

I would like to thank Cornell for establishing the Cornell Center for Materials Research (CCMR). Because of this facility, I was able to use shared instruments and ask colleagues and facility managers about parameters, techniques, and experiments used to improve my own research. In particular, I'd like to thank John Hunt, John Grazul, Kit Umbach and Mick Thomas for their expertise and for pointing me in the direction of other facility users, who could give me even more detailed advice.

I am grateful for my labmates for all the smiles that I have had in these 5 and a half years. Hanying Li, Jason Dorvee, and Ellen Keene for their mentorship. Hanying for his charismatic enthusiasm and insight that encouraged me to continue seemingly failed experiments and Jason and Ellen for their no-nonsense viewpoints. Amy Richter, Ruiqi Song and Emily Asenath-Smith and Jennie Russ for shared office banter and time. I would like to thank John Peloquin and Lauren Mangano, two

extraordinary undergraduates who have helped extend and solidify my own understanding of this research.

Finally, I would like to thank my family and friends: My father Eugene for his experimental creativity that inspires me to think outside the box, and my mother Yutaka, for teaching me resourcefulness. My sister Hiroko, for always watching out for me, and my brother Koichi, for encouraging me to strive forward. I would like to thank my fiancée Jennie Russ for her patience with me. I would like to thank Alwin Wan for his considerate humor as housemate, biking colleague and sounding board. Grace Kim and Melissa Takahashi, for their good taste in clothing and restaurants. Anna Legard and Brendan Murday for their organizational skills and for bringing together the department socially, and all my intramural teammates, especially Chile Lindo.

TABLE OF CONTENTS

LIST OF FIGURES

LIST OF TABLES

LIST OF ABBREVIATIONS

Asp	Aspartic Acid
$CaCl_2$	Calcium Chloride
$CaCO_3$	Calcium Carbonate
CCMR	Cornell Center For Materials Research
Cys	Cysteine
EBSD	Electron Backscatter Diffraction
ESRF	European Synchrotron Radiation Facility
GPa	GigaPascal
Gly	Glycine
HRTEM	High Resolution Transmission Electron Microscopy
HPLC	High Performance Liquid Chromatography
ICP-AES	Inductively Coupled Plasma Atomic Emission Spectroscopy
MPa	MegaPascal
μm	Micrometer
μN	MicroNewton
nm	Nanometer
SEM	Scanning Electron Microscopy
TGA	Thermogravimetric Analysis
WDS	Wavelength Dispersive Spectroscopy

LIST OF SYMBOLS

H	Hardness
E_{it}	Indentation Modulus
β	Indenter Specific Geometry Parameter
π	Pi
ν	Poisson's Ratio
A_c	Projected Contact Area
E_r	Reduced Modulus
S	Stiffness
σ_y	Yield Strength

CHAPTER 1

1 INTRODUCTION TO MECHANICAL PROPERTIES OF BIOGENIC CRYSTALS

1.1 Introduction

The relationships among composition, structure, and mechanical properties may help us understand not just why biominerals have remarkable mechanical properties, but how biomineralization is able to create these materials, enabling us to create synthetic mimics. Single crystal biominerals often contain a diverse range of impurities, from single atoms to proteins and polymers, that make them tougher and stronger than their pure geologic counterparts. However, these additives, found chemically and physically associated within the inorganic crystal, also alter the microstructure of the growing biomineral, inducing complex heirarchical structures with distinct crystallographic orientations. This intimate integration of organic and inorganic enables these hybrid tissues to have remarkable mechanical properties considering the starting materials.[1-3] Unfortunately, it is also this complexity that makes it difficult to isolate the individual effects of composition and structure on the mechanical response of the system.

There have been many studies examining the remarkable mechanical properties of biomineralized tissue. Within the subset of biominerals containing calcium carbonate: Mother of pearl has been measured to be thousands of times tougher than geologic aragonite.[4-6] The queen conch is 300 times tougher with a structural design incorporating five different length scales.[7, 8] Abalone shells are an "unusual combination of high strength, hardness and toughness."[9, 10] Bivalves and brachiopods demonstrate increased nanoindentation hardness attributed to inter- and intracrystalline organic[11] and

microstructure.[12, 13] Only in the case of the sea urchin spine is there information about the mechanical properties of a single crystal biomineral, though even in this case, other factors such as crystallinity and porosity have influenced the conclusions.[14, 15] The remarkable mechanical properties of these biomineralized systems are often attributed to the complex combination of organic and inorganic as well as micro- and macrostructure. However, it is also this complexity that makes it difficult to quantify the mechanical properties of the individual single crystal biominerals that comprise the tissue. Are the mechanical properties of the single crystal also remarkable?

This thesis takes a two-fold approach to understanding the individual effects of composition and structure on the hardness and modulus of the biomineral calcite. The first step involves the synthesis of single crystal calcite containing a range of additive sizes and concentrations. The second step involves quantitative measurement of these samples by depth sensing nanoindentation. By isolating and quantifying the effects of composition and structure, we can then evaluate whether strengthening mechanisms found in the metallurgical field can also be used to explain the increased strength and toughness of biominerals.

Calcium carbonate ($CaCO_3$) is found in a variety of organisms: Algae, such as *Emiliania huxleyi*, which use calcite as a protective shell, have reproductive blooms of such magnitude that they influence the global CO_2 content.[16, 17] Mollusks are capable of simultaneously producing two different crystal structures (polymorphs) of calcium carbonate, aragonite in an inner nacreous layer and calcite in an outer prismatic layer with both layers often aligned such that the carbonate groups are parallel to the shell surface.[18, 19] The polycrystalline calcite eggshells of birds and dinosaurs share a

crystallographic growth direction as well as an interruption in preferred orientation. These similarities have been used to distinguish their eggshells from the calcite found in crocodile eggshells.[20] Calcite is also found in otoconia located in mammalian inner ears; it is integrated within a fibrous organic matrix that transfers forces to a nervous system, enabling us to maintain balance and stability.[21, 22] All of these evolutionarily successful and mechanically robust examples combine organic components with inorganic calcite. While there are many diverse biomineral systems, we studied calcite as a model to gain insight into how compositional and structural variations affect the mechanical properties of biominerals.

In this thesis, I first examine the structure-property relationship by quantitatively examining the effect of crystallographic orientation on the mechanical properties of single crystal calcite. Next, I examine the composition-property relationship by synthesizing and measuring single crystal calcite containing magnesium, amino acid,[a] or agarose fiber additives, which span a range of chemical and structural size differences. Finally, I examine the structure-composition-property relationship by measuring crystals where the agarose fibers have been thermally decomposed into voids within the single crystal. These results are compared with biogenic calcite from the mollusk *Atrina rigida*, in order to investigate the strengthening mechanisms found in biominerals.

1.2 Background on Calcite

At room temperature and pressure, calcite is the most stable of the three polymorphs of calcium carbonate ($CaCO_3$).[23, 24] Calcite has a density of 2.71 g/cm^3 and a Mohs hardness of 3. Aragonite and vaterite, the two other polymorphs of calcium

[a] Calcite crystals containing amino acid additives were synthesized by Yi-Yeoun Kim in a collaboration with the Meldrum group at the University of Leeds.

carbonate have densities of 2.95 and 2.56 g/cm^3 respectively.[25] Calcite does not convert to aragonite under hydrostatic pressure[26], though calcite does convert to aragonite upon ball milling[27, 28] and aragonite converts to calcite on heating to 400 °C.[28] Geologic calcite in the form of optically clear, Iceland spar decomposes between 700 and 900 °C.[29, 30]

The calcite crystal structure was originally solved by W.L. Bragg using x-ray diffraction.[31, 32] It can be thought of as the rock salt lattice structure found in NaCl, turned on its diagonal and flattened down this diagonal by 77% (Figure 1.1). The sodium cations are then replaced by calcium cations and the chlorine anions by carbonate groups. The three fold symmetry axis of the carbonate groups coincides with the flattening direction. However, alternating layers of carbonate groups are rotated by 180 degrees, requiring two $CaCO_3$ groups per primitive unit cell.

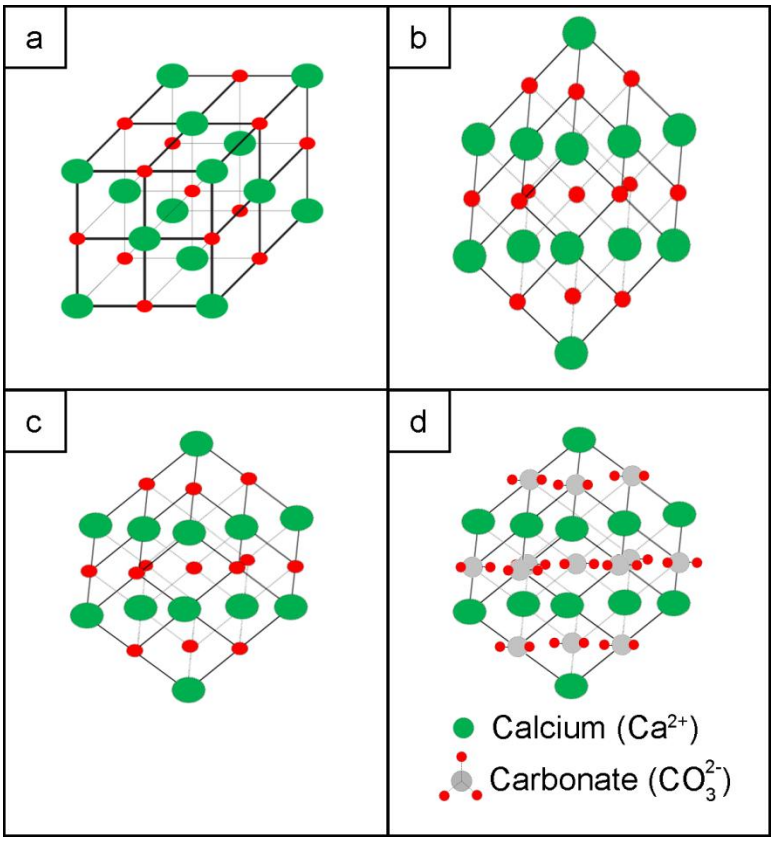

Figure 1.1 Schematic of calcite crystal structure as derived from rocksalt lattice. (a) Initial rocksalt cubic lattice. (b) Lattice rotated onto the <111> diagonal. (c) Lattice compressed down diagonal to 77% of original length. (d) Calcium substituted for green lattice points and carbonate substituted for red lattice points. Planes of carbonate groups alternate directions each layer. Some atoms are removed for clarity.

The calcite space group is $R\bar{3}c$ (International Union of Crystallography No. 167). Here, R represents the rhombohedral lattice system (Figure 1.2c) within the trigonal crystal system. The $\bar{3}$ stands for the three fold rotational symmetry of lattice when viewed perpendicular to the carbonate planes, and the overline represents the inversion symmetry seen through the center calcium of the rhombohedral cell (Figure 1.2c). Finally, the c represents a glide plane, or a reflection followed by translation. This is possible along the

c-axis with translation of half a unit cell (Figure 1.2c) and the carbonate group can be used to follow this operation by first reflecting horizontally then moving vertically.

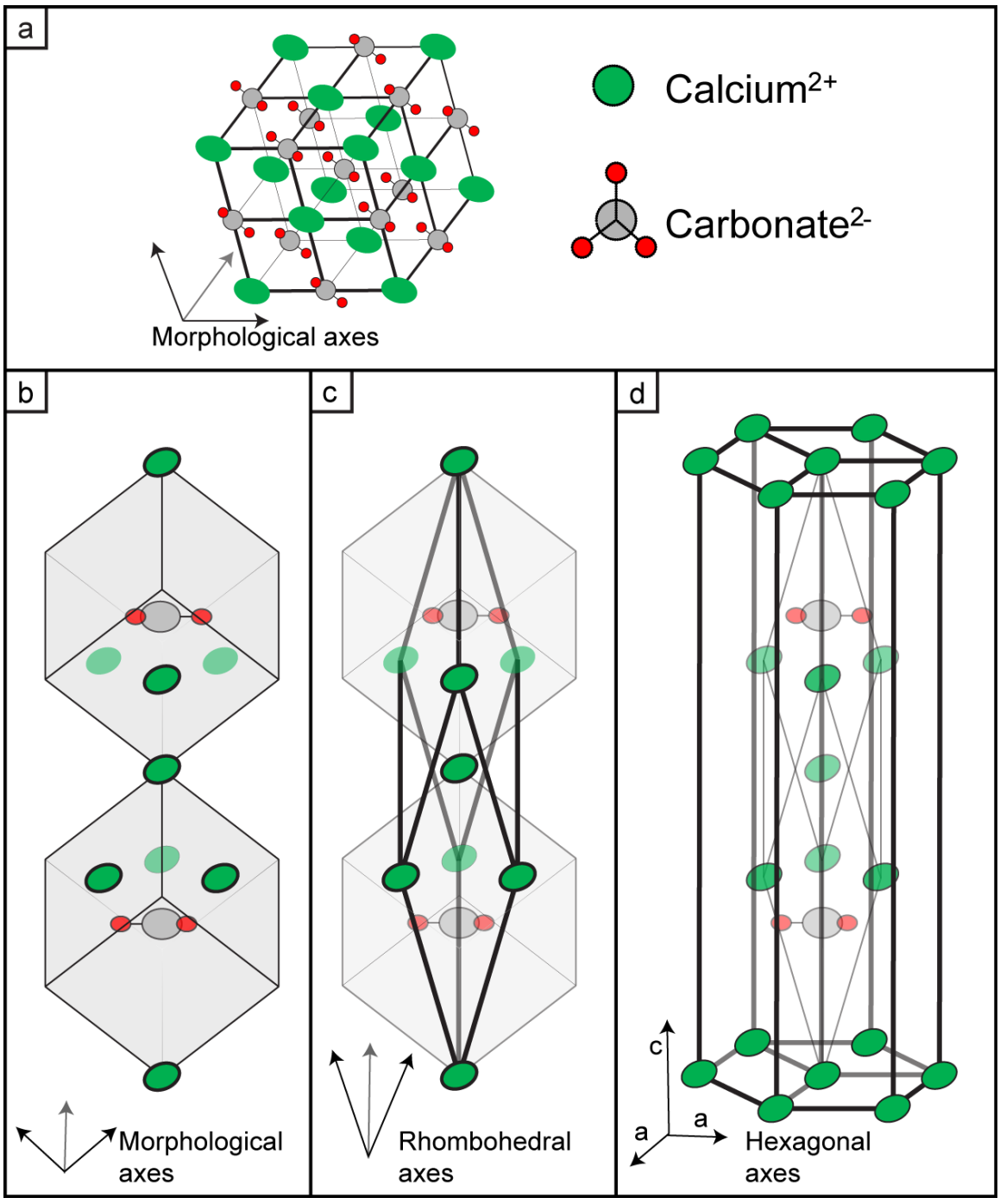

Figure 1.2 Schematic of relationship between calcite morphological, rhombohedral and hexagonal unit cells. For clarity, not all atoms are shown in b-d.

Historically, there have been several choices of the unit cell used to generate the calcite crystal structure (Figure 1.2). The earliest choice, called the morphological unit cell, was chosen because of the rhombohedral morphology found in geologic Iceland spar (Figure 1.2a). Although the morphological cell has 4 $CaCO_3$ groups, it does not contain the symmetry of the carbonate groups alternating along the c-axis and is therefore not a true unit cell. This can be seen in Figure 1.2b where the two adjacent morphological cells have inverted carbonate groups, demonstrating that space cannot be filled by simple translation. Accommodating the full symmetry of the space group, while maintaining a similar shape of the morphological unit cell, would require 8 $CaCO_3$ groups or 40 atoms. A simpler way to capture the symmetry of the $R\bar{3}c$ space group is by using a rhombohedral unit cell (Figure 1.2c) which contains 2 $CaCO_3$ groups and whose height is twice that of the morphological diagonal. However, neither the axes of the rhombohedral, nor of the morphological unit cells, are orthogonal to one another. Therefore, the hexagonal unit cell representation (a=4.99, c= 17.06 Å)[29] has become standard notation in the literature[33] because the presence of at least one orthogonal axis makes structure refinement easier. In addition to the numerical notation, a shorthand notation based on letters, was developed to associate commonly observed slip systems families.

A schematic of the crystal structure showing commonly referenced atomic planes is shown below (Figure 1.3). In order to view all the commonly referenced planes in a common zone axis (that of the *a*-axis), the figure is rotated azimuthally around the *c*-axis by 30 degrees when compared with Figure 1.2. The $CaCO_3$ groups are now pointing in and out of the plane of the paper, rather than left to right. Figure 1.3b shows the possible relative motion of atoms when calcite is compressed under hydrostatic pressure along the

c-axis. The atoms in the calcite crystal can either slip (translate) on the {104} or {012} planes or twin (rotate carbonate groups to form a mirror plane) along the {018} planes. An important and unusual feature of these slip systems is that they can shear only in the directions shown due to constraints imposed by the carbonate groups.

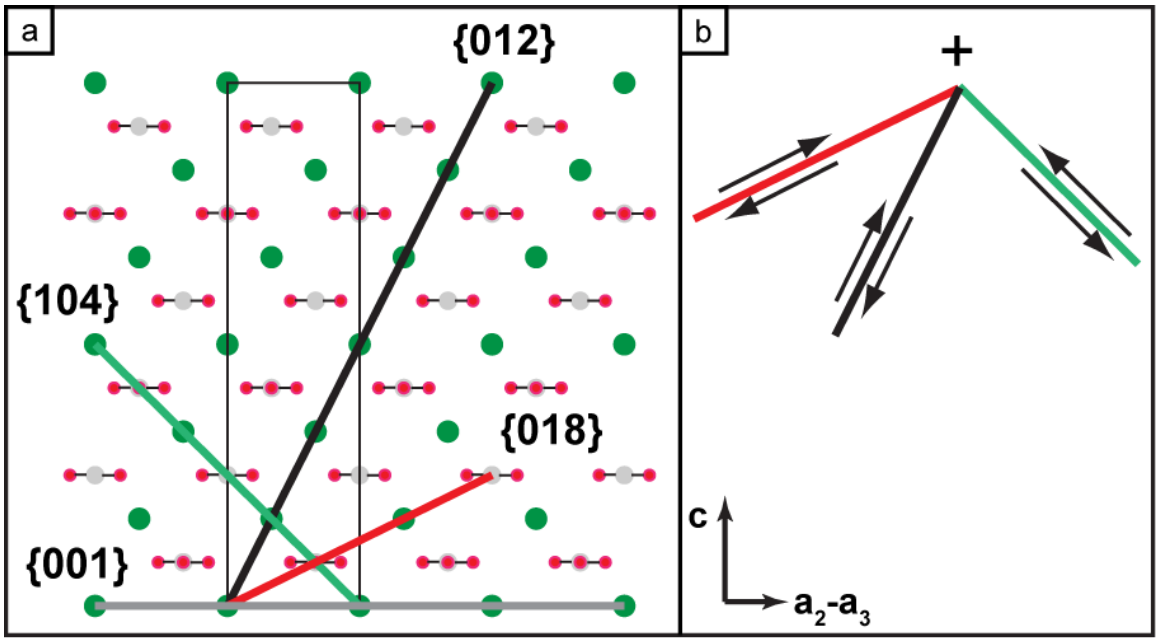

Figure 1.3 (a) Schematic of calcite structure showing commonly referenced planes in hexagonal notation. Looking down the a_1-axis which is normal to the plane of this paper, all labeled planes share this common a_1 zone axis. (b) Relative motion of twin and slip systems. The direction, "(+) sense", is denoted by relative motion of the upper portion of the crystal over the lower in the direction of the +c-axis.

Table 1 relates some commonly expressed faces in the 3 crystal systems, along with shorthand or letter notation, found in literature. Unfortunately, Turner and Griggs,[34] two pioneering investigators of calcite deformation, chose to use a morphological hexagonal unit cell which has a 1/4 spaced c-axis.[35]

Table 1 Relationships between notations found in the literature depending on the choice of unit cell.

Morphological (pseudo cubic)	***Rhombohedral***	***Hexagonal***	***Morphological Hexagonal (Turner, Griggs)***	***Shorthand Notation***
(100)	(211)	(104)	(101)	r
(1-1-1)		(012)	(021)	f
(110)		(018)	(012)	e
(111)	(111)	(001)	(001)	c
(1-10)		(110)		a
(22-1)		(100)	(100)	m

The crystal structure of calcite leads to anisotropic physical properties. The large optical birefringence (n_o ~1.66, n_e ~ 1.49 at 590nm) of calcite has been studied for several centuries[36] and has been utilized to make everything from polarizers[37] to cloaking devices.[38] The optical axis must coincide with the 3-fold symmetry axis which enables determination of the *c*-axis. Figure 1.4 demonstrates the optical birefringence of calcite when viewed normal to the {104} face. The (+) direction or "sense" is defined as movement toward the upper left corner of the crystal (Figure 1.4a), bounded by three obtuse angles, while the (-) negative direction is defined by movement toward the opposite corner of the face diagonal (Figure 1.3b).

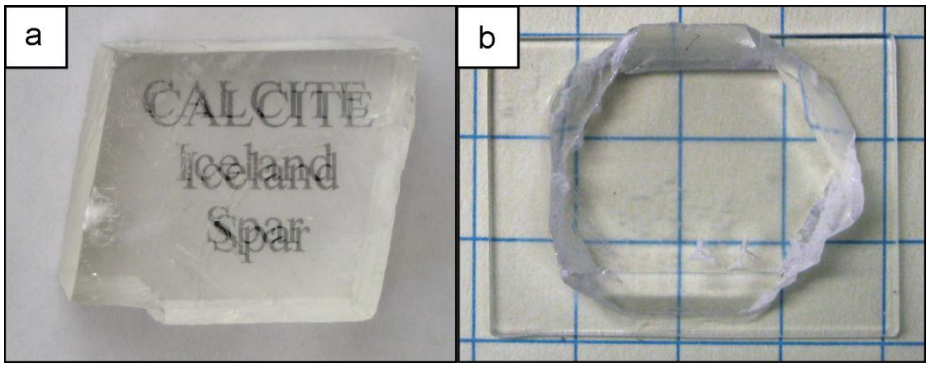

Figure 1.4 Geologic calcite in the form of Iceland spar. (a) Rhombohedral morphology expressing {104} facets. (b) Crystal polished on top and bottom to expose the {001} plane. The c-axis is the optical axis of calcite.

The mechanical response of calcite is also highly anisotropic. Upon heating, the *a*-axis contracts at -3.7 * 10^{-6} / °C while the *c*-axis expands by 25.6 * 10^{-6} / °C.[29] Calcite is also auxetic, meaning that it has a negative Poisson's ratio when uniaxial stress is applied in certain directions.[39] The calculated angle of applied uniaxial stress for auxetic behavior is ~45 degrees from the *c*-axis, so I believe it to be on a {104} plane though I was unable to translate the compliance contour plot used in Professor Wheeler's paper to rhombohedral coordinates.[39] The auxeticity may be due to the carbonate groups rigidly retaining their shape and rotating out of the (001) plane during compression, causing the *c*-axis to expand while the *a*-axis contracts. Interestingly, increased indentation hardness has been noted in auxetic materials due to densification under compression[40] and this mechanism could contribute to the anisotropic mechanical response of calcite.

Calcite has several well-characterized plastic deformation modes (Figure 1.3) including twinning on the {018} planes and slip on the {104}, {012} and {001} planes. {018} twinning[35, 41-46] (Figure 1.5) in the positive sense is the only available plastic deformation mode when stress is applied at room temperature with no confining

hydrostatic pressure.[34, 43, 45] However, at elevated temperature or under increased hydrostatic pressure, slip on the {012}, {104},[47, 48] and {001} planes is possible.[35, 49] At room temperature, the critical resolved shear stress for {018} twinning was measured at <10 MPa while {104} and {012} slip was measured between 100 and 200 MPa.[34, 48] Mechanically induced twinning, as opposed to growth twinning, was first seen by Brewster by the reflection of candlelight off the raised edges of the twin lamellae, though he believed these raised edges to be a secondary cleavage.[50] Christiaan Huygens, known for his wave theory of light and study of birefringence in calcite, also noted that a knife will glide on the {104} face much more easily in the negative sense than in the positive sense. In the positive sense, the knife is caught by the crystal and taken below the surface "like [sliding against] the scales of a fish".[51 b] Undoubtably, this is due to twinning on the {018} planes caused by catching rough portions of the knife edge. As the existence of atomic structure was unknown in 1690, it is unlikely that Huygens knew that fish scales may also contain calcium carbonates,[52] but it does emphasize the importance of controlling for crystallographic orientation when measuring the mechanical properties of minerals!

[b] Brewster included a translation of a section of Christiaan Huygens' Traite de la Lumiere, 1690.

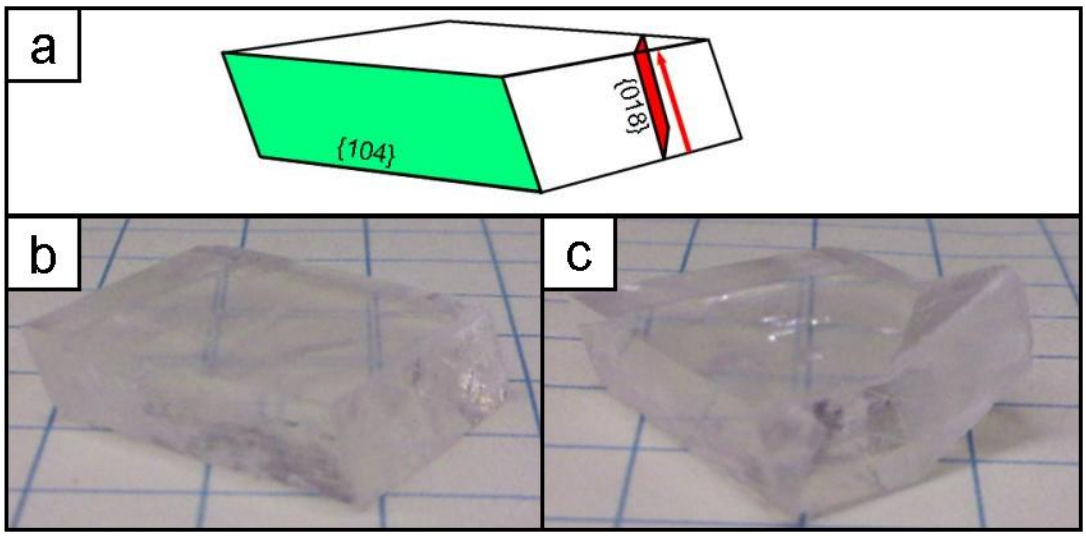

Figure 1.5 Iceland spar (b) before and (c) after twinning along the {018} plane. The calcite rhombohedron was pressed against a hard lab bench at room temperature and pressure to deform the crystal. The spacing between grid marks is ¼ inch.

Like the {104} face, the (001) face also exhibits scratch anisotropy. The polish is smooth when the motion of the polishing film is towards the apex of the (001) face, but rough when going in the opposite direction. Crystallographic orientation must therefore be controlled when polishing samples for nanoindentation or TEM. Interestingly, the direction of polish is less sensitive when polishing synthetic calcite with high percentages of additives, or when polishing biogenic samples.

Mechanically induced {018} twins in calcite may exhibit either permanent or recoverable behavior, depending on whether the elastic stored energy associated with the twin has reached a metastable energy state. Permanent or residual twins (Figure 1.5), seen as lamellae by Brewster, are created when a {018} twin propagates through a crystal to reach a free surface, releasing the stored elastic energy associated with the dislocation. However, recoverable twins, which were called “elastic twins” by Garber in 1937,[46] form

when an applied stress causes a twin to propagate into a crystal, and disappear upon removal of the applied stress. When the applied stress is removed, the crystal lowers its energy by reversing the course of the twins (Figure 1.6). A recoverable twin will become a permanent twin if it is capable of making it close enough to a free surface (typically the face on the other side of the crystal), that it is able to release the elastic stored energy by propagating completely to the free surface.

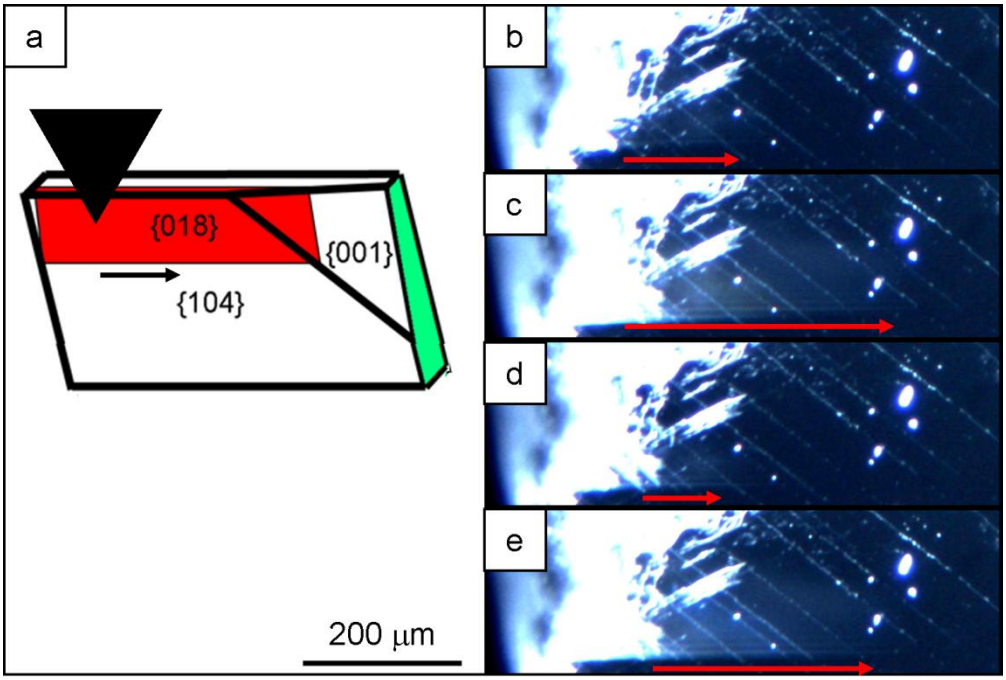

Figure 1.6 Optical micrographs of recoverable twins (brighter planes schematically highlighted by red arrows) as seen in cross polarized light. (a) A knife edge is pressed into the edge of the crystal inducing recoverable twinning on the {018} plane. (b-e) indicate the recoverable nature of the twin upon two cycles of loading and unloading.

The macroscopic stress needed to initiate a recoverable twin is roughly an order of magnitude greater than that needed to propagate the twin.[41, 46] Additionally there is a hysteresis in the load and unload curve once a recoverable twin has been formed.[44] Once a recoverable twin has been formed, it requires a finite release of the stress before the

twin begins to retreat, and it takes additional stress to restart the elongation.

The fracture morphology of calcite is dependent on the stress state that is being applied during the test, as well as the species that is being tested. Although conchoidal- or glassy fracture (as opposed to cleavage along {104} planes) has been strongly associated in literature as a hallmark of biogenic calcite,[53-55] Towe, whose paper is often cited to demonstrate this difference,[56] noted that conchoidal fracture can also be seen in geologic calcite.[56, 57] Furthermore, in one paper, the mollusk *Atrina serrata*, displayed cleavage-like fracture, although the other six species tested (from four phyla), all displayed conchoidal fracture.[58] Therefore, caution should be applied when comparing the fracture morphology of geologic and biogenic calcite specimens. Some of the fracture differences noted in literature between geologic and biogenic calcite and even within biogenic calcite specimens, may be due to differences in the stress state applied during the fracture experiment.[55, 56] For instance, the fracture morphology of geologic calcite cleaved using a razor blade may be compared with sea urchin spines fractured under compressive-, tensile-, or bending stress states. Additionally, inhomogeneities such as pores or voids found in sea urchin spines may cause local stress state variations at the crack front that are not found in Iceland spar or other species.

1.3 Nanoindentation

Depth sensing nanoindentation is an experimental method that involves pressing an indenter with a calibrated shape into a sample and measuring the force as a function of displacement.[59, 60] Nanoindentation is useful for measuring the hardness and modulus of biogenic and synthetic samples because data can be obtained from very small sample volumes. Accurate information can be obtained from indentations with depths less than

50 nm and corresponding widths less than ~200nm. The biogenic and synthetic samples used in this thesis typically ranged from 30 to 70 μm in diameter enabling either multiple measurements per sample or measurements as a function of spatial concentration gradients.

All hardness measurements in this thesis used a Berkovich, three sided pyramidal indenter whose geometry is shown in Figure 1.7. In contrast to four sided Knoop and Vickers indenters typically used in a classical hardness tests, the three sided pyramidal indenter can be more easily sharpened to a point, enabling smaller test depths to be accurately measured. However, in keeping with the classical tests, the Berkovich indenter has the same depth to area ratio as the Vickers indenter.

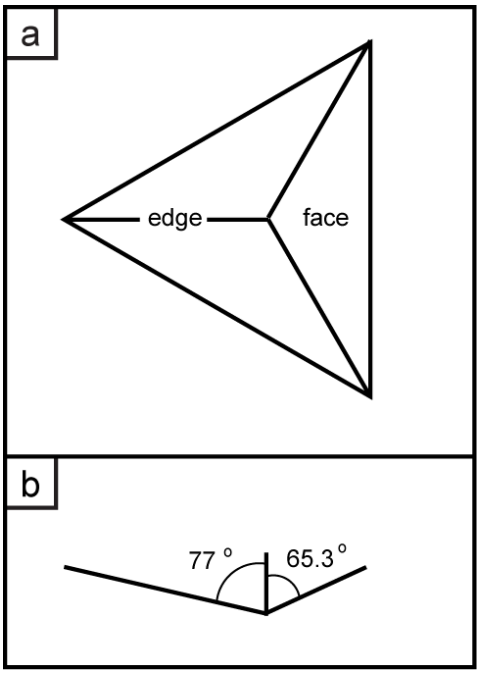

Figure 1.7 Schematic diagrams of a Berkovich indenter tip. (a) Top view of indenter. (b) Side view including indenter angles.

We used nanoindentation in quasistatic mode to determine the hardness and modulus of calcite. All experiments used a “trapezoidal” load function with 5 second

load, hold and unload segments, with the unload segment being used to calculate hardness and modulus.[59, 60] The velocity of recoverable twins in calcite has been found by high speed photography to be ~2 m/s and independent of the magnitude of shear stress.[42] Since the depth and diameter of the indents used in this thesis are on the order of 1 μm, and the unload segment spanned 5 seconds, any recoverable twins would have reached a metastable equilibrium during unloading. Therefore, the load-displacement curves fully reflect any displacement of the sample due to recoverable twinning.

The hardness of the sample may be calculated by dividing the maximum load by the projected area at the contact depth (Equation 1).

$$H = \frac{P_{max}}{A_c} \qquad (1)$$

The modulus calculated from an indentation test differs from the Young's modulus measured in a uniaxial tension test because the bulk material adjacent to an indent restrains plastic deformation, while this back pressure does not exist in a uniaxial tension test. We use the standard Oliver and Pharr method to determine the modulus of the sample according to Equation 2.[59, 60]

$$E_r = \frac{1}{\beta}\frac{\sqrt{\pi}}{2}\frac{S}{\sqrt{A_c}} \qquad (2)$$

Here, E_r is the reduced modulus, S is the stiffness of the unloading curve, β is a geometrical constant and A_c is the projected contact area. The reduced modulus includes both an elastic response from the diamond indenter tip as well as from the sample. It is possible to separate out the components using Equation 3.

$$\frac{1}{E_r} = \frac{1-\nu_i^2}{E_i} + \frac{1-\nu_s^2}{E_s} \qquad (3)$$

Here, the subscripts *i* and *s* refer to indenter and sample, while ν represents

Poisson's ratio. In this thesis, we report the plane strain indentation modulus, $E_s/(1-\nu_s^2)$, also known as the indentation modulus, E_{it} as this is the basic materials property obtained in a nanoindentation experiment. In some studies, the reduced modulus, E_r is reported, although this includes the elastic properties of both the tip and sample as shown in Equation 3. It is not sensible to try to separate values for Young's modulus and Poisson's ratio since these values cannot be determined separately, and the standard Oliver and Pharr analysis assumes an isotropic material, which calcite is not.

1.4 Synthetic Calcite Containing Additives

Biogenic calcites contain a wide variety of additives ranging in size from substitutional magnesium ions to second phase polymer networks. However, deciphering the hardness and modulus effects of each individual additive found in biogenic calcite is difficult, because variations in composition, morphology, and orientation all may occur within a single biogenic specimen. A synthetic route is capable of controlling for composition, morphology and orientation, enabling us to determine the hardness and modulus effects of the individual additives found in biogenic calcite.

There is a large background of literature on growth conditions that create single crystal calcite, as well as methods for incorporation of additives into these single crystals.[61] Supersaturation has been effected by changes in temperature or pH, mixing of precursor salts, evaporation of the solvent, liquid diffusion of Ca^{2+} and CO_3^{2-}, and by gas diffusion of CO_2. Calcite has also been made to incorporate chemically, physically and morphologically diverse impurities which range from atomic substitutions to structure directing frameworks.

In research presented in this thesis, calcite was grown by gas diffusion of CO_2

(Figure 1.8) into either a solution or a gel containing calcium chloride and the desired additive (magnesium, amino acid, or agarose). As the calcite grows, it incorporates the additive, resulting in hybrid crystals whose mechanical properties can be quantified. The growth chamber is a large glass enclosure, approximately 4 liters in size, which houses the experimental growth conditions. A 20 milliliter vial containing approximately 0.5 grams of ammonium carbonate $(NH_4)_2CO_3$ is placed in the enclosure along with a 5 mM $CaCl_2$ solution containing the additive.[c] As the ammonium carbonate decomposes, it creates CO_2 gas which diffuses into the $CaCl_2$ solution, resulting in a supersaturated medium and eventual growth of calcite.

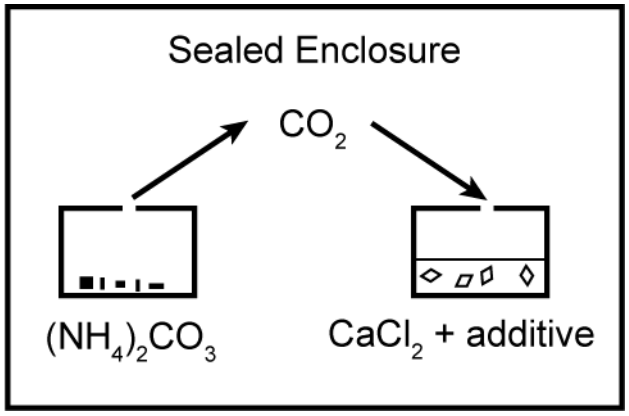

Figure 1.8 Schematic diagram showing the growth configuration used in this thesis. Solid ammonium carbonate decomposes into ammonia and carbon dioxide. The carbon dioxide then diffuses into a calcium- and additive rich solution or gel. Finally, rhombohedral single crystals of calcite incorporating the additives precipitate out of solution.

Schematic diagram showing growth configuration used in this thesis. Solid ammonium carbonate decomposes into ammonia and carbon dioxide. The carbon dioxide then

[c] Growth conditions are similar for the calcite containing amino acid additives, grown by Yi-Yeoun Kim, and are specified in chapter 3.

diffuses into a calcium- and additive rich solution or gel, precipitating an additive containing calcite.

1.5 Strengthening Mechanism

We propose that strengthening mechanisms found in metallurgy and based on reduced plasticity by hindered dislocation motion can be used to explain the increased hardness of biogenic calcite. Plasticity is permanent deformation caused by the rearrangement of atomic bonds. In the case of a perfectly ordered crystal, this rearrangement of bonds occurs at localized defect sites called dislocations. As stress is applied, dislocations can move through the crystalline lattice much like an inchworm walks across a table, or a Vernier caliper reading moves as the calipers are shifted; bonds break and reform, creating a zone of lattice defects that propagates through the rest of the perfect crystal. This localized defect motion requires less force than shearing and reforming all the bonds at the same time.[62]

During an indentation test that leaves behind a permanent shape change, material plastically deforms to accommodate the volume of the indenter tip and lower the energy of the system. Since hardness is a measure of the material's resistance to plastic deformation, anything that impedes dislocation motion will increase the hardness of the material. Analogous to strengthening in metallic crystals,[62] we propose that additives and microstructural variations act as impediments to dislocation motion and are the source of the higher hardness of biogenic calcite.

In calcite, these dislocations, or crystallographic defects, move on the {012}, {104} and {018} slip- and twin planes.[34, 35, 48, 49] The black line in Figure 1.9 schematically represents an edge dislocation, where an extra plane of atoms has been

sandwiched above the slip plane. As stress is applied to the system, i.e. by an indenter tip, this dislocation can move on {012}, {104} and {018} slip- and twin planes to accommodate the increased stress.

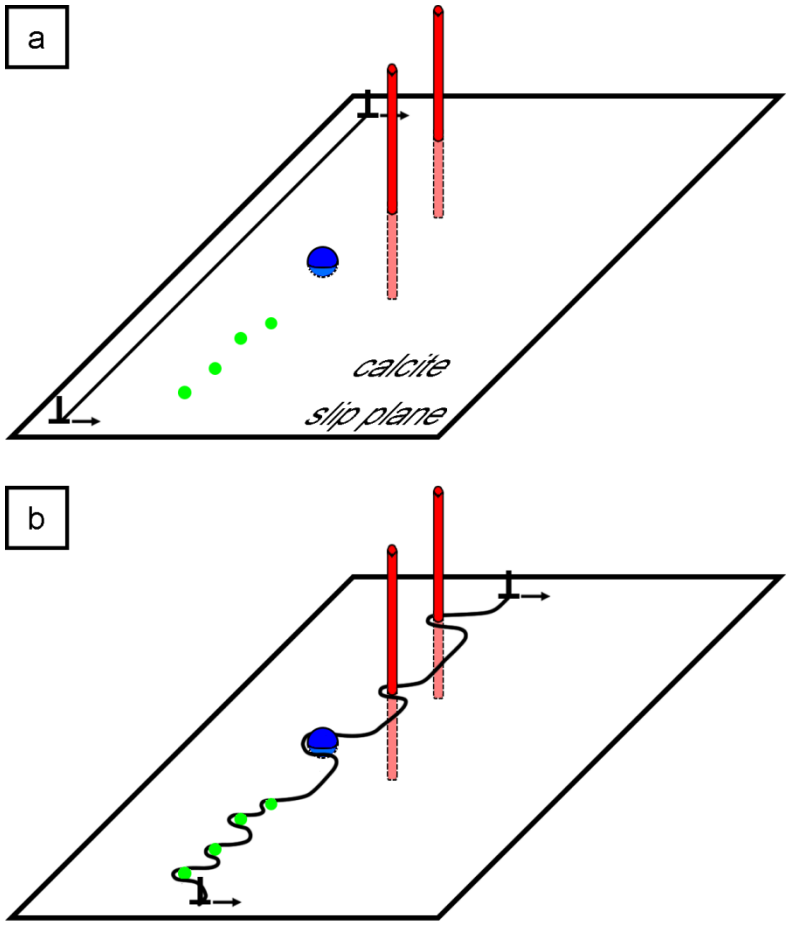

Figure 1.9 (a) Schematic of dislocation encountering substitutional additives (green), a small molecule second phase aggregate (blue), and two fibers (red). The line connecting inverted "T"s, represents an extra plane of atoms, extending upward from the slip plane. (b) As the dislocation moves to the right, the stress fields of the additives impede the motion, resulting in a back stress and higher hardness.

Different strengthening mechanisms would be expected for the three types of additives shown in Figure 1.9. For an atomic- or molecular substitutional additive, the

stress fields caused by the size- or elastic modulus- mismatch of the inclusions with the crystalline matrix would impede the motion of the dislocation by acting as a barrier to continued dislocation motion. For a second-phase-aggregate- or fiber- additive, the local inhomogeneous strain field due to an elastic modulus mismatch could also hinder dislocation motion. Finally, a *rigid* second phase aggregate or fiber could also physically block dislocation motion and prevent rearrangement of bonds if it were incapable of shearing.

With increased stress, the dislocations may continue to move. For substitutional additives, if a great enough stress were applied, the dislocation would be able to unpin itself from the obstacles and continue moving through the lattice to reduce the energy of the system (Figure 1.10). For a soft second phase aggregate or fiber, continued dislocation motion would leave behind a sheared second phase, where the top portion of the obstacle has been pushed aside by one lattice space (Figure 1.10a).

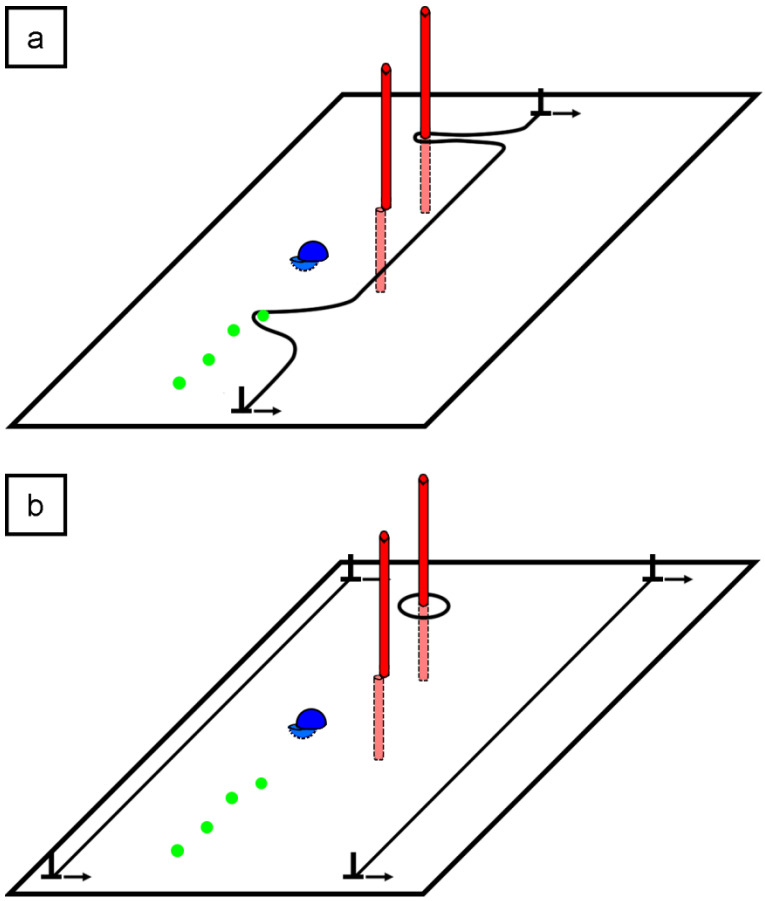

Figure 1.10 Schematic of dislocation motion under applied stress. (a) If the stress is great enough, the dislocation will unpin itself from the substitutional additives (green), or shear the second phase and weak fiber additives (blue and lower red). A strong fiber (top red) will resist shearing, forcing the dislocation to lengthen. (b) Dislocation merges with itself leaving behind a high energy defect. This residual defect can now impede the motion of a second dislocation.

However, if the second phase aggregate is stronger than the dislocation, the dislocation must leave behind a residual defect, so that the rest of the dislocation may continue to move. This residual defect (Figure 1.10b), may then act with other incoming dislocations to further impede dislocation motion, resulting in an increase in back

pressure and a higher hardness.

1.6 Conclusion

According to Stephen Mann, the guiding principles of biomineralization are "the study of the formation, structure and properties of inorganic solids deposited by biological systems." Materials science and engineering, as defined by the National Academy of Sciences' 1974 COSMAT report, is the "application of knowledge relating the composition, structure, and processing of materials to their properties and uses."[63] The similarity of these two definitions suggests a natural overlap between the fields of biomineralization and materials science and engineering. It is therefore a progression of both fields to apply theories established in traditional materials science and engineering literature to biominerals. This thesis uses careful control of crystallographic orientation as well synthetic control of compositional variation in order to quantify the reasons for the increased hardness found in biogenic minerals. Additionally, by examining the effects of individual compositional impurities found in biogenic calcite, we hope to better understand how biomineralization is able to strengthen these materials, and in turn, be able to create synthetic minerals with tailored mechanical properties.

1. Mann S. Molecular tectonics in biomineralization and biomimetic materials chemistry. *Nature* 1993, **365**(6446)**:** 499-505.

2. Meyers MA, Chen P-Y, Lin AY-M, Seki Y. Biological materials: structure and mechanical properties. *Prog Mater Sci* 2008, **53**(1)**:** 1-206.

3. Weiner S, Dove PM. An Overview of Biomineralization Processes and the Problem of the Vital Effect. *Reviews in mineralogy and geochemistry* 2003, **54**(1)**:** 1-29.

4. Jackson AP, Vincent JFV, Turner RM. The mechanical design of nacre. *Proc R Soc Lond Ser B-Biol Sci* 1988, **234**(1277)**:** 415-440.

5. Barthelat F, Espinosa HD. An experimental investigation of deformation and fracture of nacre-mother of pearl. *Exp Mech* 2007, **47**(3)**:** 311-324.

6. Currey JD. Mechanical properties of mother of pearl in tension. *Proc R Soc Lond Ser B-Biol Sci* 1977, **196**(1125)**:** 443.

7. Kamat S, Kessler H, Ballarini R, Nassirou M, Heuer AH. Fracture mechanisms of the *Strombus gigas* conch shell: II-micromechanics analyses of multiple cracking and large-scale crack bridging. *Acta Mater* 2004, **52**(8)**:** 2395-2406.

8. Kamat S, Su X, Ballarini R, Heuer AH. Structural basis for the fracture toughness of the shell of the conch *Strombus gigas*. *Nature* 2000, **405**(6790)**:** 1036-1040.

9. Rubner M. Materials science: Synthetic sea shell. *Nature* 2003, **423**(6943)**:** 925-926.

10. Li XD, Chang WC, Chao YJ, Wang RZ, Chang M. Nanoscale structural and mechanical characterization of a natural nanocomposite material: the shell of red abalone. *Nano Letters* 2004, **4**(4)**:** 613-617.

11. Merkel C, Deuschle J, Griesshaber E, Enders S, Steinhauser E, Hochleitner R*, et al.* Mechanical properties of modern calcite (*Mergerlia truncata*) and phosphate-shelled brachiopods (*Discradisca stella* and *Lingula anatina*) determined by nanoindentation. *J Struct Biol* 2009, **168**(3)**:** 396-408.

12. Pérez-Huerta A, Cusack M, Zhu W, England J, Hughes J. Material properties of brachiopod shell ultrastructure by nanoindentation. *J R Soc Interface* 2007, **4**(12)**:** 33-39.

13. Pérez-Huerta A, Cusack M, Zhu W. Assessment of crystallographic influence on material properties of calcite brachiopods. *Mineral Mag* 2008, **72**(2)**:** 563-568.

14. Moureaux C, Pérez-Huerta A, Compère P, Zhu W, Leloup T, Cusack M*, et al.* Structure, composition and mechanical relations to function in sea urchin spine. *J Struct Biol* 2010, **170**(1)**:** 41-49.

15. Su X, Kamat S, Heuer AH. The structure of sea urchin spines, large biogenic single crystals of calcite. *J Mater Sci* 2000, **35**(22)**:** 5545-5551.

16. Kayano K, Saruwatari K, Kogure T, Shiraiwa Y. Effect of Coccolith Polysaccharides Isolated from the Coccolithophorid, Emiliania huxleyi, on Calcite Crystal Formation in In Vitro $CaCO_3$ Crystallization. *Mar Biotechnol* 2011, **13**(1)**:** 83-92.

17. Westbroek P, Jong EWd, Wal Pvd, Borman AH, Vrind JPMd, Kok D*, et al.*

Mechanism of Calcification in the Marine Alga Emiliania huxleyi [and Discussion]. *Philosophical Transactions of the Royal Society of London Series B, Biological Sciences* 1984, **304**(1121)**:** 435-444.

18. Nudelman F, Shimoni E, Klein E, Rousseau M, Bourrat X, Lopez E*, et al.* Forming nacreous layer of the shells of the bivalves Atrina rigida and Pinctada margaritifera: An environmental- and cryo-scanning electron microscopy study. *J Struct Biol* 2008, **162**(2)**:** 290-300.

19. Nudelman F, Chen HH, Goldberg HA, Weiner S, Addadi L. Spiers memorial lecture: lessons from biomineralization: comparing the growth strategies of mollusc shell prismatic and nacreous layers in *Atrina rigida*. *Faraday Discuss* 2007, **136:** 9-25.

20. Silyn-Roberts H, Sharp RM. The Similarity of Preferred Orientation Development in Eggshell Calcite of the Dinosaurs and Birds. *Proceedings of the Royal Society of London Series B, Biological Sciences* 1989, **235**(1281)**:** 347-363.

21. Lins U, Farina M, Kurc M, amp, x, cio*, et al.* The Otoconia of the Guinea Pig Utricle: Internal Structure, Surface Exposure, and Interactions with the Filament Matrix. *J Struct Biol* 2000, **131**(1)**:** 67-78.

22. Ross MD, Pote KG. Some Properties of Otoconia. *Philosophical Transactions of the Royal Society of London Series B, Biological Sciences* 1984, **304**(1121)**:** 445-452.

23. Kitano Y, Hood DW, Park K. Pure Aragonite Synthesis. *J Geophys Res* 1962, **67**(12)**:** 4873.

24. Grasby SE. Naturally precipitating vaterite (μ-$CaCO_3$) spheres: unusual carbonates formed in an extreme environment. *Geochim Cosmochim Ac* 2003, **67**(9)**:** 1659-1666.

25. Macdonald G, J., F. Experimental determination of calcite-aragonite equilibrium relations at elevated temperatures and pressures. *Am Mineral* 1956, **41**(9).

26. Merrill L, Bassett WA. Miniature diamond anvil pressure cell for single crystal x-ray diffraction studies. *Rev Sci Instrum* 1974, **45**(2)**:** 290-294.

27. Gammage RB, Glasson DR. The effect of grinding on the polymorphs of calcium carbonate. *J Colloid Interface Sci* 1976, **55**(2)**:** 396-401.

28. Burns JH, Bredig M. Transformation of calcite to aragonite by grinding. *The Journal of Chemical Physics* 1956, **25**(6)**:** 1281-1281.

29. Markgraf SA, Reeder RJ. High-temperature structure refinements of calcite and

magnesite. *Am Mineral* 1985, **70**(5-6)**:** 590-600.

30. Rodriguez-Navarro C, Ruiz-Agudo E, Luque A, Rodriguez-Navarro AB, Ortega-Huertas M. Thermal decomposition of calcite: Mechanisms of formation and textural evolution of CaO nanocrystals. *Am Mineral* 2009, **94**(4)**:** 578-593.

31. Bragg WL. The structure of some crystals as indicated by their diffraction of x-rays. *P R Soc Lond a-Conta* 1913, **89**(610)**:** 248-277.

32. Bragg WH, Bragg WL. The reflection of X-rays by crystals. *P R Soc Lond a-Conta* 1913, **88**(605)**:** 428-438.

33. Skinner AJ, LaFemina JP, Jansen HJF. Structure and bonding of calcite; a theoretical study. *Am Mineral* 1994, **79**(3-4)**:** 205-214.

34. Turner FJ, Griggs DT, Heard H. Experimental deformation of calcite crystals. *Geol Soc Am Bull* 1954, **65**(9)**:** 883-933.

35. Barber DJ, Wenk HR. Deformation twinning in calcite, dolomite, and other rhombohedral carbonates. *Phys Chem Miner* 1979, **5**(2)**:** 141-165.

36. Bartholin E. *Erasmi Bartholini Experimenta crystalli Islandici disdiaclastici, qvibus mira & insolita refractio detegitur*. apud J. Blaeu, 1670.

37. Bridges T, Kluver J. Dichroic calcite polarizers for the infrared. *Appl Opt* 1965, **4**(9)**:** 1121-1125.

38. Chen X, Luo Y, Zhang J, Jiang K, Pendry JB, Zhang S. Macroscopic invisibility cloaking of visible light. *Nat Commun* 2011, **2:** 176.

39. Aouni N, Wheeler L. Auxeticity of calcite and aragonite polymorphs of $CaCO_3$ and crystals of similar structure. *Phys Status Solidi B* 2008, **245**(11)**:** 2454-2462.

40. Alderson KL, Fitzgerald A, Evans KE. The strain dependent indentation resilience of auxetic microporous polyethylene. *J Mater Sci* 2000, **35**(16)**:** 4039-4047.

41. Cahn R. Soviet work on mechanical twinning. *Il Nuovo Cimento (1943-1954)* 1953, **10:** 350-386.

42. Cooper RE. Kinetics of Elastic Twinning in Calcite. *Proceedings of the Royal Society of London Series a-Mathematical and Physical Sciences* 1962, **270**(1343)**:** 525.

43. Clayton J, Knap J. Phase field modeling of twinning in indentation of transparent crystals. *Model Simul Mater Sc* 2011, **19**(8)**:** 085005.

44. Kosevich AM, Boiko VS. Dislocation theory of elastic twinning in crystals. *Soviet Physics Uspekhi-Ussr* 1971, **14**(3)**:** 286.

45. Kaga H, Gilman JJ. Twinning and detwinning in calcite. *J Appl Phys* 1969, **40**(8)**:** 3196.

46. Boĭko VS. *Reversible crystal plasticity*. American Institute of Physics: New York :, 1994.

47. Debresser JHP, Spiers CJ. Slip systems in calcite single crystals deformed at 300-800 degrees C. *Journal of Geophysical Research-Solid Earth* 1993, **98**(B4)**:** 6397-6409.

48. DeBresser JHP, Spiers CJ. Strength characteristics of the r, f, and c slip systems in calcite. *Tectonophysics* 1997, **272**(1)**:** 1-23.

49. Barber DJ, Wenk HR, Gomez-Barreiro J, Rybacki E, Dresen G. Basal slip and texture development in calcite: new results from torsion experiments. *Phys Chem Miner* 2007, **34**(2)**:** 73-84.

50. Brewster D. On a new cleavage in calcareous spar, with a notice of a method of detecting secondary cleavages in minerals. *Edinburgh Journal of Science* 1828, **9:** 311-314.

51. Huygens C. On the cause of the extraordinary figure of calcareous spar, and on its cleavage in three different directions. *Edinburgh Journal of Science* 1828, **9:** 314-317.

52. Onozato H, Watabe N. Studies on fish scale formation and resorption. III. Fine structure and calcification of the fibrillary plates of the scales in Carassius auratus (Cypriniformes: Cyprinidae). *Cell Tissue Res* 1979, **201**(3)**:** 409-422.

53. Berman A, Addadi L, Weiner S. Interactions of sea urchin skeleton macromolecules with growing calcite crystals- a study of intracrystalline proteins. *Nature* 1988, **331**(6156)**:** 546-548.

54. Seto J, Ma Y, Davis SA, Meldrum F, Gourrier A, Kim Y-Y*, et al.* Structure-property relationships of a biological mesocrystal in the adult sea urchin spine. *Proc Natl Acad Sci* 2012, **109**(10)**:** 3699-3704.

55. O' Neill PL. Polycrystalline echinoderm calcite and its fracture mechanics. *Science* 1981, **213**(4508)**:** 646-648.

56. Towe KM. Echinoderm calcite: single crystal or polycrystalline aggregate. *Science* 1967, **157**(3792)**:** 1048-1050.

57. Currey JD, Nichols D. Absence of organic phase in echinoderm calcite. *Nature* 1967, **214**(5083)**:** 81.

58. Berman A, Hanson J, Leiserowitz L, Koetzle TF, Weiner S, Addadi L. Biological control of crystal texture - a widespread strategy for adapting crystal properties to function. *Science* 1993, **259**(5096)**:** 776-779.

59. Oliver WC, Pharr GM. An improved technique for determining hardness and elastic modulus using load and displacement sensing indentation experiments. *J Mater Res* 1992, **7**(6)**:** 1564-1583.

60. Oliver WC, Pharr GM. Measurement of hardness and elastic modulus by instrumented indentation: advances in understanding and refinements to methodology. *J Mater Res* 2004, **19**(1)**:** 3-20.

61. Asenath-Smith E, Li H, Keene EC, Seh ZW, Estroff LA. Crystal Growth of Calcium Carbonate in Hydrogels as a Model of Biomineralization. *Adv Funct Mater* 2012, **22**(14)**:** 2891-2914.

62. Nabarro FRN. The mechanical properties of metallic solid solutions. *Proceedings of the Physical Society* 1946, **58**(6)**:** 669.

63. Cohen M, Baker W. *Materials and Man's Needs*. National Academy of Sciences: Washington, D.C., 1974.

CHAPTER 2

2 EVALUATION OF STRENGTHENING MECHANISMS IN CALCITE SINGLE CRYSTALS FROM MOLLUSK SHELLS*

2.1 Abstract

Biogenic single crystal calcite is often reported to be harder and tougher than geologic calcite in the form of Iceland spar. However, the mechanistic origins of the superior mechanical properties of the biogenic materials are still debated. We investigate the hardness and modulus of biogenic calcite from the prismatic layer of the mollusk, *Atrina rigida,* compared with a pure geologic calcite, Iceland spar. On the {001} face, biogenic calcite is found to be 50 to 70% harder than geologic calcite. This range is due to the fact that changes in azimuthal angle of the indenter tip lead to a hardness variation of ~20% in *Atrina rigida* but only ~7% in Iceland spar. The higher hardness and increased anisotropy of biogenic calcite could be accounted for by hardening mechanisms based on hindered dislocation motion rather than crack deflection.

2.2 Introduction

Biomineralized tissues are hierarchically-organized composites that are often reported to be stronger and tougher than their inorganic constituents.[1-5] However, the mechanical properties of these constituents are rarely measured because of their small size, and the measurements that do exist are widely scattered.[6-9] Therefore, understanding the mechanical properties of biogenic composites requires understanding the

* Portions reproduced with permission from M. E. Kunitake, L. M. Mangano, J. M. Peloquin, S. P. Baker, L. A. Estroff, *Acta Biomaterialia,* **2013**, 9 (2), 5353-5359. Copyright 2012 Acta Materialia Inc.

microstructure, properties, and morphologies of the individual constituents at all appropriate length scales. As a model system, we compare the structure and mechanical properties of individual calcite single crystals from the outer shell of the mollusk, *Atrina rigida,* with those of a pure geologic calcite single crystal, Iceland spar.

Biomineralized structures such as mollusk shells are comprised of small mineral crystals embedded within a polymer matrix. The mechanical properties of these composites are typically evaluated using a classic engineering approach in which both phases are assumed to be homogeneous and the properties of pure single crystals are used to describe the mineral.[3, 4] However, the individual, mineral building blocks in biological tissues are often *themselves* composites. Analyses of large biogenic crystals have shown up to several weight percent of organic biomacromolecules trapped *within* the crystals.[10-15] These occluded biopolymers are thought to toughen the biogenic minerals.[16] In addition, multiple characterization techniques have revealed, in a range of biogenic crystals, the presence of a "granular" sub-structure, which may be a remnant of a formation process that begins from an amorphous precursor.[17, 18] Despite all of this evidence that individual biogenic crystals cannot be treated as homogenous, pure crystals, very little work has been done to quantitatively evaluate their mechanical properties.[6, 8, 19, 20]

The focus of the current study is the outer shell of the bivalve, *Atrina rigida* (Figure 2.1a).[12] The shell of this mollusk is comprised of two layers, each containing mineral crystals surrounded by water-insoluble, organic matrices. In the inner nacreous layer, the mineral is in the form of aragonite "tablets" and in the outer prismatic layer the mineral is in the form of elongated single-crystal "prisms" of calcite (Figure 2.1b). In the

prismatic layer, the individual prisms are oriented with their long axes (the crystallographic *c* axis) perpendicular to the shell surface (Figure 2.1c). Each prism diffracts x-rays as a single crystal with coherence lengths similar to those measured for geologic calcite (from hundreds of nanometers to several micrometers).[21, 22] Recent TEM studies have further confirmed that *Atrina* prisms, in contrast to prisms from other mollusk species, can be treated as single crystals.[23] In addition, compositional analysis reveals that *within* each prism, there are both inorganic impurities, in particular Mg^{2+}, and organic macromolecules, including chitin and members of the Asprich protein family.[11, 12] Based upon evidence from x-ray coherence length measurements, small angle x-ray scattering and annular dark field scanning transmission electron microscopy and tomography, the *intra*-crystalline biomacromolecules are incorporated in the form of flattened disks that lie parallel to {001} planes.[10, 21, 24]

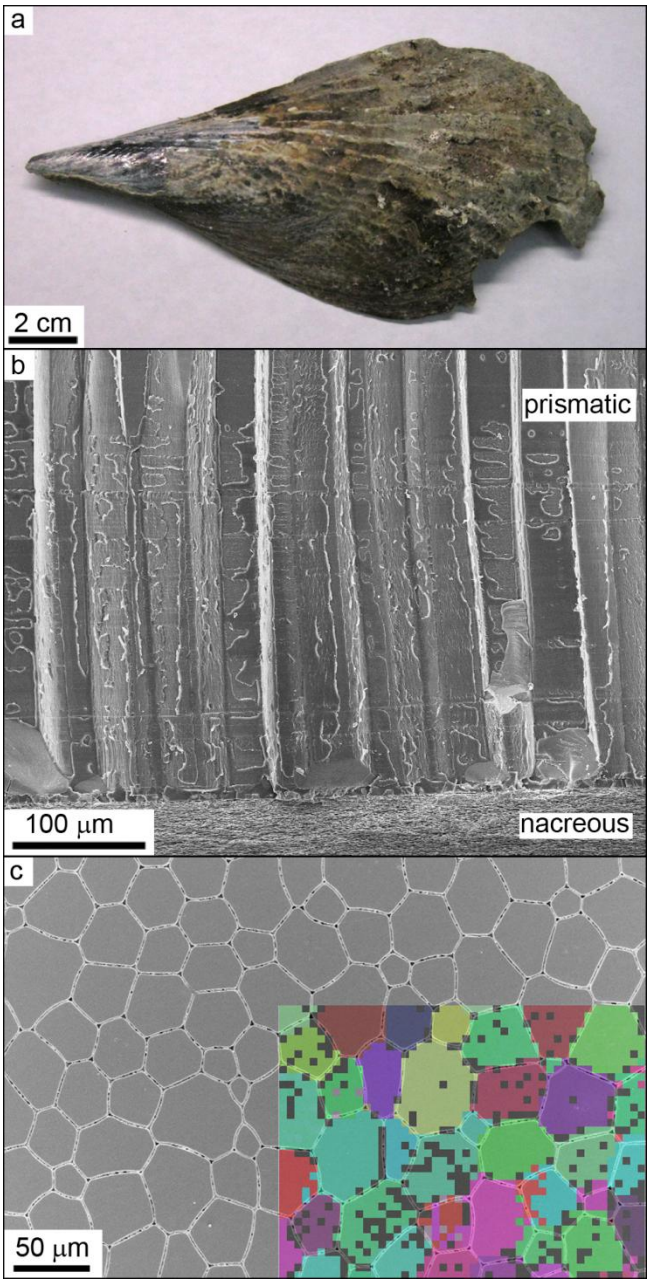

Figure 2.1 a.) Photograph of an *Atrina rigida* shell. b.) Scanning electron micrograph of a cross-section of the shell showing the larger columnar prismatic layer (top) and smaller plate-like nacreous layer (bottom). c.) Top view of a polished prismatic layer with an overlay of the EBSD map used to determine crystallographic orientation. The color of each 5 µm by 5 µm pixel is generated by plotting the three Euler angles that correlate the calcite crystal orientation at that location to a constant reference coordinate system as red,

green, and blue color intensities. The interprismatic organic matrix has been damaged by the EBSD electron beam in this image and appears bright.

To fully understand the origins of the superior mechanical properties of biogenic materials, the properties of individual building blocks, such as the individual prisms in *Atrina rigida*, must be determined. In this paper, we present results of a detailed study of the hardness and indentation modulus of the prisms, along with qualitative observations of fracture. Because the prisms are small (< 100 μm in diameter and up to several hundred μm long), we use nanoindentation to determine the properties of individual single crystals. We conducted identical experiments on single crystal Iceland spar, a pure (<1 wt% inorganic impurities) form of calcite, as a reference (Figure 2.2a). We note that very few comparable experiments have been performed for either biogenic or geologic calcite and that the previously reported data are very scattered.[6, 9] For example, the hardness of single crystal Iceland spar, indented on {104} faces, has been reported to be 1 to 3 GPa,[6, 25, 26] while the hardness of biogenic calcite single crystals, indented in a range of orientations, spans from 2.2 to 5 GPa.[6-9] While it is well known that calcite is anisotropic,[27-32] the effects of this anisotropy on Berkovich indentation values has, to the best of our knowledge, not been evaluated. In the present work we account for this anisotropy and find it to be significant.

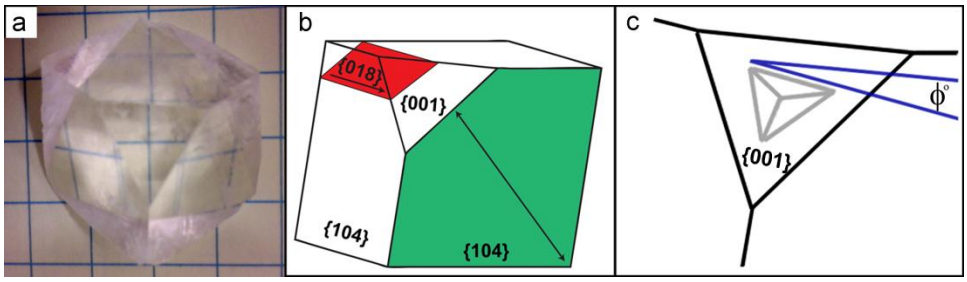

Figure 2.2 a) Polished geologic calcite crystal on a ¼ in. grid. A {001} plane is exposed for nanoindentation. b) Schematic illustration of a calcite crystal relating the {001} indentation plane with the {104} slip system and the {018} twin system. c) Schematic illustration showing the reference $\phi = 0°$ orientation of a 3-fold symmetric Berkovich tip relative to a calcite crystal.

2.3 Experimental Design

We chose to indent the prisms on their naturally exposed surface, *i.e.*, the {001} plane (Figure 2.1c), since this orientation is the biologically relevant wear surface at the exterior of the mollusk shell. We polished the geologic calcite crystals to expose a {001} facet on which to indent so that the results would be directly comparable to the biogenic crystals (Figure 2.2a). The symmetry of the indenter tip must also be taken into account. For this work, we used a 3-fold-symmetric Berkovich tip. When viewed down the *c* axis (normal to the {001} plane), calcite also has a 3-fold axis of symmetry (Figure 2.2). For this reason, the azimuthal angle, ϕ, of the indenter tip with respect to the calcite {001} plane, must be controlled. We define the azimuthal angle to be 0° when the faces of the Berkovich tip, the {001} surface, and the adjacent {104} facets share common zone axes (Figure 2.2c). Due to symmetry, the angles $0° \leq \phi \leq 60°$ will contain all information for this system; however, for completeness, we performed indents at azimuthal angles from 0° to 120° in both the biogenic and geologic calcite crystals. For comparison with

previously published nanoindentation results,[1, 6, 7, 25, 26] we also indented geologic calcite on the naturally occurring {104} cleavage face. Hardness and modulus values were determined at each azimuthal angle.

2.4 Materials and Methods

2.4.1 Specimen Preparation and Characterization

Optically clear geologic calcite rhombohedra (1-2 cm in length; Carolina Biological Supplies GEO3429B) were mechanically polished on the (001) plane to a RMS roughness of less than 10 nm by using a disk grinder followed by graded Al_2O_3 lapping films and a final 50 nm Al_2O_3 powder (Buehler micropolish γ–Al_2O_3) suspended in a water and 2-methyl-2,4-pentanediol mix (Green Lube, Allied High Tech) (Figure 2.2a). A representative sample measured by ion coupled plasma atomic emission spectroscopy (ICP-AES) contained less than 1 wt % inorganic impurities (data not shown).

Atrina rigida (Gulf Specimen Marine Lab, Florida) samples were received fresh and cleaned of sand and other debris. The shells were then placed overnight in 10% NH_4OH, rinsed with DI water, and frozen for storage. One portion (~1 cm x 1 cm) of the frozen shell was then thawed, excised, and embedded in epoxy (Electron Microscopy Sciences Epofix) so that the *c* axis fiber texture of the prismatic layer would be accessible after polishing by the same procedure described for the geologic samples. The sample was then stored at ambient conditions before measurements were taken. Only one shell was chosen for analysis to eliminate variability from organism to organism.

EBSD (Leica StereoScan 440 SEM with Nordlys II EBSD detector) was used to

determine the crystallographic orientation of each individual prism and SEM (Leo 1550 FESEM) was used to image the indentations. For imaging, EBSD samples were coated with amorphous carbon, while SEM samples were coated with Au-Pd. Prior to indentation, the carbon layer was removed by a final polish with the 50 nm Al_2O_3 powder suspended in a water and 2-methyl-2,4-pentanediol mix.

2.4.2 Nanoindentation

Load-displacement measurements were performed using a Berkovich diamond indenter in a commercial nanoindenter system (Hysitron Triboindenter) in quasistatic mode. Prior to data collection, the shape of the tip was calibrated.[33] It had a tip radius of ~120 nm. Each indent consisted of five second load, hold, and unload segments with the unloading segment used to calculate the indentation modulus and hardness (Figure 2.3).[33]

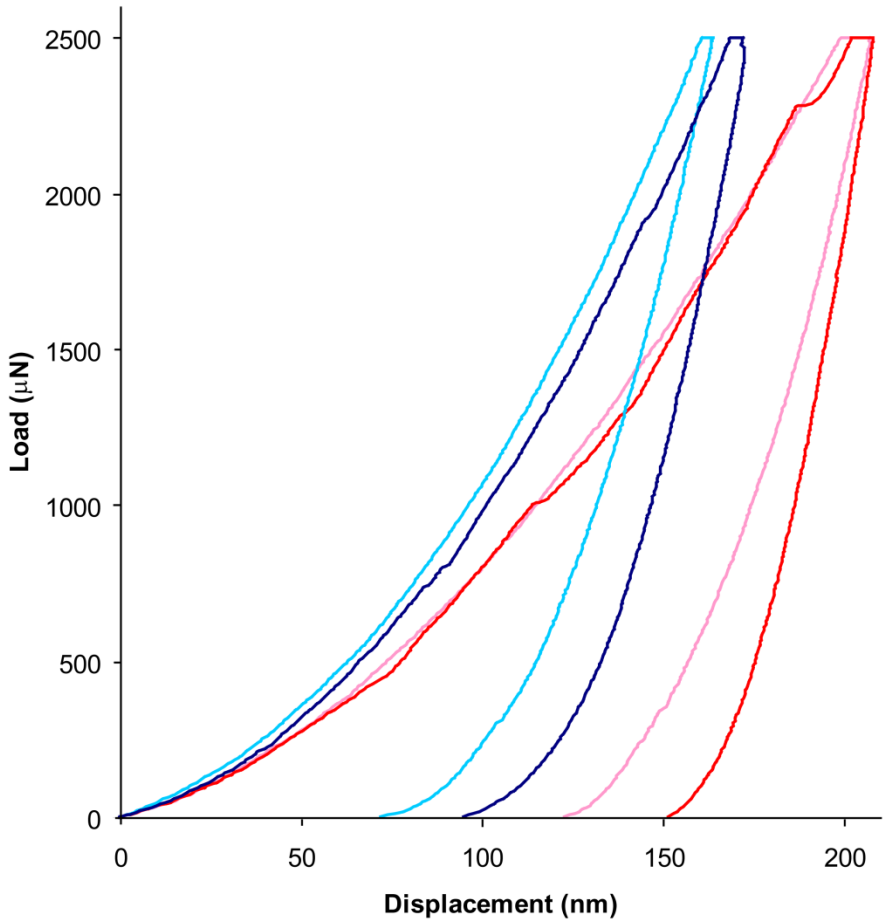

Figure 2.3 Representative load displacement graphs for Atrina rigida and geologic calcite. Atrina rigida: 0° dark blue, 60° light blue. Geologic: 0° red, 60° pink. The maximum depth and amount of creep is less for Atrina rigida than geologic calcite.

Indentations were made to a maximum load of 2500 μN, resulting in depths of about 170 nm in *Atrina* prisms and 200 nm in Iceland spar (Table 2 and Figure 2.3). Based upon a survey of loads (data not shown), 2500 μN was chosen as the maximum load to ensure that the indentation depth was significantly larger than the surface features (surface roughnesses were less than 10 nm RMS) and that the sampled volume would

encompass a homogenous representation of the biogenic calcite. The load was also chosen to be small enough to allow for multiple measurements per prism (4-9 indentations were made at each azimuthal angle). Hardness and modulus values were relatively constant in a range from 1500 to 10000 μN in geologic calcite and from 2500 to 10000 μN in *Atrina rigida* (data not shown), so the reported values are expected to be representative. For the {001} face of Iceland spar, arrays of 9 indentations were made at each azimuthal angle. On the {104} face of Iceland spar, arrays of 9 indentations were made in 20 degree azimuthal angle increments, totaling 120 degrees, and the hardness and modulus values are reported as the average of the measured values at each angle.

Table 2 The plane strain indentation modulus and hardness values for biogenic and geologic calcite.

	$E_s/(1-\upsilon_s^2)$ (GPa)		Hardness (GPa)		Indentation Depth (nm)	
	0°	**60°**	**0°**	**60°**	**0°**	**60°**
Biogenic {001} ***Atrina rigida***	74.9 ± 0.7	70.1 ± 1.5	3.47 ± 0.21	4.19 ± 0.27	173 ± 2.1	166 ± 2.1
Geologic {001}	76.9 ± 3.1	67.5 ± 1.1	2.30 ± 0.14	2.46 ± 0.03	203 ± 4.5	199 ± 1.1
Geologic {104}[a]	88.1 ± 1.7		2.54 ± 0.07		182 ± 2.4	

[a]The {104} data is an azimuthal average.

2.4.3 Crystallographic Orientation

For the geologic crystals, the azimuthal angle could be determined optically based upon the crystal morphology (Figure 2.2a). Geologic azimuthal angle data were collected on the single crystal by rotating the specimen beneath the tip in ten-degree increments. The vertex between a {104} and a {001} plane was viewed under the optical microscope

of the nanoindenter and aligned to the indenter tip using the angle measurement function in the microscope software. The initial fixed orientation of the tip was determined by imaging an impression made in a fused silica reference.

For the *Atrina* prisms, with their {001} fiber texture, electron back-scattered diffraction (EBSD) was used to determine both the *c* axis orientation and the in-plane orientation (azimuthal angle) for individual prisms (Figure 2.1c). Only prisms whose *c* axes were within 5° of the surface normal were selected for indentation. The orientation in the *a-b* plane for each of these prisms was determined, and coupled with knowledge of the tip orientation, used to determine the azimuthal angle for each prism. A range of prism orientations were chosen to sample the entire 0°-120° range. The embedded and polished shell sample was notched with two reference alignment marks to retain azimuthal angles when transferring between the EBSD microscope and nanoindenter. Reported azimuthal angles are estimated to be accurate to ± 1°.

2.5 Results

The hardness for both *Atrina* prisms and Iceland spar, indented on the {001} face, varies with azimuthal angle, ϕ (Figure 2.4 and Table 2). For both materials, the lowest values are found near $\phi = 0^{\circ}$ and the highest at $\phi = 60^{\circ}$. The hardness varies 21% and 7% with ϕ for *Atrina* prisms and Iceland spar, respectively. In addition, at all ϕ, the hardness values are significantly higher for the biogenic crystals. The prisms are 51% harder than Iceland spar at $\phi = 0^{\circ}$ and 70% harder at $\phi = 60^{\circ}$. The uncertainty in the hardness values was significantly greater in the biogenic material. Indentions on the {104} face of Iceland spar returned hardness values (Table 2) similar to those found in other nanoindentation experiments that were conducted on the {104} face.[1, 6, 7, 25, 26]

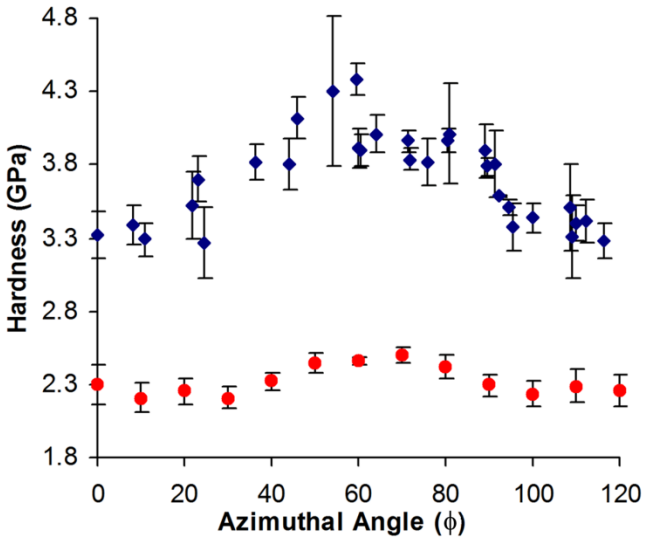

Figure 2.4 Plot of hardness as a function of azimuthal angle for Atrina rigida (blue diamonds) and geologic calcite (red circles). Each azimuthal angle is an average of 9 to 27 indents for the geologic sample or 4 to 8 indents for the biogenic sample. Error bars represent one standard deviation.

In contrast to the hardness, the indentation modulus values (Table 2 and Figure 2.5) for *Atrina* prisms and Iceland spar are similar and vary by only about 10% with ϕ. The variation with ϕ is consistent with the 3-fold symmetry of both the indenter tip and the (001) face of calcite. The fact that the values are the same for both biogenic and geologic material indicates that the concentrations of impurities and defects in the biogenic material are not high enough to significantly affect the modulus. Overall, the higher variability in the modulus data from the *Atrina* prisms can be attributed to the smaller number of indents per prism and greater inhomogeneity of that material. The fact that the variability is higher at lower ϕ values, particularly in the Iceland spar, can be attributed to cracking.

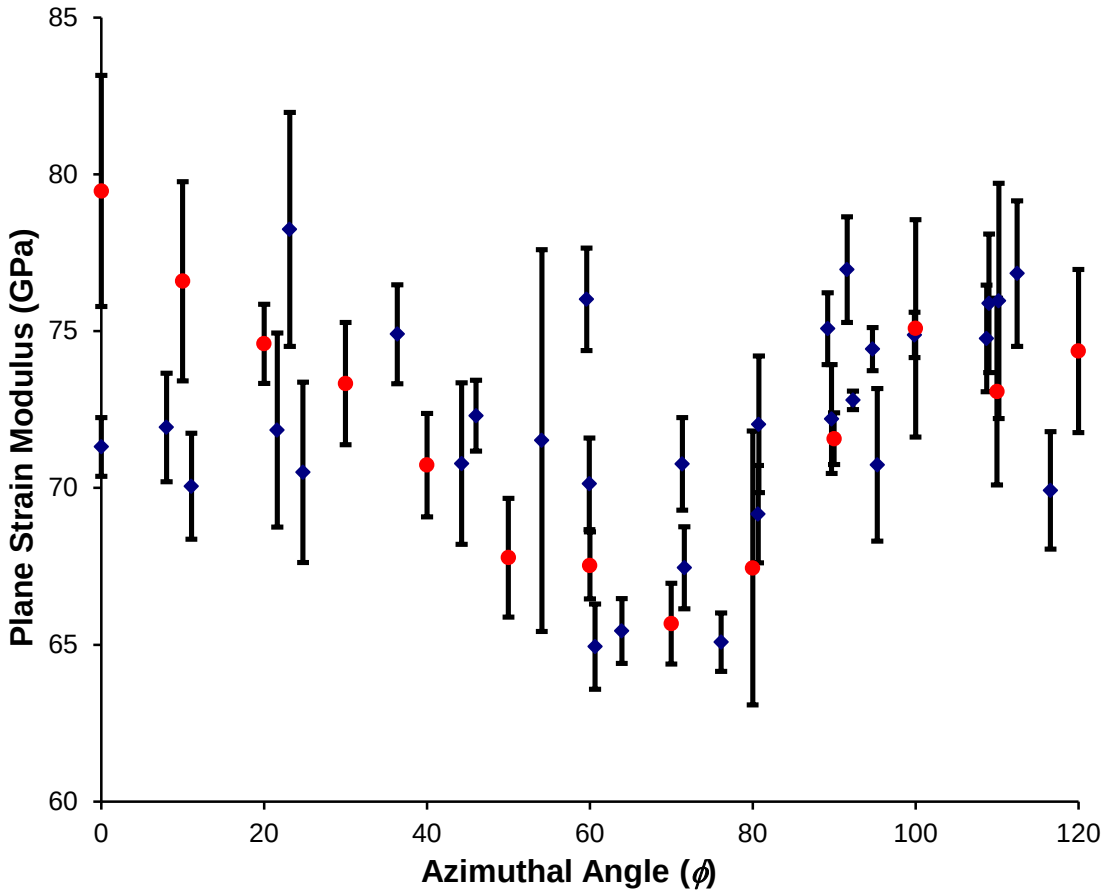

Figure 2.5 Plot of plane strain indentation modulus as a function of azimuthal angle for Atrina rigida (blue diamonds) and geologic calcite (red circles). Each azimuthal angle is an average of 9 to 27 indents for the geologic sample or 4 to 8 indents for the biogenic sample. Error bars represent one standard deviation.

Modulus values from indentations on the {104} face of the geologic material were found to be ~10% higher than values reported in previous studies.[1, 6, 7, 25, 26] However, caution should be exercised in directly comparing modulus values obtained from nanoindentation experiments because it is often unclear which modulus is being reported. In the standard analysis, the plane strain modulus of the sample, $E_s \big/ (1-\upsilon_s^2)$,

and the plane strain modulus of the indenter tip, $E_t \big/ (1-\upsilon_t^2)$, combine to form the "reduced modulus," E_r, following:

$$\frac{1}{E_r} = \frac{1-\nu_s^2}{E_s} + \frac{1-\nu_t^2}{E_t} \qquad [1]$$

where E and ν are Young's modulus and Poisson's ratio, and the subscripts s and t refer to the sample and tip materials, respectively. Different groups report E_r, E_s (sometimes referred to as E_{it}), or $E_s \big/ (1-\upsilon_s^2)$, as the modulus. We report the plane strain indentation modulus, $E_s \big/ (1-\upsilon_s^2)$, since this value is the sample-specific modulus obtained in a nanoindentation experiment. E_r includes the elastic properties of the tip, and reporting E_s requires making some assumption about Poisson's ratio, which is highly anisotropic in calcite.[34] We thus view our modulus values as being similar to those previously reported.

Finally, the fracture response of both biogenic and geologic calcite was dependent on azimuthal orientation. SEM images of indentations in both materials showed multiple fractures for ϕ near 0°, and virtually no fracture for ϕ near 60° (Figure 2.6). At higher loads, it becomes apparent that there is more cracking in Iceland spar at ϕ=0° (Figure 2.7).

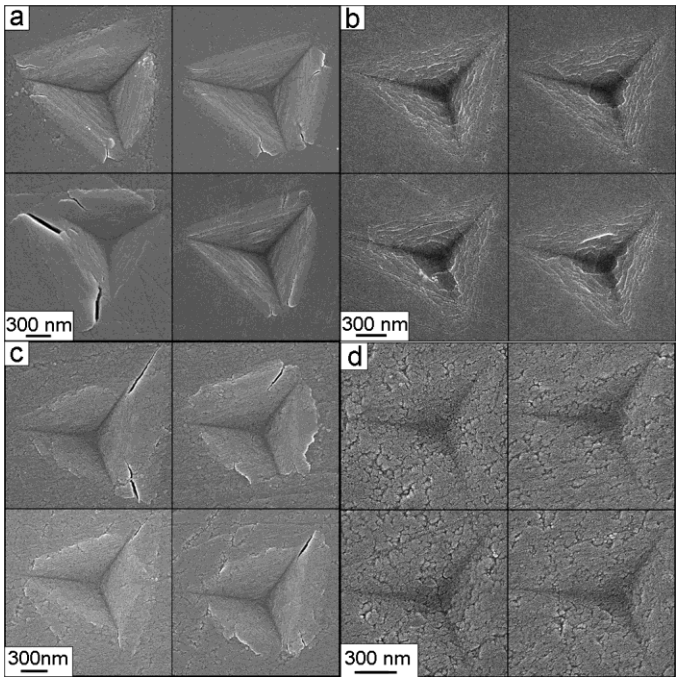

Figure 2.6 Representative SEM images of 2500 μN indents of: a) Geologic 0° b) Geologic 60° c) Atrina rigida 4.1° d) Atrina rigida 60°. RMS roughnesses for both geologic and biogenic surfaces were measured by the nanoindenter to be <10 nm. Any apparent difference in surface texture between the images in (c) and (d), which are taken from the same sample, is a result of a higher magnification and grey level-adjustment to enhance the contrast in (d) to better image the indents.

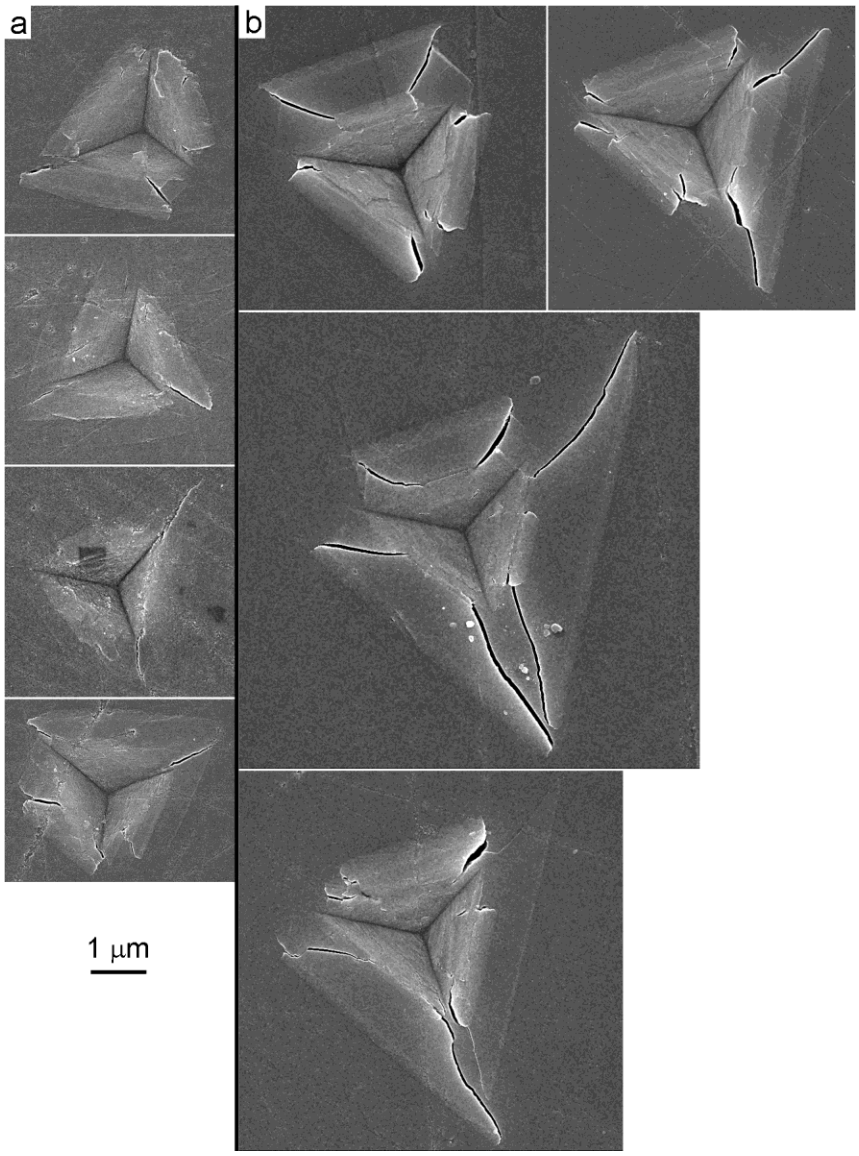

Figure 2.7 Representative SEM images of 8500 μN indents scaled to the same magnification: a) Atrina rigida 0° b) Geologic 0°. Although the indents are roughly the same size, the fracture length of the geologic samples is greater.

2.6 Discussion

2.6.1 Plastic Deformation in Geologic and Biogenic Calcite

Calcite is an ionic crystal and fractures easily in tension. However, in compression or shear, calcite readily deforms plastically, even at room temperature. For plastic deformation of a crystal there are only two possible mechanisms, dislocation motion and/or mass transport. The presence of small amounts (by weight or volume) of organic macromolecules and/or voids within the crystal does not make any new mechanisms possible. The biogenic crystals, therefore, still have to deform by one of these two mechanisms. Since there is no evidence for high diffusion rates in calcite at room temperature under and near the indenter, dislocation motion is the only possible plastic deformation mechanism for both the geologic and biogenic calcite crystals.

In uniaxial compression, Iceland spar has been shown to deform plastically by slip on {104} and {012} planes and by twinning on {018} planes (Figure 5) [30, 35] at pressures much lower than those found under an indenter tip (0.5 or 1.0 GPa [30] *vs.* 2.5 to 4 GPa (Figure 2.4 and Table 2). It is therefore unsurprising that plastic deformation occurs in calcite during hardness testing. The residual impressions left after an indentation test in calcite single crystals (Figure 2.6 and Figure 2.7), whether biogenic or geologic, necessarily arise from dislocation motion on the available slip planes. Indeed, SEM images of indentations made using higher loads (8500 μN) (Figure 2.7) show that regions of material have slipped up and out along the expected, well-defined crystallographic planes.

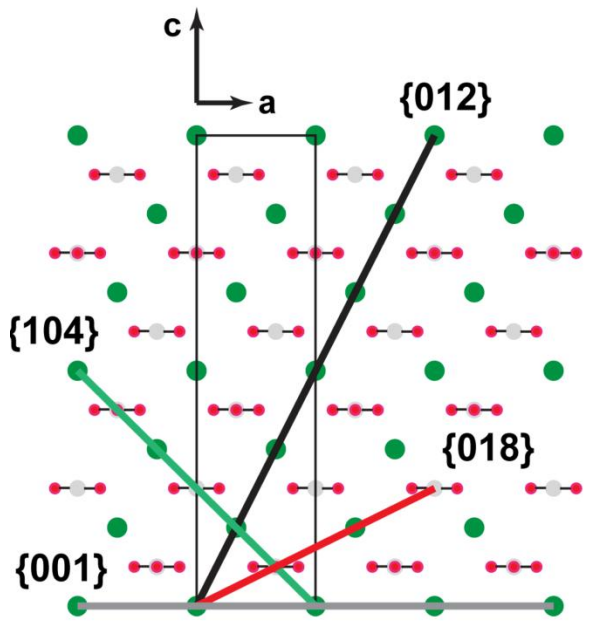

Figure 2.8 Calcite atomic structure (green filled circles: calcium; red filled circles: oxygen; grey filled circles: carbon) showing the {001} indentation plane (grey line), the {104} and {012} slip systems (green and black lines, respectively), and the {018} twin system (red line).

2.6.2 Angular Variation in Hardness

The limited number of slip systems available leads to anisotropy in the plastic response of calcite. Hardness anisotropy in single crystals, in general, is well-known and has been studied in calcite using Knoop and Vickers micro-indenters, whose four-fold symmetries do not match the symmetry of the crystal faces in calcite, making interpretation of these data difficult.[29, 36-38] In our case, the three-fold symmetry of the Berkovich nanoindenter matches the three-fold symmetry of the (001) face of calcite (Figure 2.2c), allowing a conceptually simple evaluation of the variations in hardness and

fracture with azimuthal angle based on slip-system geometry, without need to assume a particular stress state.

When the indenter is in the $\phi = 0^\circ$ orientation, three planes are favorably oriented to accommodate deformation in the material adjacent to each indenter face with a minimum of dislocation activity: {104} and {012} primary slip planes, and a {018} twin plane. In contrast, at $\phi = 60^\circ$, {018} twinning is suppressed and deformation adjacent to each face requires the coordinated motion of two sets of both {104} and {012} slip planes, or slip on less-favorably oriented planes, requiring necessarily more dislocation line length and more dislocation interactions. Thus the 60˚ orientation is expected to be harder than the 0˚ orientation, in agreement with our data for both geologic and biogenic calcite.

The ϕ-dependence of fracture also contributes to the ϕ-dependence of the calculated hardness values. The "easy" slip systems at $\phi = 0°$ are all facilitated by radial cracking at the indenter edges, and indeed both geologic and biogenic calcite show more fracture near this orientation (Figure 2.6 and Figure 2.7). Since fracture facilitates additional permanent deformation beneath the indenter, it further reduces the hardness values near $\phi = 0°$.

2.6.3 Comparison of Biogenic and Geologic Materials

The higher hardness of the biogenic calcite single crystals in *Atrina rigida* prisms compared to that of the geologic Iceland spar (Figure 2.4) can be attributed to four possible sources: solid-solution strengthening due to Mg^{2+} substitutionals, composite strengthening due to occluded macromolecules, strengthening due to residual defects that arise as a result of the formation process, and differences in fracture toughness.[6, 8, 16, 20, 39-

41

Magnesium is well-known to substitute for calcium in calcite [42-44] and is commonly found in biogenic calcite, including 0.4 to 1 at% in the *Atrina* prisms.[11, 45] Recent computational studies [46, 47] suggest that the lattice distortions around Mg^{2+} substitutionals are significant, and such distortions would hinder dislocation movement through the crystals, resulting in an increased hardness. Due to the structural complexity and multiple impurities in biogenic calcite, it has been difficult to establish clear correlations between experimental measurements of Mg^{2+} concentration and the hardness of biogenic calcite.[8, 16, 39-41] However, we have recently identified a correlation between magnesium content and hardness in synthetic calcite.[45] Based upon those measurements, the magnesium content in *Atrina* prisms could account for ~20 to 50% of the observed increase in hardness.

It is well-known that the presence of the occluded macromolecules significantly changes the appearance of fracture surfaces and indirect evidence suggests that occluded macromolecules increase the fracture toughness.[13, 16] Even though the macromolecules themselves are unlikely to be particularly resistant to shearing (at least for small plastic strains) the lower stiffness regions associated with the presence of the macromolecule inclusions should attract dislocations and increase the hardness.

The formation mechanism of the prismatic layer in bivalves is still under investigation and may occur via the agglomeration of amorphous calcium carbonate particles.[12, 18] Most of the indirect evidence for such a mechanism comes from genera other than *Atrina*. For example, phase-contrast AFM images of polished and gently etched prismatic layers from *Pinna nobilis*, *Haliotis rufescens,* and *Pinctada*

margaritifera all show 50-60 nm sized grains surrounded by a thin (~8 nm thick) layer.[48] In other work, x-ray absorption spectroscopy suggests that prisms from *Pinctada fucata* are composed of many crystallographically mis-aligned nanoparticles.[49] Finally, a recent comparative study of multiple prismatic layers using x-ray diffraction and TEM techniques suggests that prisms from *Pinctada fucata* and *Crassostrea nippona* have a "sub-grain structure", whereas prisms from *Atrina pectinata* do not.[23] Interestingly, SEM images of the growing prismatic layer of *Atrina rigida* suggest the initial deposition of 50-100 nm sized particles. What remains unclear is how such particles can coalesce into "good" (as assessed by x-ray and TEM) single crystals of calcite.[12] The existence of any sort of sub-grain structure within a single crystal requires that dislocations exist on the boundaries. Other defects (e.g., vacancies, impurity atoms) may also accumulate there. These defects would interact with dislocations to strengthen the material.

Finally, it is worthwhile to consider the effect of fracture on the difference in hardness between the biogenic and geologic samples. For a given material, the measured hardness values would be expected to decrease as the extent of fracture increases. Since the geologic material fractures more at $\phi = 0^{\circ}$, and neither material fractures at $\phi = 60^{\circ}$, if fracture were the cause of the measured difference in hardness, that greatest difference would be at $\phi = 0^{\circ}$. However, the largest difference was at $\phi = 60^{\circ}$. Thus, the other strengthening mechanisms cannot be independent of ϕ, and in fact must make the biogenic material more (plastically) anisotropic than the geologic one.

2.7 Conclusions

We have shown individual calcite single crystal prisms from the mollusk Atrina rigida to be significantly harder and tougher (as inferred from the extent of cracking

under identical conditions) than the geologic calcite single crystal reference (Iceland spar). After accounting for anisotropy, the biogenic crystals, indented along the <001> axis, are 51 to 70 % harder than geologic Iceland spar, indented along the same direction, depending on the azimuthal angle. While the relative contributions are unknown, the difference in hardness could be attributed to a combination of Mg^{2+} solid-solution strengthening, occluded macromolecules, residual defects from the formation process, and fracture. These results suggest that single-crystal geologic refererence materials are a poor analogue for the inorganic constituents in biomineralized tissues. Therefore the actual properties of these building blocks, including anisotropy, should be accounted for in models of tissue properties and function.

The range of hardness values in our study spans approximately 45% of the reported variation in hardness values for all forms of calcite. A significant fraction of the previously reported variation, therefore, can be accurately attributed to anisotropy and the four strengthening mechanisms discussed here. Differences in composition and structure in biogenic calcite occur with genera, species, environmental conditions where the calcite was formed, age of individual specimens, and anatomic location of the sample,[6, 9] and may account for the remaining variations. Further work, therefore, is needed to fully understand the variations in mechanical properties of biogenic single crystals. Insights gained from the current work can provide design strategies for generating synthetic materials from single crystals with tailored mechanical properties.

2.8 Acknowledgements

We acknowledge support from NSF (DMR 0845212), the J. D. Watson Investigator Program (NYSTAR Contract #C050017), the Cornell Center for Materials

Research (CCMR), a Materials Research Science and Engineering Center of the National Science Foundation (DMR 1120296), the GI Bill (Chapter 33), Hysitron Inc., and Engineering Learning Initiatives (Cornell College of Engineering). Particular acknowledgement is made of the use of the Electron Microscopy facility of CCMR. We would also like to thank Dr. Michael Rutzke for ICP-AES data and Dr. Ellen Keene for shell preparation. Supporting information is available from Elsevier or from the authors.

1. Ma YR, Cohen SR, Addadi L, Weiner S. Sea urchin tooth design: an "all-calcite" polycrystalline reinforced fiber composite for grinding rocks. *Adv Mater* 2008, **20**(8)**:** 1555-1559.

2. Aizenberg J, Weaver JC, Thanawala MS, Sundar VC, Morse DE, Fratzl P. Skeleton of *Euplectella* sp.: structural hierarchy from the nanoscale to the macroscale. *Science* 2005, **309**(5732)**:** 275-278.

3. Jackson AP, Vincent JFV, Turner RM. The mechanical design of nacre. *Proc R Soc Lond Ser B-Biol Sci* 1988, **234**(1277)**:** 415-440.

4. Kamat S, Su X, Ballarini R, Heuer AH. Structural basis for the fracture toughness of the shell of the conch *Strombus gigas*. *Nature* 2000, **405**(6790)**:** 1036-1040.

5. Bruet BJF, Song J, Boyce MC, Ortiz C. Materials design principles of ancient fish armour. *Nat Mater* 2008, **7**(9)**:** 748-756.

6. Merkel C, Deuschle J, Griesshaber E, Enders S, Steinhauser E, Hochleitner R*, et al.* Mechanical properties of modern calcite (*Mergerlia truncata*) and phosphate-shelled brachiopods (*Discradisca stella* and *Lingula anatina*) determined by nanoindentation. *J Struct Biol* 2009, **168**(3)**:** 396-408.

7. Presser V, Gerlach K, Vohrer A, Nickel KG, Dreher WF. Determination of the elastic modulus of highly porous samples by nanoindentation: a case study on sea urchin spines. *J Mater Sci* 2010, **45**(9)**:** 2408-2418.

8. Moureaux C, Pérez-Huerta A, Compère P, Zhu W, Leloup T, Cusack M*, et al.* Structure, composition and mechanical relations to function in sea urchin spine. *J Struct Biol* 2010, **170**(1)**:** 41-49.

9. Pérez-Huerta A, Cusack M, Zhu W. Assessment of crystallographic influence on material properties of calcite brachiopods. *Mineral Mag* 2008, **72**(2)**:** 563-568.

10. Li H, Xin HL, Kunitake ME, Keene EC, Muller DA, Estroff LA. Calcite prisms from mollusk shells (*Atrina rigida*): swiss-cheese-like organic–inorganic single-

crystal composites. *Adv Funct Mater* 2011**:** 2028-2034.

11. Pokroy B, Fitch AN, Marin F, Kapon M, Adir N, Zolotoyabko E. Anisotropic lattice distortions in biogenic calcite induced by intra-crystalline organic molecules. *J Struct Biol* 2006, **155**(1)**:** 96-103.

12. Nudelman F, Chen HH, Goldberg HA, Weiner S, Addadi L. Spiers memorial lecture: lessons from biomineralization: comparing the growth strategies of mollusc shell prismatic and nacreous layers in *Atrina rigida*. *Faraday Discuss* 2007, **136:** 9-25.

13. Aizenberg J, Hanson J, Koetzle TF, Weiner S, Addadi L. Control of macromolecule distribution within synthetic and biogenic single calcite crystals. *J Am Chem Soc* 1997, **119**(5)**:** 881-886.

14. Gries K, Kröger R, Kübel C, Fritz M, Rosenauer A. Investigations of voids in the aragonite platelets of nacre. *Acta Biomater* 2009, **5**(8)**:** 3038-3044.

15. Seto J, Zhang Y, Hamilton P, Wilt F. The localization of occluded matrix proteins in calcareous spicules of sea urchin larvae. *J Struct Biol* 2004, **148**(1)**:** 123-130.

16. Aizenberg J, Hendler G. Designing efficient microlens arrays: lessons from Nature. *J Mater Chem* 2004, **14**(14)**:** 2066-2072.

17. Weiner S, Addadi L. Crystallization pathways in biomineralization. *Annu Rev Mater Res* 2011, **41:** 21-40.

18. Addadi L, Raz S, Weiner S. Taking advantage of disorder: amorphous calcium carbonate and its roles in biomineralization. *Adv Mater* 2003, **15**(12)**:** 959-970.

19. Kearney C, Zhao Z, Bruet BJF, Radovitzky R, Boyce MC, Ortiz C. Nanoscale anisotropic plastic deformation in single crystal aragonite. *Phys Rev Lett* 2006, **96**(25).

20. Pérez-Huerta A, Cusack M, Zhu W, England J, Hughes J. Material properties of brachiopod shell ultrastructure by nanoindentation. *J R Soc Interface* 2007, **4**(12)**:** 33-39.

21. Pokroy B, Fitch AN, Zolotoyabko E. The microstructure of biogenic calcite: A view by high-resolution synchrotron powder diffraction. *Adv Mater* 2006, **18**(18)**:** 2363-2368.

22. Berman A, Hanson J, Leiserowitz L, Koetzle TF, Weiner S, Addadi L. Biological control of crystal texture - a widespread strategy for adapting crystal properties to function. *Science* 1993, **259**(5096)**:** 776-779.

23. Okumura T, Suzuki M, Nagasawa H, Kogure T. Microstructural variation of biogenic calcite with intracrystalline organic macromolecules. *Cryst Growth Des* 2011, **12**(1)**:** 224-230.

24. Gilow C, Zolotoyabko E, Paris O, Fratzl P, Aichmayer B. Nanostructure of biogenic calcite crystals: a view by small-angle x-ray scattering. *Cryst Growth Des* 2011, **11**(6)**:** 2054-2058.

25. Broz ME, Cook RF, Whitney DL. Microhardness, toughness, and modulus of Mohs scale minerals. *Am Mineral* 2006, **91**(1)**:** 135-142.

26. Zugner S, Marquardt K, Zimmermann I. Influence of nanomechanical crystal properties on the comminution process of particulate solids in spiral jet mills. *Eur J Pharm Biopharm* 2006, **62**(2)**:** 194-201.

27. Barber DJ, Wenk HR, Gomez-Barreiro J, Rybacki E, Dresen G. Basal slip and texture development in calcite: new results from torsion experiments. *Phys Chem Miner* 2007, **34**(2)**:** 73-84.

28. Bragg WHS. *X-rays and crystal structure* G. Bell and Sons, Ltd: London, 1915.

29. Carter GM, Henshall JL, Wakeman RJ. Knoop hardness and fracture anisotropy of calcite. *J Mater Sci Lett* 1993, **12**(6)**:** 407-410.

30. Turner FJ, Griggs DT, Heard H. Experimental deformation of calcite crystals. *Geol Soc Am Bull* 1954, **65**(9)**:** 883-933.

31. Taylor EW. Correlation of Mohs's scale of hardness with the Vickers's hardness numbers. *Am Mineral* 1949, **34**(9-10)**:** 718-721.

32. Bass JD. Elasticity of minerals, glasses, and melts. *Mineral physics & crystallography: a handbook of physical constants*, vol. 2. AGU: Washington, DC, 1995, pp 45-63.

33. Oliver WC, Pharr GM. Measurement of hardness and elastic modulus by instrumented indentation: advances in understanding and refinements to methodology. *J Mater Res* 2004, **19**(1)**:** 3-20.

34. Aouni N, Wheeler L. Auxeticity of calcite and aragonite polymorphs of $CaCO_3$ and crystals of similar structure. *Phys Status Solidi B* 2008, **245**(11)**:** 2454-2462.

35. DeBresser JHP, Spiers CJ. Strength characteristics of the r, f, and c slip systems in calcite. *Tectonophysics* 1997, **272**(1)**:** 1-23.

36. Winchell H. The Knoop microhardness tester as a mineralogical tool. *Am Mineral* 1945, **30**(9-10)**:** 583-595.

37. Wong TY, Bradt RC. Microhardness anisotropy of single crystals of calcite, dolomite and magnesite on their cleavage planes. *Mater Chem Phys* 1992, **30**(4)**:** 261-266.

38. Brookes CA, Oneill JB, Redfern BAW. Anisotropy in hardness of single crystals. *Proc R Soc Lond Ser A-Mat* 1971, **322**(1548)**:** 73-88.

39. Long X, Ma Y, Qi L. In vitro synthesis of high Mg calcite under ambient conditions and its implication for biomineralization process. *Cryst Growth Des* 2011, **11**(7)**:** 2866-2873.

40. Wang RZ, Addadi L, Weiner S. Design strategies of sea urchin teeth: structure, composition and micromechanical relations to function. *Phil Trans R Soc B* 1997, **352**(1352)**:** 469-480.

41. Griesshaber E, Schmahl WW, Neuser R, Pettke T, Blum M, Mutterlose J*, et al.* Crystallographic texture and microstructure of terebratulide brachiopod shell calcite: An optimized materials design with hierarchical architecture. *Am Mineral* 2007, **92**(5-6)**:** 722-734.

42. Davis KJ, Dove PM, Wasylenki LE, De Yoreo JJ. Morphological consequences of differential Mg^{2+} incorporation at structurally distinct steps on calcite. *Am Mineral* 2004, **89**(5-6)**:** 714-720.

43. Paquette J, Reeder RJ. Relationship between surface structure, growth mechanism, and trace element incorporation in calcite. *Geochim Cosmochim Ac* 1995, **59**(4)**:** 735-749.

44. Anovitz LM, Essene EJ. Phase equilibria in the system $CaCO_3$-$MgCO_3$-$FeCO_3$. *J Petrol* 1987, **28**(2)**:** 389-415.

45. Kunitake ME, Baker SP, Estroff LA. The effect of magnesium substitution on the hardness of synthetic and biogenic calcite. *MRS Communications* 2012, **2**(03)**:** 113-116.

46. Stashans A, Chamba G. A new insight on the role of Mg in calcite. *Int J Quantum Chem* 2011, **111**(10)**:** 2436-2443.

47. Elstnerova P, Friak M, Fabritius HO, Lymperakis L, Hickel T, Petrov M*, et al.* Ab initio study of thermodynamic, structural, and elastic properties of Mg-substituted crystalline calcite. *Acta Biomater* 2010, **6**(12)**:** 4506-4512.

48. Dauphin Y. The nanostructural unity of mollusc shells. *Mineral Mag* 2008, **72**(1)**:** 243-246.

49. Gilbert PUPA, Young A, Coppersmith SN. Measurement of c-axis angular orientation in calcite ($CaCO_3$) nanocrystals using X-ray absorption spectroscopy. *Proc Natl Acad Sci USA* 2011, **108**(28)**:** 11350-11355.

CHAPTER 3

[3] THE EFFECT OF MAGNESIUM SUBSTITUTION ON THE HARDNESS OF SYNTHETIC AND BIOGENIC CALCITE [*]

3.1 Abstract

Biogenic minerals often contain inorganic and organic impurities that are believed to harden and toughen the material. However, because of the complexity of these systems, it is difficult to deconvolute the effect of each of these impurities on the hardness of the material. We have created single-crystal samples with a range of magnesium concentrations and measured their hardness while controlling for orientation. We find that hardness increases linearly with magnesium content and that magnesium impurities could account for ~20% of the increased hardness in biogenic calcite from the mollusk *Atrina rigida* when compared to pure geologic calcite.

3.2 Introduction

Many organisms synthesize amazingly hard and tough functional materials by combining inorganic minerals with organic macromolecules in complex, hierarchical structures.[1] For example, sea urchin teeth, which contain high-magnesium content polycrystalline calcite ($CaCO_3$) embedded in a protein-based matrix, are hard and tough enough to grind limestone rocks.[2] Although biogenic calcite has been reported to be harder than geologic calcite,[3-8] the reasons for the increased hardness are not well understood. Changes in hardness have been speculated to arise from differences in magnesium[3-5, 7, 8] and organic macromolecule content,[4, 6, 7, 9] as well as microstructural

[*] Portions reproduced with permission from M. E. Kunitake, S. P. Baker, L. A. Estroff, *MRS Communications,* **2013**, 2 (3), 113-116. Copyright 2012 Materials Research Society

features including crystallographic texture,[4, 6] crystallite size,[10] and inorganic to organic ratio.[3] However, it is not possible to quantify the relative importance of these compositional and microstructural differences from the existing data, because multiple parameters vary simultaneously between hardness measurements of different biologic systems and even within measurements of a single system.[5, 8]

In previous work,[4] we showed that the hardness of single crystal calcite is sensitive to the orientation of the crystal (both the crystal face indented and the azimuthal angle of the indenter with respect to that face), and that the combination of the mechanisms listed above leads to a hardness for single crystal calcite from the outer shell of the mollusk *Atrina rigida* that is as much as 70% greater than the hardness of a relatively pure geologic single crystal calcite, Iceland spar (at the same orientation). To provide more detailed insight into the effect of magnesium incorporation on the hardness of single crystal calcite, we have produced synthetic samples with excellent control of both composition and microstructure, and investigated their mechanical properties using nanoindentation.

3.3 Experimental Design

We created samples with a range of Mg-concentrations by epitaxially overgrowing synthetic calcite seed crystals with a layer of calcite that contains a gradient in magnesium concentration. The equilibrium solubility of Mg in calcite is about 1 at%.[11] To create a gradient in Mg-concentration, a fixed volume solution of 1 mM:5 mM Mg:Ca is used.[12] As the thermodynamically favorable calcite is deposited, the ratio of magnesium to calcium ions remaining in solution increases, leading to increased magnesium incorporation in the overgrowth with time.

As seed crystals, we chose to use calcite grown in a 1 w/v% agarose hydrogel, which yields samples with uniform size and shape.[13] To orient the seed crystals with their *c* axis perpendicular to the substrate, an array of ~50 μm deep impressions were made in a 1/16th inch thick aluminum sheet (Figure 3.1a) using a home-built cubic zirconia indenter ground and polished to the shape of a calcite rhombohedron, generating an array of oriented sockets for the seed crystals. A single ~75 μm calcite seed was then carefully placed into each impression, letting gravity orient it such that the *c* axis was aligned with the indentation axis (Figure 3.1b). Using a solution of 1 mM $MgCl_2$ and 5 mM $CaCl_2$,[14] we then epitaxially overgrew the seed crystals by gas diffusion of $NH_4(CO_3)_2$ leading to an ~20 μm thick overgrowth of Mg-containing calcite (Figure 3.1c). After 10 days of overgrowth, the crystals were rinsed and dried, and cyanoacrylate resin was poured over the top to encapsulate the crystals. The seed crystals with Mg-containing calcite overgrowth were then polished to expose the {001} face for measurement (Figure 3.1d and Figure 3.2).

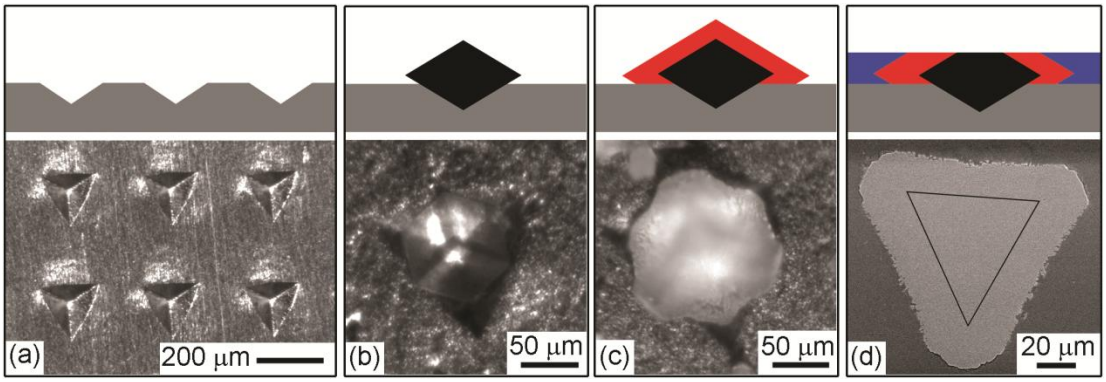

Figure 3.1 Profile (schematic) and top (a-c: light and, d: electron microscope images) views of experimental setup. (a) Array of impressions in Al substrate made to hold seed crystals with their c axis perpendicular to the substrate. (b) Seed crystal in impression. (c) Seed crystal with Mg-containing calcite overgrowth. (d) Secondary electron (SE) image of polished cross-section of crystal embedded within cyanoacrylate resin with black line overlay showing outline of seed crystal. Key: Gray: Al substrate; Black: calcite seed crystal; Red: Mg-containing calcite overgrowth; Blue: cyanoacrylate embedding resin.

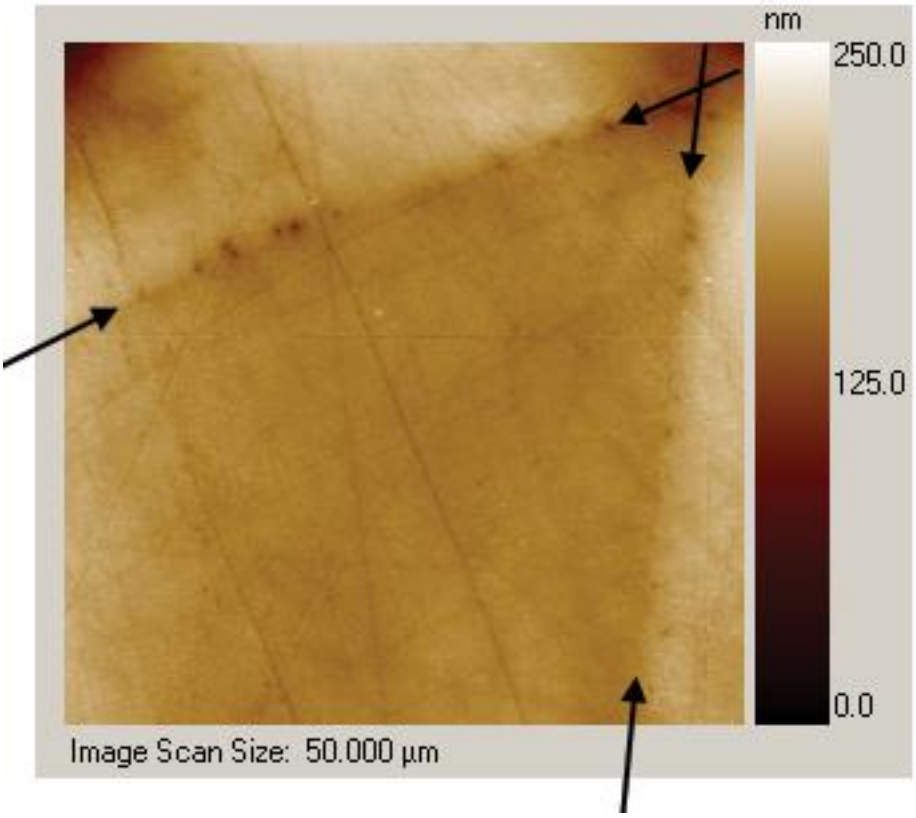

Figure 3.2 Surface topography of seed calcite crystal and magnesium-containing overgrowth as scanned by nanoindenter tip prior to indentation. The arrows indicate the interface between seed crystal and overgrowth.

We then used wavelength dispersive spectroscopy (WDS) to measure the magnesium and calcium content in the overgrowth region for five different synthetic crystals (Figure 3.3a). The WDS data showed that the magnesium concentration was fairly uniform parallel to the growth front (Figure 3.4), and increased at a non-linear rate as a function of distance from the seed crystal-overgrowth interface (Figure 3.3c). We also measured the Mg-content in Iceland spar and *Atrina rigida* to be 0.225 ± 0.044 at% (n=32) and 0.80 ± 0.11 at% (n=48), respectively.

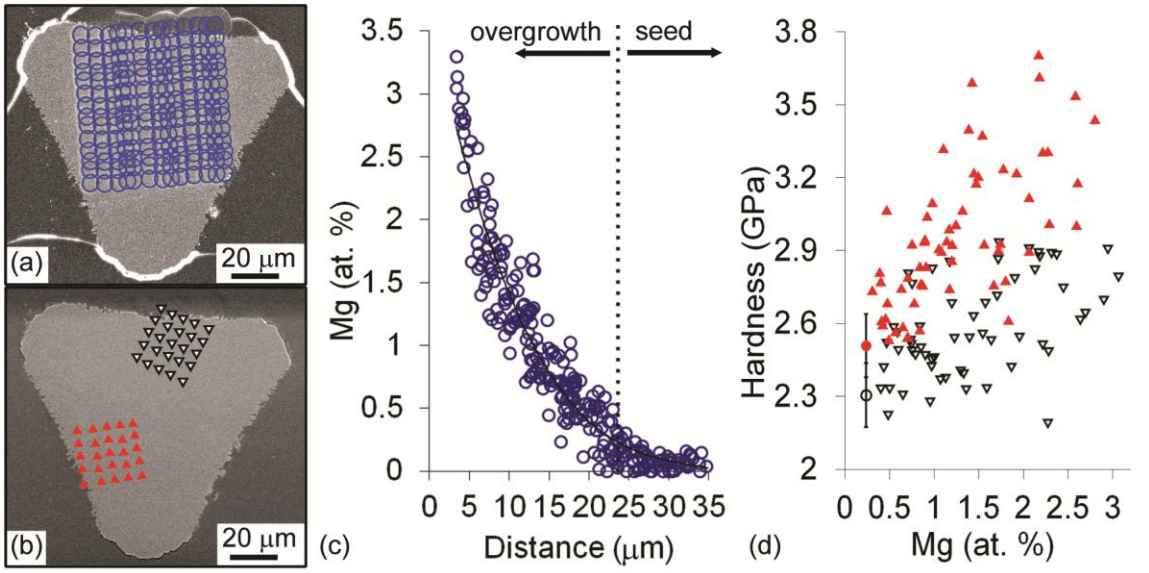

Figure 3.3 (a) SEM image with overlay of blue circles showing location of WDS magnesium and calcium measurements (5 µm spot size). (b) SEM image with triangle array overlay showing location of nanoindentation measurements for 0° (open black) and 60° (filled red) orientations for 1 of 5 crystals. (c) Mg-content as a function of distance from outer edge of crystals. Dotted line indicates approximate interface between seed-crystal and overgrowth region. For a diopside ($MgCaSi_2O_6$) standard, the Mg-content was 11.0 at% and the standard deviation as measured by counts per second was ± 1.7 at%. (d) Hardness as a function of Mg-content in overgrowth region. Triangles represent 0° (open black) and 60° (filled red) azimuthal angles while correspondingly colored circles represent the reference geologic values. For a standard fused silica sample, the hardness was 9.10 ± 0.15 GPa (n=4). Plots in (c) and (d) are compilations of data from 5 different crystals.

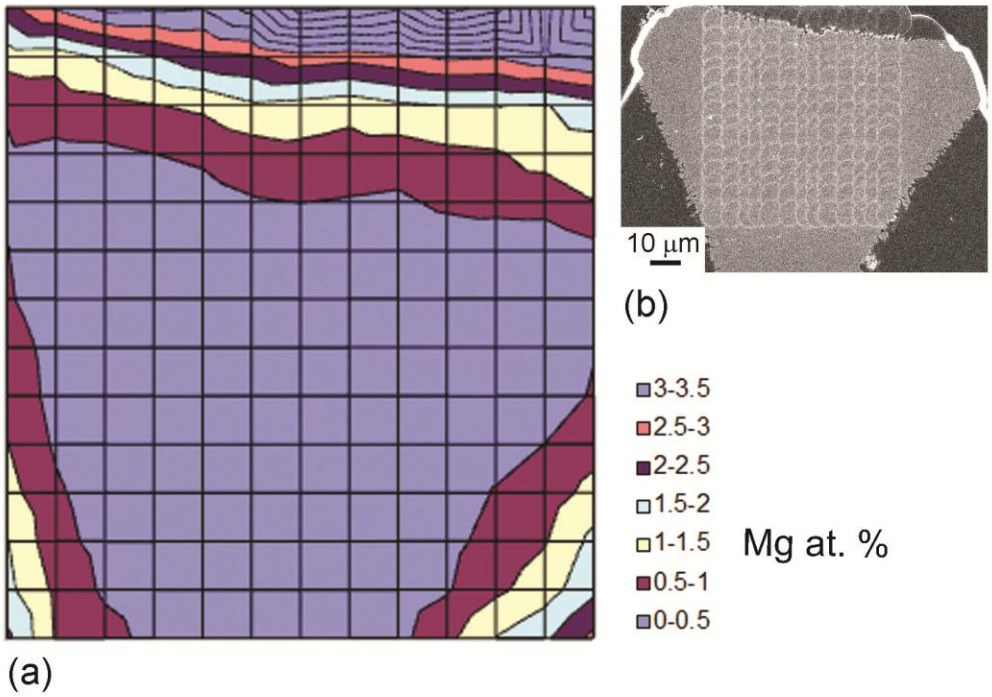

Figure 3.4 (a) Graphical representation of WDS magnesium data, with each square representing a 5 μm spot. The Mg-free seed crystal (light purple) is clearly seen in the center, surrounded by growth-bands of equal Mg-content. (b) SEM image taken with in-lens detector showing location of WDS measurements.

We used nanoindentation to measure the hardness and plane strain indentation modulus[15] of the polished faces at two different azimuthal angles in the same five crystals (Figure 3.3b). The resulting indentations were ~200 nm deep. Surface topography scans were performed with the indenter tip before and after indenting. These scans are sensitive enough to detect differences in polishing between the seed crystal and the overgrowth region (Figure 3.2). To avoid any influence from the seed crystal or the sample edges, we included only indentations that were more than 2 μm away from these interfaces.

Hardness as a function of magnesium concentration was determined by using the

distance from the overgrowth surface as a common parameter (Figure 3.3d). Hardness increases with increasing Mg content. Both 0° and 60° azimuthal orientations approach the values of geologic calcite with decreasing magnesium content, confirming the accuracy of this method. The indentation modulus of the overgrowth regions was similar to geologic calcite and consistent with DFT calculations[16] for small changes in composition (Figure 3.5).

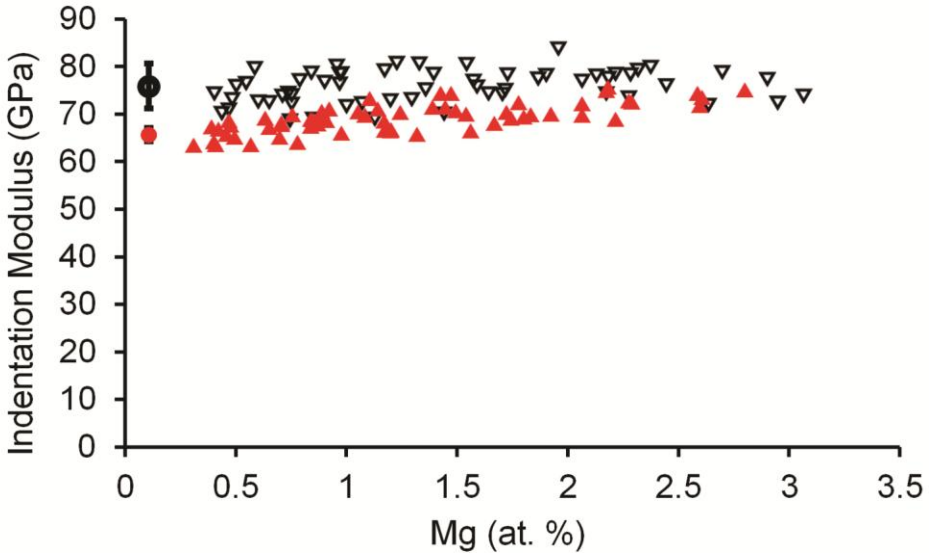

Figure 3.5 Plane strain indentation modulus,[4, 17] as a function of Mg-content in overgrowth region. Triangles represent 0° (open black) and 60° (filled red) azimuthal angles while correspondingly colored circles represent the reference geologic values. For a standard fused silica sample, the plane strain indentation modulus was 74.95 ± 1.25 GPa (n=4).

We assume the mechanism by which magnesium hardens calcite is solid solution hardening. X-ray diffraction,[18] computational studies,[16, 19] experimental phase diagrams,[11] TEM,[20, 21] AFM,[22] and cathodoluminescence[23] all show that magnesium is incorporated substitutionally into the calcite lattice at low concentrations, ≤1 at%. Since magnesium is

a smaller cation than calcium, it is expected to create lattice distortions (a stress field)[16, 19] that would hinder dislocation motion and increase the hardness. Theories for substitutional impurity strengthening suggest that the yield strength of single crystal metals follows a square root dependence[24] and it has been proposed that a similar relationship holds for ionic single crystals.[25] Therefore, we might expect a similar functional form for our hardness. We fit both linear and square root dependences to our data, but there was no difference in the quality of fit. In an attempt to extend our data set, we tried using a higher magnesium to calcium ratio (5 mM:5 mM) for the overgrowth solution.[26, 27] However, the overgrowth, while epitaxial, was no longer smooth and well-defined, leading to difficulties in correlating hardness with magnesium content. Thus, our experiments were constrained to equilibrium magnesium contents of <1 at%.

Given the relationship shown in Figure 3.3d, it is possible to evaluate the effect of magnesium in previous reports of the increased hardness of biogenic calcite. To a first order approximation, we have assumed that the effect of magnesium on the hardness of calcite may be separated out from the contributions due to other impurities (e.g., biomacromolecules and microstructural features found in biogenic calcite. For calcite crystals (with 0.8 at% Mg) from the mollusk, *Atrina rigida*, we reported a hardness between 3.5 and 4.2 GPa for the {001} plane depending on azimuthal angle.[4] From Figure 3.3d, a 0.84 at% Mg-containing calcite crystal has a hardness of 2.4 to 2.9 GPa. Therefore, assuming strengthening mechanisms in biogenic calcite are independent of each other, approximately 20% of the increased hardness found in calcite prisms from *Atrina rigida* could come from magnesium content. In another organism, the brachiopod *Megerlia truncata,* the magnesium content of the primary and secondary layer has been

reported to range from 0.2 to 0.9%[8] and therefore all of the increased hardness of the dorsal valve, which has been measured at 2.85 ± 0.41 GPa, could come from magnesium solid solution hardening.[10]

Other species produce supersaturated solid-solution Mg-containing calcites (>1 at%). For example, the spines from the sea urchin *Paracentrotus lividus* are comprised of calcite containing 3 to 5% magnesium in solid solution and the nanoindentation hardness on the {001} plane in the septa has been found to range from 3.6 to 4.1 GPa.[5] If we extrapolate from our data to the magnesium concentrations found in the sea urchin septa, it is possible that magnesium impurities could account for the increased hardness.

3.4 Conclusions

In summary, we have quantitatively determined the effect of magnesium incorporation on the hardness of calcite. Our results show that magnesium incorporation plays a significant role in hardening calcite, even at relatively low magnesium concentrations (in the equilibrium solid solubility regime < 1 at%). The results are consistent with a solid solution strengthening mechanism. A significant fraction of the hardness of several biogenic calcites, compared with a nearly pure geologic reference, can be attributed to magnesium impurities. To elucidate other hardening mechanisms in biogenic calcites, a similar approach, in which synthetic samples with well-controlled composition and microstructure are prepared and tested (e.g., calcite with incorporated organic macromolecules), can be used.

3.5 Materials and Methods

Geologic calcite specimen preparation: An optically clear geologic calcite rhombohedron (1-2 cm in length) was polished to expose the (001) plane (Iceland spar,

Carolina Biological Supplies GEO3429B). The sample was first manually polished by hand on a 30 μm aluminum oxide lapping film until ~1 cm^2 of both the (001) and (00-1) planes were exposed. Rough adjustments to the crystallographic orientation were made by polishing both {001} faces of the crystal until the vertex of each corner of the exposed surfaces were within a few degrees of an equilateral triangle as measured on a rotating microscope stage. Fine adjustments were then made by using a conoscope and centering the interference pattern or isogyre. The interference pattern was viewed with a Leica DM EP polarizing microscope set up as a conoscope by removing the eyepiece (Figure 3.6). We were able to orient the *c* axis to within ~1° of the surface normal using this technique. The crystal was then fixed with a cyanoacrylate resin (instant Krazy Glue, Elmers) to a glass microscope slide and the exposed (001) face was polished with a graded set of aluminum oxide lapping films followed by a final polish with a 50 nm Al_2O_3 powder (Buehler micropolish γ–Al_2O_3) suspended in a water and 2-methyl-2,4-pentanediol mix (Green Lube, Allied High Tech).[4]

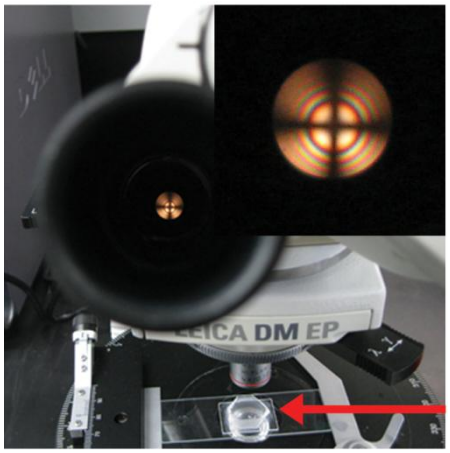

Figure 3.6 Experimental setup used during polishing to orient a geologic calcite crystal. Interference pattern (inset) is centered when the optical axis (*c* axis) is vertical. The field

of view is ~8°. The red arrow points to the geologic crystal , visible at the bottom of the image beneath the microscope objective.

Magnesium-containing calcite specimen preparation: A gradient of magnesium content in calcite was epitaxially overgrown on seed crystals, which were oriented by gravity to rest in aluminum impressions such that the *c* axis of the crystals was normal to the surface.

Substrate preparation: An array of impressions ~60 μm deep were made in 1/16 inch thick marine corrosion resistant aluminum 5052 (Speedy Metals) by using a home-built indenter that mimicked the morphology of the calcite rhombohedron. The home-built cubic zirconia indenter was polished using an Imahashi crystal polisher (Faceting Unit Model FAC-8) to orient the cubic zirconia at the desired angles and polished with a graded set of aluminum oxide lapping films. The crystal polisher is accurate to within 1° and it is estimated from light microscopy that the radius of curvature of the tip of the cubic zirconia was ~3 μm (Figure 3.7). The polished crystal was then attached perpendicularly to the knife mount of a Sorvall MT 2B ultramicrotome and the manual stepper of the microtome was used to press the cubic zirconia indenter into the aluminum substrate. A 4 by 11 array of impressions with 300 μm spacing was made, using the microtome's stage micrometers to reposition the indenter between impressions.

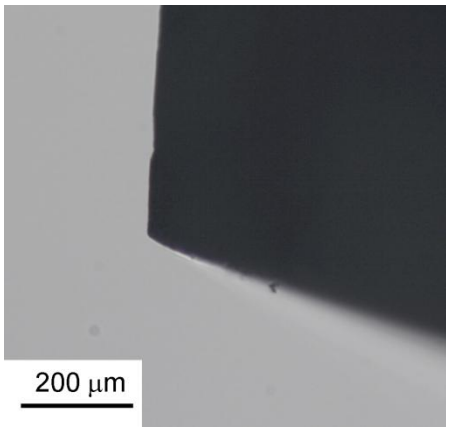

Figure 3.7 Optical microscope image of home-built cubic zirconia indenter, polished to be geometrically similar to a calcite rhombohedron. The indenter is used to make oriented impressions in aluminum that then hold the seed crystals.

Seed crystal growth: The seed crystals were grown in agarose gels according to our previously published procedure.[13] Briefly, CO_2 gas (from the sublimation of ammonium carbonate) was diffused into a hydrogel containing 1 w/v % agarose (Type IB; Sigma) and 5 mM $CaCl_2$. After overnight growth, the crystals were extracted by melting the hydrogel in boiling water until the crystals settled to the bottom of the container. The supernatant was then decanted and the crystals rinsed once with water and once with ethanol. This growth method creates relatively large (~75 μm on edge) and uniform seed crystals that are large enough to be manipulated under a dissecting microscope.

Mg-containing calcite overgrowth: The aluminum specimen holder was placed in a 15 mm petri dish with 3 mL of a solution of 1 mM $MgCl_2$ ($MgCl_2$•$6H_2O$; Sigma Aldrich 99%) and 5 mM $CaCl_2$ ($CaCl_2$•H_2O; Strem Chemicals 99.999%). Approximately 50 to 100 seed crystals were placed on top of the aluminum specimen holder. The crystals

were then manually pushed into the impressions using a glass fiber ~50 μm in diameter that was drawn by hand from a pipette. Gravity aligns the crystals in the impressions once they are close to the right orientation. Using the ammonium carbonate diffusion method, the seed crystals were then overgrown for 10 days to ensure adequate overgrowth and sufficient binding to the substrate. After overgrowth, the crystals were gently rinsed with DI water followed by ethanol to ensure their binding to the substrate and to clean the surface. Cyanoacrylate resin (instant Krazy Glue, Elmers) was then poured over the top of the array to embed the crystals. We then polished through the resin to expose the seed crystals and magnesium-containing calcite overgrowth using a graded set of aluminum oxide lapping films ending with a 50 nm Al_2O_3 powder (Buehler micropolish γ–Al_2O_3) suspended in a water and 2-methyl-2,4-pentanediol mix (Green Lube, Allied High Tech).[4] Surface roughness as measured by the nanoindenter surface scan was less than 10 nm RMS (Figure 3.2).

Nanoindentation: Load-displacement measurements were performed using a commercial nanoindenter system (Hysitron Triboindenter, Minneapolis, MN) in quasistatic mode. Prior to data collection, the tip shape of a Berkovich diamond indenter with a tip radius of ~120 nm was calibrated using the procedure of Oliver and Pharr.[15] Each indent consisted of five second load, hold and unload segments with the unloading segment used to calculate the plane strain indentation modulus and hardness via the method of Oliver and Pharr.[28] A 5 by 5 array of indents with 10 μm spacing was made in the overgrowth region of each crystal at 0° and 60° azimuthal angles (where we define the azimuthal angle to be 0° when the faces of the Berkovich tip, the {001} surface, and the adjacent {104} facets share common zone axes).[4] A total of 5 crystals were

examined.

Wavelength Dispersive Spectroscopy (WDS): WDS measurements were done after nanoindentation to ensure any surface damage induced by WDS was not reflected in the hardness measurements. WDS measurements were done using a JEOL 8900 microprobe with a 5 μm spot size, 6.5 nA current, 10 kV accelerating voltage, and 30 second acquisition time. The samples were coated in a thermal evaporator with ~25 nm of amorphous carbon to reduce charging. Magnesium and calcium content were calibrated against diopside ($MgCaSi_2O_8$) and calcite standards, respectively. An ~10 by 15 array of measurements with ~5 μm spacing was used for each crystal. WDS data were collected from the same 5 crystals that were used to determine hardness. For *Atrina rigida* (Gulf Specimen Marine Lab, Florida) and the geologic sample (Iceland spar), magnesium content was determined at 48 points in 43 prisms and at 32 points in one geologic single crystal, respectively.

Scanning Electron Microscopy (SEM): A scanning electron microscope (LEO 1550 FESEM) was used to characterize the location of the indentation and WDS measurements. Using the secondary electron detector, it was possible to see the location of the indents. Using the in-lens detector, which captures both backscattered and secondary electrons, we were able to see the location of the WDS imprints (Figure 3.4b).

Correlation of WDS and nanoindentation measurements: We then pieced together higher magnification images and measured the distance between the edge of the crystal and the center of the indents or WDS imprints from the images. We then fit a third order polynomial to the cumulative WDS data and used this polynomial to determine the magnesium content at the nanoindentation locations.

3.6 Acknowledgments

We acknowledge support from NSF (DMR 0845212), the J. D. Watson Investigator Program (NYSTAR Contract #C050017), the GI Bill (Chapter 33), and Hysitron Inc. We also acknowledge the Cornell Center for Materials Research (CCMR), a Materials Research Science and Engineering Center of the National Science Foundation (DMR 1120296), for both research support and use of the Electron Microscopy facility. We would also like to thank John Hunt for WDS measurements and Benjamin Shulman for help with sample preparation. Supporting Information is available online from MRS Communications or from the authors.

1. Meyers MA, Chen P-Y, Lin AY-M, Seki Y. Biological materials: structure and mechanical properties. *Prog Mater Sci* 2008, **53**(1)**:** 1-206.

2. Ma YR, Cohen SR, Addadi L, Weiner S. Sea urchin tooth design: an "all-calcite" polycrystalline reinforced fiber composite for grinding rocks. *Adv Mater* 2008, **20**(8)**:** 1555-1559.

3. Wang RZ, Addadi L, Weiner S. Design strategies of sea urchin teeth: structure, composition and micromechanical relations to function. *Phil Trans R Soc B* 1997, **352**(1352)**:** 469-480.

4. Kunitake ME, Mangano LM, Peloquin JM, Baker SP, Estroff LA. Evaluation of strengthening mechanisms in calcite single crystals from mollusk shells. *Acta Biomater* 2013, **9**(2)**:** 5353-5359.

5. Moureaux C, Pérez-Huerta A, Compère P, Zhu W, Leloup T, Cusack M*, et al.* Structure, composition and mechanical relations to function in sea urchin spine. *J Struct Biol* 2010, **170**(1)**:** 41-49.

6. Pérez-Huerta A, Cusack M, Zhu W. Assessment of crystallographic influence on material properties of calcite brachiopods. *Mineral Mag* 2008, **72**(2)**:** 563-568.

7. Pérez-Huerta A, Cusack M, Zhu W, England J, Hughes J. Material properties of brachiopod shell ultrastructure by nanoindentation. *J R Soc Interface* 2007, **4**(12)**:**

33-39.

8. Griesshaber E, Schmahl WW, Neuser R, Pettke T, Blum M, Mutterlose J*, et al.* Crystallographic texture and microstructure of terebratulide brachiopod shell calcite: An optimized materials design with hierarchical architecture. *Am Mineral* 2007, **92**(5-6)**:** 722-734.

9. Aizenberg J, Hendler G. Designing efficient microlens arrays: lessons from Nature. *J Mater Chem* 2004, **14**(14)**:** 2066-2072.

10. Merkel C, Deuschle J, Griesshaber E, Enders S, Steinhauser E, Hochleitner R*, et al.* Mechanical properties of modern calcite (*Mergerlia truncata*) and phosphate-shelled brachiopods (*Discradisca stella* and *Lingula anatina*) determined by nanoindentation. *J Struct Biol* 2009, **168**(3)**:** 396-408.

11. Anovitz LM, Essene EJ. Phase equilibria in the system $CaCO_3$-$MgCO_3$-$FeCO_3$. *J Petrol* 1987, **28**(2)**:** 389-415.

12. Raz S, Weiner S, Addadi L. Formation of high-magnesian calcites via an amorphous precursor phase: Possible biological implications. *Adv Mater* 2000, **12**(1)**:** 38-42.

13. Li HY, Estroff LA. Calcite growth in hydrogels: assessing the mechanism of polymer-network incorporation into single crystals. *Adv Mater* 2009, **21**(4)**:** 470-473.

14. Falini G, Gazzano M, Ripamonti A. Magnesium calcite crystallization from water-alcohol mixtures. *Chem Commun* 1996(9)**:** 1037-1038.

15. Oliver WC, Pharr GM. Measurement of hardness and elastic modulus by instrumented indentation: advances in understanding and refinements to methodology. *J Mater Res* 2004, **19**(1)**:** 3-20.

16. Elstnerova P, Friak M, Fabritius HO, Lymperakis L, Hickel T, Petrov M*, et al.* Ab initio study of thermodynamic, structural, and elastic properties of Mg-substituted crystalline calcite. *Acta Biomater* 2010, **6**(12)**:** 4506-4512.

17. Broz ME, Cook RF, Whitney DL. Microhardness, toughness, and modulus of Mohs scale minerals. *Am Mineral* 2006, **91**(1)**:** 135-142.

18. Pokroy B, Fitch AN, Marin F, Kapon M, Adir N, Zolotoyabko E. Anisotropic lattice distortions in biogenic calcite induced by intra-crystalline organic molecules. *J Struct Biol* 2006, **155**(1)**:** 96-103.

19. Stashans A, Chamba G. A new insight on the role of Mg in calcite. *Int J Quantum Chem* 2011, **111**(10)**:** 2436-2443.

20. Tsipursky SJ, Buseck PR. Structure of magnesian calcite from sea urchins. *Am Mineral* 1993, **78**(7-8)**:** 775-781.

21. Barber DJ, Reeder RJ, Smith DJ. A tem microstructural study of dolomite with curved faces (saddle dolomite). *Contributions to Mineralogy and Petrology* 1985, **91**(1)**:** 82-92.

22. Davis KJ, Dove PM, Wasylenki LE, De Yoreo JJ. Morphological consequences of differential Mg^{2+} incorporation at structurally distinct steps on calcite. *Am Mineral* 2004, **89**(5-6)**:** 714-720.

23. Paquette J, Reeder RJ. Relationship between surface structure, growth mechanism, and trace element incorporation in calcite. *Geochim Cosmochim Ac* 1995, **59**(4)**:** 735-749.

24. Courtney TH. *Mechanical behavior of materials*. McGraw-Hill, 1990.

25. Evans AG, Langdon TG. Structural ceramics. *Prog Mater Sci* 1976, **21**(3–4)**:** 171-285.

26. Long X, Nasse MJ, Ma Y, Qi L. From synthetic to biogenic Mg-containing calcites: a comparative study using FTIR microspectroscopy. *Physical Chemistry Chemical Physics* 2012, **14**(7)**:** 2255-2263.

27. Long X, Ma Y, Qi L. In vitro synthesis of high Mg calcite under ambient conditions and its implication for biomineralization process. *Cryst Growth Des* 2011, **11**(7)**:** 2866-2873.

28. Oliver WC, Pharr GM. An improved technique for determining hardness and elastic modulus using load and displacement sensing indentation experiments. *J Mater Res* 1992, **7**(6)**:** 1564-1583.

CHAPTER 4

4 THE EFFECTS OF AMINO ACID ADDITIVES ON THE HARDNESS OF SYNTHETIC CALCITE[d]

4.1 Introduction

We would like to understand why biogenic calcite is harder and tougher than geologic calcite[1-5] and to rationally design synthetic analogs. It is known that biogenic calcite often contains additives[6-14] and microstructural variations[15-21] not found in geologic calcite in the form of Iceland Spar, and these differences have been proposed as reasons for the increased hardness and toughness of biogenic calcite.[6-10, 22, 23] However, it is not known what role each of these individual additives and microstructural variations have in strengthening calcite nor whether some additives might be more effective than others at altering the mechanical properties of calcite. For example, calcite prisms from the mollusk Atrina *rigida* are harder than geologic calcite[6] and contain additives including Mg^{2+} ions, acidic proteins and polymer fibers;[12, 24, 25] what contribution do each of these additives provide to the increased hardness of biogenic calcite? In chapter 3, we examined the effect of Mg^{2+} substitution on the hardness and modulus of calcite. In chapter 5, we will look at the effect of nanometer sized polysaccharide fibers. In this chapter, we quantify the effect of small molecules on the hardness and modulus of calcite to enable a better understanding of how organic small molecule additives strengthen calcite and why biogenic materials are harder than their geologic counterparts.

[a]I would like to thank Dr. Yi-Yeoun Kim and Professor Fiona Meldrum, from Leeds University, England, for providing the calcite samples containing amino acid impurities. I would also like to thank Dr. Boaz Pokroy from Technion University, Israel, for x-ray data that quantified lattice strain within the samples, and Prof. Matthew Collins from York University, England, for high performance liquid chromatography data which quantified amino acid concentration within the calcite samples. I would like to thank all of them for their insightful discussions during the course of this work.

Small molecules also provide a means to examine the effects of additive size, structure, and chemistry on the mechanical properties of calcite. In ionic and metallic single crystals, the size-, charge-, and modulus mismatch between a substitutional impurity and lattice atoms affects the mechanical properties of the composite. Does the bond structure of a small molecule additive or the strength of interaction of an additive with the calcite lattice affect the hardness of single crystal biogenic and synthetic calcite? Small molecule additives, including amino acids, have stereospecific bonds and functional groups with different isoelectric points and have been shown to affect the nucleation rate-,[26] crystallographic orientation-,[27, 28] and morphology of calcite [28, 30-36, 38-46] grown from solution and to selectively nucleate polymorphs of calcium carbonate[26-37]. These changes are believed to be due to the interaction of small molecules with the growing crystallographic surface. The molecular crystal literature has many examples of molecular additives substitutionally replacing a host molecule[47, 48] in a molecular crystal; if small molecules are likewise substitutionally incorporated into the calcite lattice we would expect a correlation between hardness and additive size, structure or chemistry.

In this chapter, we examine the effect of the amino acids L-aspartic acid (Asp), glycine (Gly) and L-cysteine (Cys) (Figure 4.1) on the hardness and modulus of calcite. Amino acids have been extensively studied as growth modifiers for calcite, in particular because of their relationship to proteins.[30, 46, 49] In situ atomic force microscopy has been used to show that anionic amino acids could stereospecifically interact with hillocks on a growing calcite crystal surface, but evidence of incorporation was not found.[41, 42] It was suggested that the aspartic acid modifies the growth morphology by affecting the stability of the growing surface. More recently, high resolution x-ray diffraction data have shown

a normalized lattice strain that depends on the choice of amino acid impurity,[50] which suggests that amino acids are incorporated into the lattice substitutionally. An analogous hypothetical substitution for the case of an amino acid in calcite is shown in Figure 4.2.

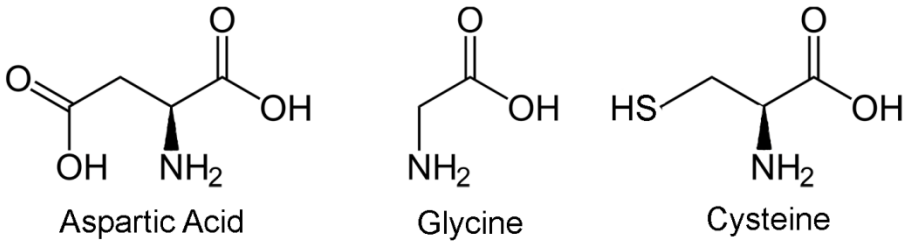

Figure 4.1 Chemical structures of three amino acids that were added to the calcite growth solution, and subsequently incorporated into the calcite crystals. Concentrations of amino acid in the growth solution ranged from 0.005 mM to 50 mM.

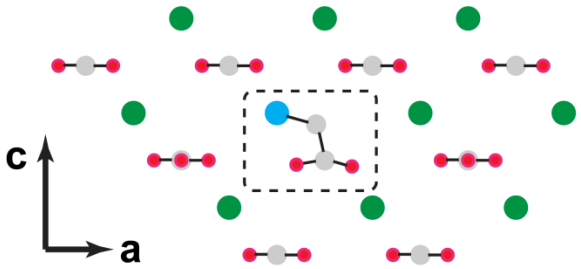

Figure 4.2 Hypothetical schematic of the substitutional mode of incorporation of an amino acid in the calcite lattice. The substitutional additive resides in registry with the calcite lattice, with the carboxylate group of the amino acid substitutionally replacing a CO_3^{2-} in calcite and the amino end replacing a calcium cation.

We use depth sensing nanoindentation to measure the effect of amino acid additives on mechanical properties. Since hardness is a measure of a material's resistance to permanent deformation, measurements can tell us about the strength of the interaction

of a dislocation with an impurity. Additives create barriers to dislocation motion, increasing hardness. In the case of atomic substitutions, this stress field can result from a size,[51-53] modulus,[51] or charge mismatch[52, 53] with a larger mismatch leading to a higher hardness. At the multiple unit cell length scale, a second phase impurity can also strengthen a material by a size or modulus mismatch with a coherent or incoherent particle. However, the energetics of the second phase itself must also be considered due to creation of internal defects and altered surface free energy if a dislocation passes through the second phase. Finally, second phase particles can also act as nucleation centers for dislocations, which can then interact with other dislocations on different slip planes, increasing the rate of work hardening.[54-57] We hope to examine whether a size or charge mismatch influences the hardness of calcite.

4.2 Experimental

Crystal Growth: Calcite single crystals containing a range of amino acid concentrations were grown by Dr. Yi Yeoun Kim at the University of Leeds, and sent to Cornell for hardness and modulus testing. Analytic grade (Sigma Aldrich) L-aspartic acid, glycine and L-cysteine (Figure 4.1), calcium chloride dihydrate and ammonium carbonate were used as starting materials without further purification.

To grow the single crystals, amino acids were mixed with calcium chloride dihydrate to prepare a 40 mL mixed solution containing 0.005 – 50 mM amino acid and 10 mM calcium. The mixed solution was then transferred to a 90 mm petri dish containing three Piranha-solution-cleaned glass slides and calcium carbonate precipitated by the ammonium carbonate diffusion method. All petri dishes were covered with

parafilm pierced with four holes and placed in a dessicator containing five grams of freshly crushed ammonium carbonate powder. Crystallization proceeded for two days, resulting in crystals that typically measured 20 to 60 μm on edge (Figure 4.3). The glass slides were then removed, rinsed with deionized water, rinsed with ethanol and finally air dried. All amino acid doped calcite samples had optically perfect rhombohedral morphology except for the Asp series grown in solutions greater than 5 mM Asp. Crystals grown at 5 mM Asp, exhibited slightly roughened {104} faces (Figure 4.3b inset) and crystals grown at 50 mM Asp were no longer rhombohedral (Figure 4.3c inset). Therefore, the maximum aspartic acid concentration tested by nanoindentation was 20 mM to avoid the possibility of accidentally indenting a spherical $CaCO_3$ polymorph instead of a polished calcite crystal with rounded edges.

Sample Preparation: Cyanoacrylate resin (Krazy Glue®) was poured over the top of the glass slides to encapsulate the randomly oriented crystals and then allowed to set overnight. The glue and crystals were polished by graded Al_2O_3 lapping films and a final 50 nm Al_2O_3 powder (Buehler micropolish γ–Al_2O_3) suspended in a water and 2-methyl-2,4-pentanediol mix (Green Lube, Allied High Tech). The glue and crystals were polished until the randomly oriented crystals were exposed for nanoindentation (Figure 4.4). The surface roughness following this protocol was less than 10 nm RMS.

Quantification of Amino Acid Content: Crystals from the same synthesis batches that were measured for hardness were also sent to York University, where the actual amino acid content incorporated within the synthetic calcite was measured using high performance liquid chromatograpy (HPLC).

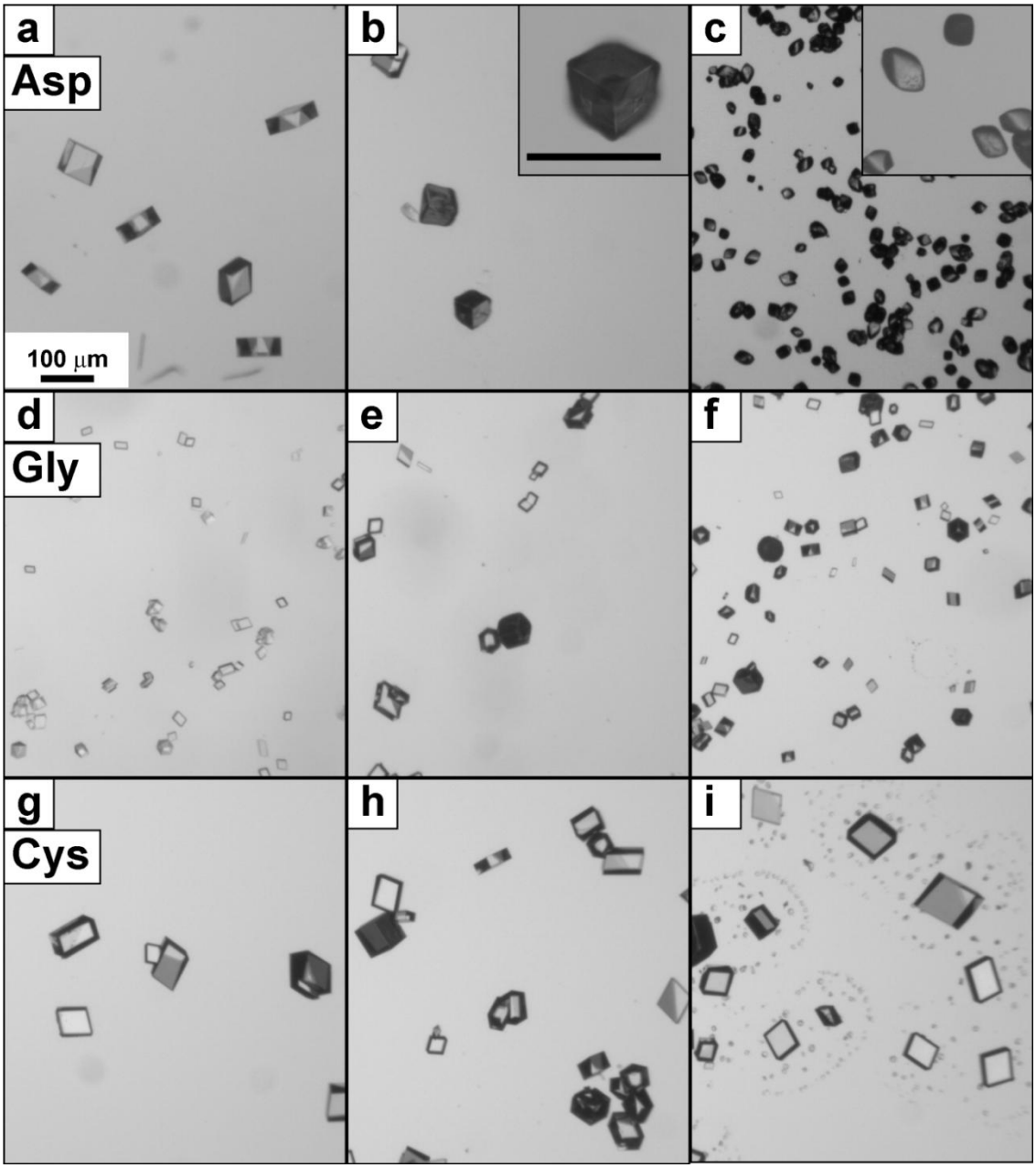

Figure 4.3 Optical micrographs of calcite crystals grown in 10 mM calcium solutions containing 1, 5 or 50 mM of amino acid (left to right). (a-c) Aspartic acid. (d-f) Glycine. (g-i) Cysteine. Inset in b shows roughening of {104} faces at 5 mM aspartic acid concentration and inset in c shows curved faces at 50 mM aspartic acid concentration. Scale bar in (a) is for all panels (a-i) and scale bar in the inset of (b) is also for inset in (c). Both scale bars are 100 μm.

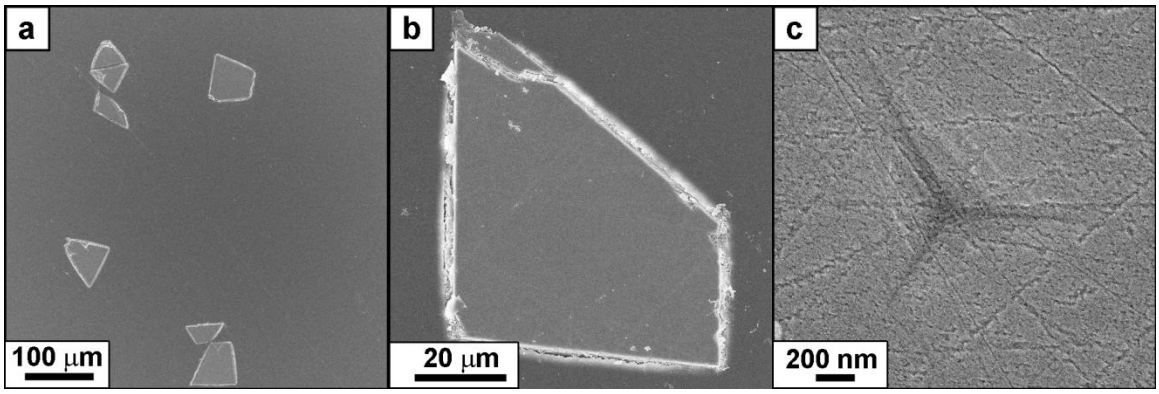

Figure 4.4 Scanning electron micrographs (a, b). Embedded calcite crystals grown in 1 mM aspartic acid and polished to expose crystal surfaces for nanoindentation. (c). Representative indent in calcite crystal with 2500 μN load. Surface roughnesses were less than 10 nm RMS as determined by nanoindenter surface scan.

Nanoindentation: Load-displacement measurements were performed using a Berkovich (~120 nm tip radius) diamond indenter on a commercial nanoindenter system (Hysitron Triboindenter) in quasistatic mode. Prior to data collection, the shape of the tip was calibrated using the method of Oliver and Pharr.[58] Each indent consisted of five second load, hold, and unload segments with a maximum 2500 μN load, resulting in ~200 nm deep indents, with the unloading segment used to calculate the indentation modulus and hardness.[58] The maximum load was chosen to create an indentation which was large enough to sample a homogeneous volume and minimize the effects of surface roughness, while allowing multiple indents per sample. Surface topography scans were performed with the indenter tip before and after indenting to ensure indentations were located at least 5 μm away from any edges. Each single crystal was measured in four to ten locations depending on size constraints, and five to eight different crystals were

measured for each amino acid concentration. This sampling density led to a minimum of 28 indents per amino acid concentration.

The hardness and modulus of calcite is dependent on crystallographic orientation and therefore, as discussed in Chapter 2, it is important to control for this variable when possible.[6, 59, 60] However, the as-grown synthetic crystals, for all amino acids tested, show a range of crystallographic growth orientations (Figure 3). Therefore, when the crystals were embedded in cyanoacrylate glue and polished to expose an indentation surface, we did not control for the orientation of the exposed indentation plane nor for the azimuthal angle of the indenter tip relative to the crystal. The data presented thus include variations in both hardness and modulus due to variations in crystallographic orientation.

4.3 Results

The hardness of calcite increases with the mole fraction of amino acid incorporated in the crystal (Figure 4.5) and also increases with the concentration of amino acids present in the growth solution (Figure 4.6). We present Figure 4.6 for completeness because only a subset of the samples that were tested for hardness were measured for amino acid content using HPLC. For all materials, the lowest hardnesses were found near the lowest impurity growth concentration and were similar to the values measured for geologic Iceland spar (2.3 to 2.5 GPa).[6] The highest hardnesses were found at the highest impurity growth concentrations and were similar to the values measured for calcite prisms from *Atrina rigida* (Chapter 2) (3.4 to 4.2 GPa).[6] Calcite crystals grown with aspartic acid had the largest hardness range from 2.3 to 4.1 GPa while those crystals grown with glycine and cysteine ranged from 2.4 to 3.4 GPa.

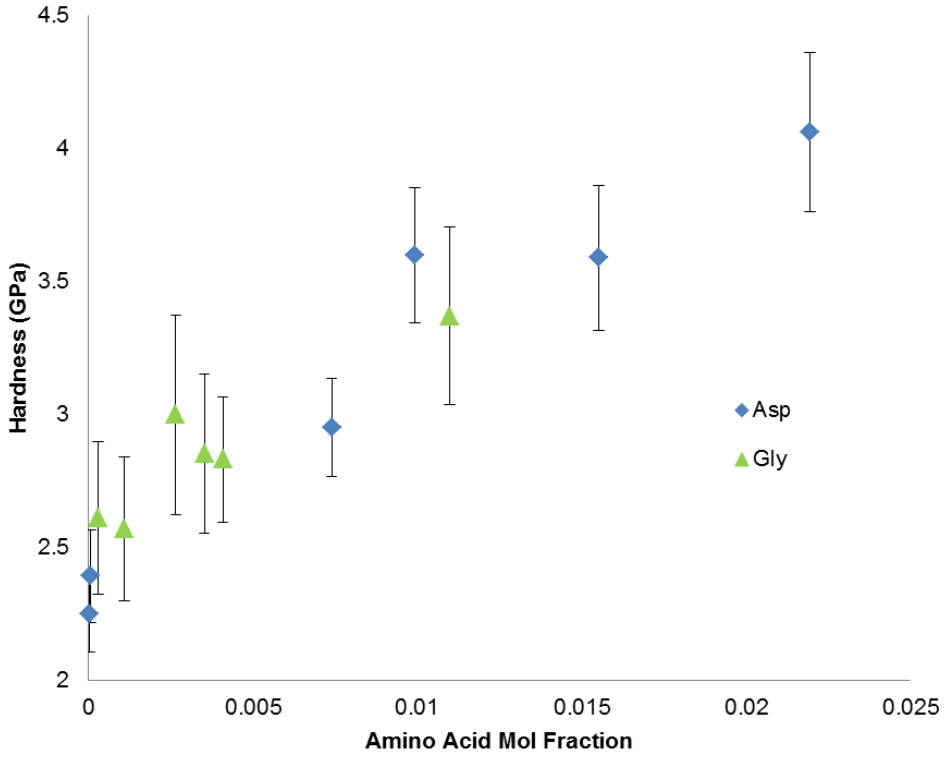

Figure 4.5 Graph of hardness versus amino acid mole fraction for aspartic acid (blue diamond) and glycine (green triangle). Molecular fraction measured by HPLC. Each data point represents the average of a minimum of 28 hardness measurements on at least five randomly oriented crystals.

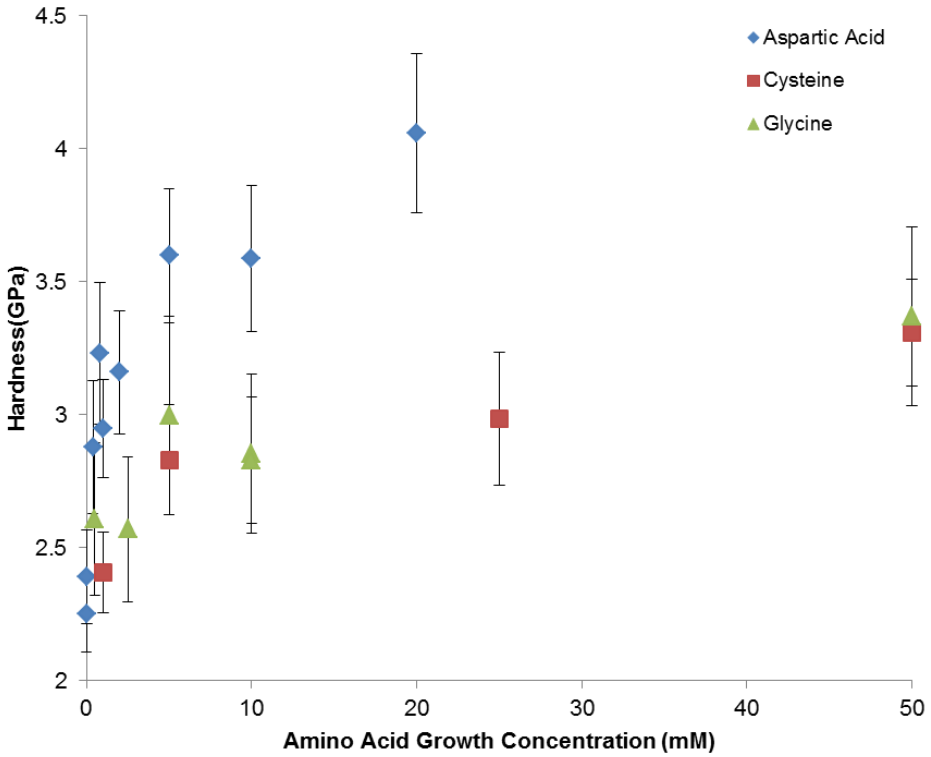

Figure 4.6 Graph of hardness versus concentration of amino acid in the growth solution for aspartic acid (blue diamond), glycine (green triangle) and cysteine (red square). Each data point represents the average of a minimum of 28, 39 and 42 hardness measurements on at least five randomly oriented crystals for Asp, Gly and Cys. Error bars represent one standard deviation.

In contrast to the hardness, the indentation modulus values (Figure 4.7), were similar for all amino acids tested and for all concentrations tested. Please see Chapter 1 for more discussion about the indentation modulus. The modulus values were up to 30% lower than the values measured for the average of the {001} and {104} faces of pure, geologic Iceland spar. Some of the lower modulus values may be due to additional compliance when measuring the smaller synthetic crystals. The synthetic crystals may not

have been firmly adhered to the glass substrate or the nucleating face may not have been smooth. Additional compliance during measurement is expected to affect modulus more than hardness and is consistent with the fact that the hardness at low concentrations for each additive sample was close to the pure geologic reference. We attribute the greater variation in the modulus of synthetic samples to the anisotropy of calcite as each amino acid data point is an average of at least five crystallographic orientations while the standard deviation of geologic calcite contains only data from when each face is taken individually. The average modulus for all samples from each amino acid set was comparable (Figure 4.7).

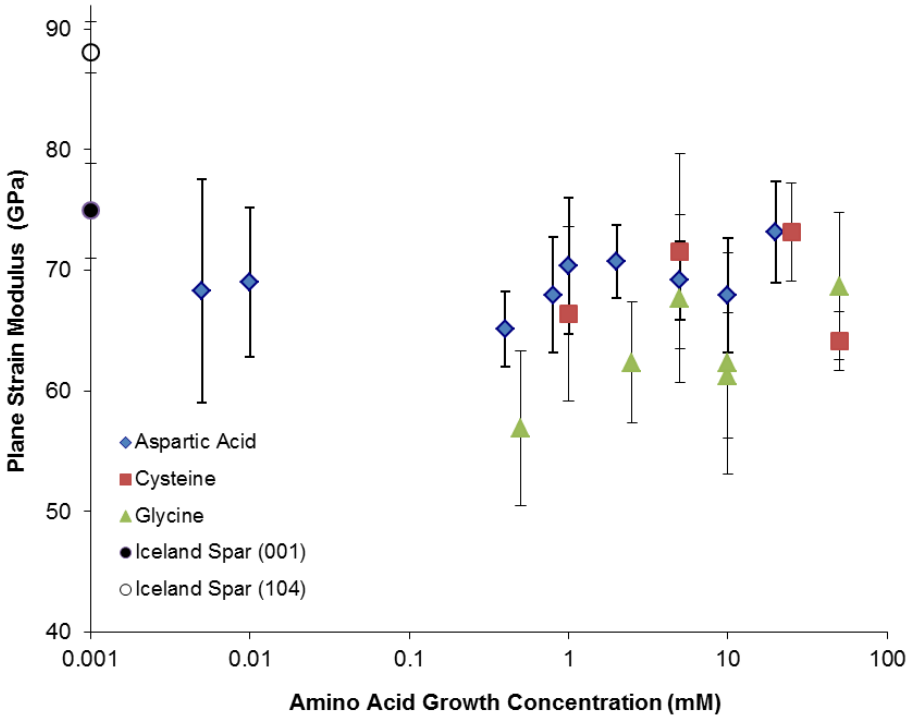

Figure 4.7 Graph of plane strain indentation modulus vs. concentration of the amino acid in the growth solution for aspartic acid (blue diamond), glycine (green triangle), cysteine (red square) and geologic Iceland spar (black circle).

Crystals were also sent for x-ray diffraction measurements at the European Synchrotron Radiation Facility (ESRF), where the lattice strain (Δc/c) associated with the additives was quantified. All three amino acids seem to fit on a master curve of hardness versus *c*-axis lattice strain. The hardening effect is non-linear and appears to be independent of the choice of amino acid (Figure 4.8).

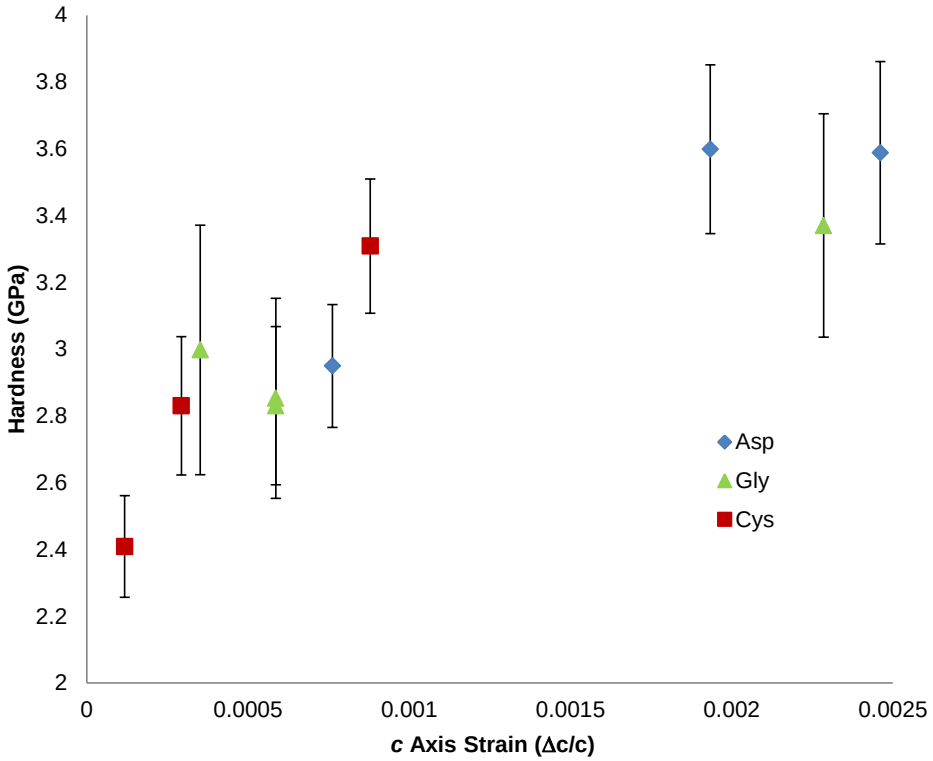

Figure 4.8 Graph of hardness versus *c* axis strain for aspartic acid (blue diamond), glycine (green triangle), and cysteine (red square). Each data point represents the average of a minimum of 28 hardness measurements on at least five randomly oriented crystals.

Although the hardness is correlated with *c*-axis strain, a homogenous or global shift in lattice parameter, such as that measured by a peak shift in x-ray diffraction, should not directly affect hardness. However, additive concentration affects hardness, and the global lattice strain is related to additive concentration. Thus the relationship shown

in Figure 4.8 may show a correlation between hardness and *c*-axis lattice strain. Although it is well known that the magnitude of the *local* strain created by an impurity is related to its stress field and hardening ability,[61] there is no reason to believe that the local strain fields around the molecules should change to increase the hardness.

4.4 Discussion

The increased hardness of biogenic calcite single crystals when compared with Iceland spar has been attributed to differences in magnesium[6-10] and organic macromolecule content,[6, 9, 22, 23] as well as microstructural features including crystallographic texture,[6, 22] crystallite size,[62] and inorganic to organic ratio.[7] This work shows that by only using small molecule amino acid additives, it is possible to synthetically increase the hardness of calcite to levels found in some biogenic calcites.[6, 62]

While additive size may play a role in the rate of hardening calcite, it is not the only factor. Comparing the effectiveness of amino acids with magnesium substitutionals (data adapted from chapter 3), amino acids are 3 to 5 times more effective at hardening calcite for a given mole fraction when compared to the magnesium substitutional additives (Figure 4.9). However, Figure 4.9 also shows that between amino acids, the larger aspartic acid has an equivalent hardening rate to the smaller glycine.

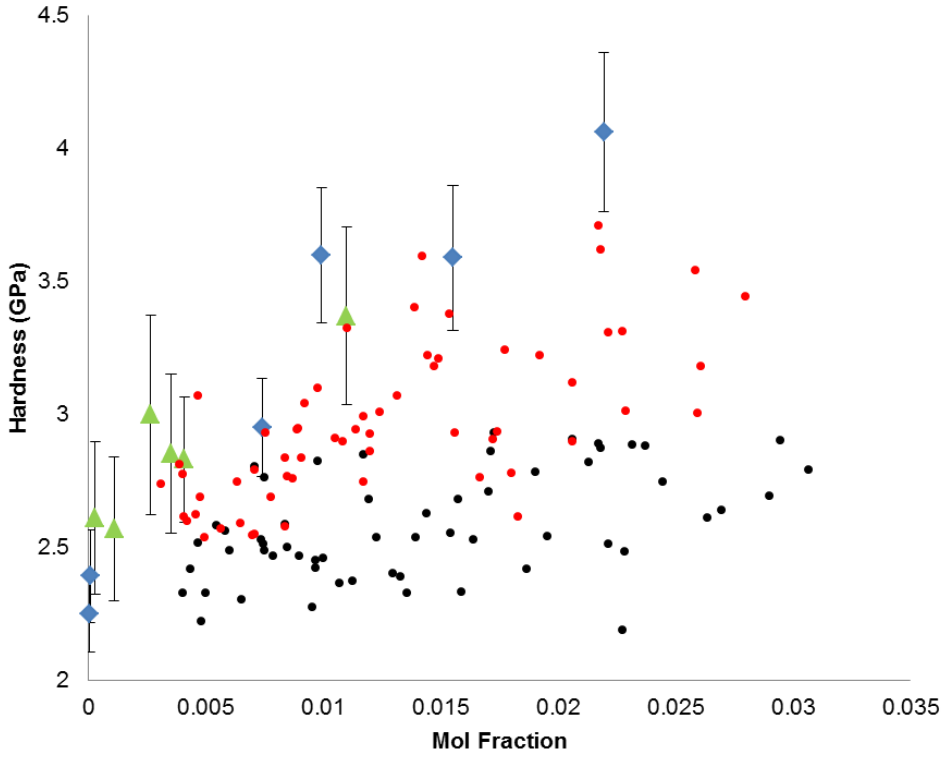

Figure 4.9 Graph of hardness versus additive mole fraction for aspartic acid (blue diamond), glycine (green triangle), and magnesium (circle). The magnesium data is from Chapter 3. Each data point for the amino acids represents the average of a minimum of 28 hardness measurements on at least five randomly oriented crystals while the magnesium data is as collected. Amino acid content was measured by HPLC while magnesium content was measured by WDS.

The net ionic charge associated with the amino acid additive might also be expected to create different stress fields within the calcite lattice and result in different hardening rates for the three amino acids. However, Figure 4.5 demonstrates that both glycine and aspartic acid have similar effects on hardness with additive content. The isoelectric points of aspartic acid (pI = 2.94), cysteine (pI = 5.01), and glycine (pI = 6.07),[63] suggest that although the partitioning of charge between crystal and additive is

undetermined, aspartic acid within the crystal would be expected to have a greater negative charge than cysteine or glycine. Therefore, the three amino acids might be expected to have different net valences within the crystal, and different hardening rates, possibly similar to the difference in rates between divalent and monovalent substitutions found in NaCl.[64-66] It is therefore surprising that glycine and aspartic acid have similar effects on hardness with additive content.

Given the relationship shown in Figure 4.5, it is tempting to try to quantify the hardening effect of aspartic and glycine rich proteins, as well as organic impurities found in previous reports of the increased hardness of *Atrina rigida*. In the case of *Atrina rigida*, previous reports showed the organic intra-crystalline content contained 0.28 wt% insoluble and 0.085 wt% soluble proteins,[12] and an undetermined amount of chitin. However, the seminal investigation of the prismatic layer of *Atrina rigida* did not consider the presence of small molecules in the intra-crystalline matrix, and used a 3500 MW dialysis cutoff to separate out organic additives.[12] Thus, attempting to quantify the effect of organic content using the relationship determined in Figure 4.9, would be speculative as the true organic intra-crystalline content is still unknown. However, TGA has shown a decomposition weight loss greater than 8% (Appendix Figure A2.1) suggesting that the intra-crystalline organic content may be significant.

4.5 Conclusions

The data presented in this chapter demonstrates that small molecule additives could be responsible for a large portion of the increased hardness of biogenic calcites. At their highest concentrations, small molecules can increase the hardness of synthetic

calcite to equal that of biogenic calcite from the mollusk Atrina *rigida*. The results emphasize the importance of small molecules in addition to substitutional impurities and large biomacromolecules, in determining the mechanical properties of inorganic single crystals.

Without further information about how the amino acid molecules are incorporated into the calcite lattice, it is impossible to attribute specific strengthening mechanisms to substitutional small molecule additives. For example, while the amino acids are more effective than the smaller magnesium ion at hardening calcite, glycine is just as effective as the larger aspartic acid. Without knowing if glycine replaces the same calcite atoms as an aspartic acid, it is not possible to know if a strengthening mechanism exists due to a size mismatch. Furthermore, glycine and aspartic acids have different isoelectric points yet similar strengthening rates. Without knowing if glycine and aspartic acid replace the same ionic charges within calcite, it is not possible to know if a strengthening mechanism exists due to a charge mismatch. More information is needed to determine the local strain surrounding these additives in order to be able to determine the strengthening mechanisms. Atomic probe microscopy, solid state NMR and near edge x-ray absorption fine spectra should be capable of distinguishing the chemistry of the amino acids and whether they are aggregated in the crystal, or reside within the crystalline lattice, helping to clarify the role of additive structure and chemistry on the hardness of calcite.

References

1. Weiner S, Addadi L, Wagner HD. Materials design in biology. *Mat Sci Eng C-Bio S* 2000, 11(1): 1-8.

2. Weiner S, Dove PM. An Overview of Biomineralization Processes and the

Problem of the Vital Effect. *Reviews in mineralogy and geochemistry* 2003, 54(1): 1-29.

3. Morse JW, Arvidson RS, Luttge A. Calcium carbonate formation and dissolution. *Chem Rev* 2007, 107(2): 342-381.

4. Ma YR, Cohen SR, Addadi L, Weiner S. Sea urchin tooth design: an "all-calcite" polycrystalline reinforced fiber composite for grinding rocks. *Adv Mater* 2008, 20(8): 1555-1559.

5. Westbroek P, Jong EWd, Wal Pvd, Borman AH, Vrind JPMd, Kok D*, et al.* Mechanism of Calcification in the Marine Alga Emiliania huxleyi [and Discussion]. *Philosophical Transactions of the Royal Society of London Series B, Biological Sciences* 1984, 304(1121): 435-444.

6. Kunitake ME, Mangano LM, Peloquin JM, Baker SP, Estroff LA. Evaluation of strengthening mechanisms in calcite single crystals from mollusk shells. *Acta Biomater* 2013, 9(2): 5353-5359.

7. Wang RZ, Addadi L, Weiner S. Design strategies of sea urchin teeth: structure, composition and micromechanical relations to function. *Phil Trans R Soc B* 1997, 352(1352): 469-480.

8. Moureaux C, Pérez-Huerta A, Compère P, Zhu W, Leloup T, Cusack M*, et al.* Structure, composition and mechanical relations to function in sea urchin spine. *J Struct Biol* 2010, 170(1): 41-49.

9. Pérez-Huerta A, Cusack M, Zhu W, England J, Hughes J. Material properties of brachiopod shell ultrastructure by nanoindentation. *J R Soc Interface* 2007, 4(12): 33-39.

10. Griesshaber E, Schmahl WW, Neuser R, Pettke T, Blum M, Mutterlose J*, et al.* Crystallographic texture and microstructure of terebratulide brachiopod shell calcite: An optimized materials design with hierarchical architecture. *Am Mineral* 2007, 92(5-6): 722-734.

11. Berman A, Addadi L, Weiner S. Interactions of sea urchin skeleton macromolecules with growing calcite crystals- a study of intracrystalline proteins. *Nature* 1988, 331(6156): 546-548.

12. Nudelman F, Chen HH, Goldberg HA, Weiner S, Addadi L. Spiers memorial lecture: lessons from biomineralization: comparing the growth strategies of mollusc shell prismatic and nacreous layers in *Atrina rigida*. *Faraday Discuss* 2007, 136: 9-25.

13. Pokroy B, Fitch AN, Marin F, Kapon M, Adir N, Zolotoyabko E. Anisotropic lattice distortions in biogenic calcite induced by intra-crystalline organic molecules. *J Struct Biol* 2006, 155(1): 96-103.

14. Kunitake ME, Baker SP, Estroff LA. The effect of magnesium substitution on the hardness of synthetic and biogenic calcite. *MRS Communications* 2012, 2(03): 113-116.

15. Asenath-Smith E, Li H, Keene EC, Seh ZW, Estroff LA. Crystal Growth of Calcium Carbonate in Hydrogels as a Model of Biomineralization. *Adv Funct Mater* 2012, 22(14): 2891-2914.

16. Pokroy B, Fitch AN, Zolotoyabko E. The microstructure of biogenic calcite: A view by high-resolution synchrotron powder diffraction. *Adv Mater* 2006, 18(18): 2363-2368.

17. Berman A, Hanson J, Leiserowitz L, Koetzle TF, Weiner S, Addadi L. Biological control of crystal texture - a widespread strategy for adapting crystal properties to function. *Science* 1993, 259(5096): 776-779.

18. Aizenberg J, Hanson J, Koetzle TF, Weiner S, Addadi L. Control of macromolecule distribution within synthetic and biogenic single calcite crystals. *J Am Chem Soc* 1997, 119(5): 881-886.

19. Gilow C, Zolotoyabko E, Paris O, Fratzl P, Aichmayer B. Nanostructure of biogenic calcite crystals: a view by small-angle x-ray scattering. *Cryst Growth Des* 2011, 11(6): 2054-2058.

20. Okumura T, Suzuki M, Nagasawa H, Kogure T. Microstructural variation of biogenic calcite with intracrystalline organic macromolecules. *Cryst Growth Des* 2011, 12(1): 224-230.

21. Li H, Xin HL, Kunitake ME, Keene EC, Muller DA, Estroff LA. Calcite prisms from mollusk shells (*Atrina rigida*): swiss-cheese-like organic–inorganic single-

crystal composites. *Adv Funct Mater* 2011: 2028-2034.

22. Pérez-Huerta A, Cusack M, Zhu W. Assessment of crystallographic influence on material properties of calcite brachiopods. *Mineral Mag* 2008, 72(2): 563-568.

23. Aizenberg J, Hendler G. Designing efficient microlens arrays: lessons from Nature. *J Mater Chem* 2004, 14(14): 2066-2072.

24. Gotliv B-A, Kessler N, Sumerel JL, Morse DE, Tuross N, Addadi L*, et al.* Asprich: A Novel Aspartic Acid-Rich Protein Family from the Prismatic Shell Matrix of the Bivalve Atrina rigida. *ChemBioChem* 2005, 6(2): 304-314.

25. Nudelman F, Shimoni E, Klein E, Rousseau M, Bourrat X, Lopez E*, et al.* Forming nacreous layer of the shells of the bivalves Atrina rigida and Pinctada margaritifera: An environmental- and cryo-scanning electron microscopy study. *J Struct Biol* 2008, 162(2): 290-300.

26. Kitano Y, Hood DW. Influence of Organic Material on Polymorphic Crystallization of Calcium Carbonate. *Geochim Cosmochim Ac* 1965, 29(1): 29.

27. Borah BM, Dey SK, Das G. Crystal to Calcite: Fabrication of Pure Calcium Carbonate Polymorph in the Solid State. *Cryst Growth Des* 2011, 11(7): 2773-2779.

28. Mann S, Archibald DD, Didymus JM, Douglas T, Heywood BR, Meldrum FC*, et al.* Crystallization at Inorganic-Organic Interfaces - Biominerals and Biomimetic Synthesis. *Science* 1993, 261(5126): 1286-1292.

29. Maruyama K, Yoshino T, Kagi H. Synthesizing a composite material of amorphous calcium carbonate and aspartic acid. *Materials Letters* 2011, 65(2): 179-181.

30. Tong H, Ma W, Wang L, Wan P, Hu J, Cao L. Control over the crystal phase, shape, size and aggregation of calcium carbonate via a L-aspartic acid inducing process. *Biomaterials* 2004, 25(17): 3923-3929.

31. Sugihara H, Ono K-i, Adachi K, Setoguchi Y, Ishihara T, Takita Y. Systhesis of Disk-Like Calcium Carbonate (Part 1) Effect of Various Organic Compounds on the Carbonation of the Basic Calcium Carbonate. *Journal of the Ceramic Society*

of Japan 1996, 104(1213): 832-836.

32. Sugihara H, Anan T, Adachi K, Baba A, Egashira N, Nishiguchi H*, et al.* Synthesis of Disk-Like Calcium Carbonate (Part 2) Effect of Various Ethylenediamine Compounds on the Carbonation of Basic Calcium Carbonate and Mechanism of Disk-Like Calcium Carbonate Synthesis. *Journal of the Ceramic Society of Japan* 1997, 105(1226): 886-890.

33. Meldrum FC, Hyde ST. Morphological influence of magnesium and organic additives on the precipitation of calcite. *Journal of Crystal Growth* 2001, 231(4): 544-558.

34. Dickinson SR, McGrath KM. Switching between kinetic and thermodynamic control: calcium carbonate growth in the presence of a simple alcohol. *J Mater Chem* 2003, 13(4): 928-933.

35. Keum DK, Naka K, Chujo Y. Unique crystal morphology of hydrophobic CaCO3 composite by sodium trisilanolate in a mixture of a water-miscible organic solvent and water. *Journal of Crystal Growth* 2003, 259(4): 411-418.

36. Didymus JM, Oliver P, Mann S, Devries AL, Hauschka PV, Westbroek P. Influence of Low-Molecular-Weight and Macromolecular Organic Additives on the Morphology of Calcium-Carbonate. *J Chem Soc Faraday T* 1993, 89(15): 2891-2900.

37. Wolf SE, Loges N, Mathiasch B, Panthofer M, Mey I, Janshoff A*, et al.* Phase selection of calcium carbonate through the chirality of adsorbed amino acids. *Angewandte Chemie* 2007, 46(29): 5618-5623.

38. Borah BM, Bhuyan BJ, Das G. Low-molecular-weight poly-carboxylate as crystal growth modifier in biomineralization. *Journal of Chemical Sciences* 2006, 118(6): 519-524.

39. Babu Mukkamala S, Powell AK. Biomimetic assembly of calcite microtrumpets: crystal tectonics in action. *Chemical Commununications* 2004(8): 918-919.

40. Estroff LA, Addadi L, Weiner S, Hamilton AD. An organic hydrogel as a matrix for the growth of calcite crystals. *Org Biomol Chem* 2004, 2(1): 137-141.

41. Orme CA, Noy A, Wierzbicki A, McBride MT, Grantham M, Teng HH*, et al.* Formation of chiral morphologies through selective binding of amino acids to calcite surface steps. *Nature* 2001, 411(6839): 775-779.

42. Teng HH, Dove PM, Orme CA, De Yoreo JJ. Thermodynamics of calcite growth: baseline for understanding biomineral formation. *Science* 1998, 282(5389): 724-727.

43. Mann S, Didymus JM, Sanderson NP, Heywood BR, Samper EJA. Morphological Influence of Functionalized and Non-Functionalized-Alpha,Omega-Dicarboxylates on Calcite Crystallization. *J Chem Soc Faraday T* 1990, 86(10): 1873-1880.

44. Wada N, Yamashita K, Umegaki T. Effects of Carboxylic Acids on Calcite Formation in the Presence of Mg2+Ions. *J Colloid Interface Sci* 1999, 212(2): 357-364.

45. Wada N, Kanamura K, Umegaki T. Effects of Carboxylic Acids on the Crystallization of Calcium Carbonate. *J Colloid Interface Sci* 2001, 233(1): 65-72.

46. Hazen RM, Filley TR, Goodfriend GA. Selective adsorption of l- and d-amino acids on calcite: Implications for biochemical homochirality. *Proc Natl Acad Sci* 2001, 98(10): 5487-5490.

47. Bullard T, Wustholz KL, Bott ED, Robertson M, Reid PJ, Kahr B. Role of Kinks in Dyeing Crystals: Confocal Luminescence Microscopy from Single Molecules to Square Centimeters. *Cryst Growth Des* 2008, 9(2): 982-990.

48. Weissbuch I, Addadi L, Leiserowitz L. Molecular recognition at crystal interfaces. *Science* 1991, 253(5020): 637-645.

49. Manoli F, Kanakis J, Malkaj P, Dalas E. The effect of amino acids on the crystal growth of calcium carbonate. *Journal of Crystal Growth* 2002, 236(1–3): 363-370.

50. Borukhin S, Bloch L, Radlauer T, Hill AH, Fitch AN, Pokroy B. Screening the Incorporation of Amino Acids into an Inorganic Crystalline Host: the Case of Calcite. *Adv Funct Mater* 2012, 22(20): 4216-4224.

51. Fleischer RL. Substitutional Solution Hardening. *Acta Metallurgica* 1963, 11(3): 203.

52. Luhman WJ, Gorum AE. The Effect of Impurities on the Strength of Silver Chloride. *Acta Metallurgica* 1959, 7(10): 685-687.

53. Gilman JJ. Theory of Solution Strengthening of Alkali-Halide Crystals. *J Appl Phys* 1974, 45(2): 508-509.

54. Evans RA, Wronski AS, Redfern BAW. Generation of Slip by Pressurization of LiF Single-Crystals Containing Cavities. *Philosophical Magazine* 1974, 29(6): 1381-1398.

55. Evans RA, Redfern BAW, Wronski AS. Influence of Hydrostatic Pressure on Microstructure of Lif Single-Crystals Containing Cavities. *J Mater Sci* 1972, 7(10): 1216.

56. Evans RA, Wronski AS, Redfern BAW. Influence of Pressurization-Induced Dislocations on Plastic-Deformation of Lif and Nacl Monocrystals. *J Mater Sci* 1975, 10(3): 427-435.

57. Redfern BAW, Evans RA, Wronski AS. Generation of Dislocations by Hydrostatic Pressure in Nacl Monocrystals Containing Na2so4 Particles. *J Mater Sci* 1970, 5(9): 784.

58. Oliver WC, Pharr GM. Measurement of hardness and elastic modulus by instrumented indentation: advances in understanding and refinements to methodology. *J Mater Res* 2004, 19(1): 3-20.

59. Carter GM, Henshall JL, Wakeman RJ. Knoop hardness and fracture anisotropy of calcite. *J Mater Sci Lett* 1993, 12(6): 407-410.

60. Winchell H. The Knoop microhardness tester as a mineralogical tool. *Am Mineral* 1945, 30(9-10): 583-595.

61. Rosenhain W. The Hardness of Solid Solutions. *Proceedings of the Royal Society of London Series A* 1921, 99(698): 196-202.

62. Merkel C, Deuschle J, Griesshaber E, Enders S, Steinhauser E, Hochleitner R*, et al.* Mechanical properties of modern calcite (*Mergerlia truncata*) and phosphate-shelled brachiopods (*Discradisca stella* and *Lingula anatina*) determined by nanoindentation. *J Struct Biol* 2009, 168(3): 396-408.

63. Bull HB, Breese K. Surface tension of amino acid solutions: A hydrophobicity scale of the amino acid residues. *Archives of Biochemistry and Biophysics* 1974, 161(2): 665-670.

64. Dryden JS, Morimoto S, Cook JS. The hardness of alkali halide crystals containing divalent ion impurities. *Philosophical Magazine* 1965, 12(116): 379-391.

65. Stokes RJ, Li CH. The sodium chloride-silver chloride alloy system. *Acta Metallurgica* 1962, 10(5): 535-542.

66. Courtney TH. *Mechanical behavior of materials*. McGraw-Hill, 1990.

CHAPTER 5

5 HARDNESS OF POLYMER REINFORCED CALCITE

5.1 Introduction

Organisms from mammals to mollusks produce a range of fiber-reinforced biomineral composites that have amazing functional utility.[1-4] For example, otoconia, or "ear dust", are micron-sized calcite crystals containing inter- and intra-otoconial filaments that transmit forces between otoconia and to our nervous system to regulate balance.[2, 5] The presence of occluded polymer fibers within the single-crystal matrix of octoconia and other biominerals may impart improved mechanical properties to the inherently brittle minerals.[1, 6-8] The effect of polymer reinforcement on the hardness and toughness of single-crystal biominerals, however, is not well understood because biogenic crystals contain additional inorganic and organic impurities and microstructural variations (see Chapters 2-4).[9-16] Therefore, to isolate the role of polymer fibers in determining the hardness of biominerals, we have developed a gel-growth system in which the amount of polysaccharide fibers occluded within calcite crystals can be controlled.[17, 18]

Previous work has demonstrated that calcite crystals grown in agarose hydrogels incorporate the gel fibers.[17, 18] The amount of gel fibers incorporated into the crystals can be controlled by varying the growth conditions. High resolution ADF-STEM shows that the agarose fibers are incorporated as a second phase with a continuous network structure within the calcite lattice.[18] At the internal interfaces, both low energy uncharged {104}

facets and high energy homocharged {012} facets are expressed. These interfaces are notable because the chemical interaction of agarose with calcite is presumed to be weak given the uncharged structure of agarose (Figure 5.1) and the fact that the externally expressed morphology consists of rhombohedral {104} facets.[18] This mode of incorporation is in contrast to inorganic additives like magnesium and strontium (see Chapter 3), which substitutionally replace calcium cations in the calcite lattice.[19] The physical interaction of agarose fibers with calcite and the associated network structure, may enable additional strengthening mechanisms for the calcite not possible with discrete inorganic or small molecule additives.[8, 20-22]

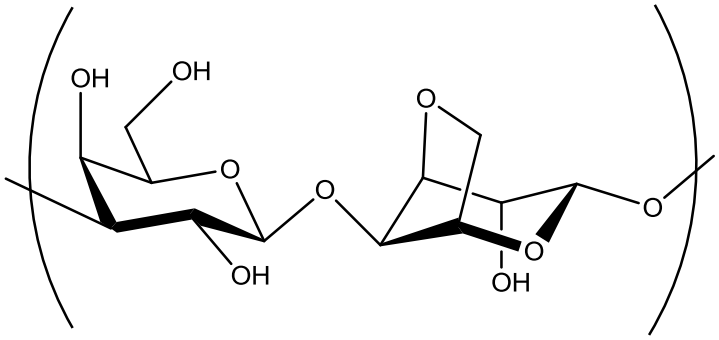

Figure 5.1 Chemical structure of repeating unit of agarose. The average agarose polymer contains ~300 repeats.

Agarose is a naturally occurring, neutral linear polysaccharide extracted from seaweed (algae). It has a molecular weight of ~120,000 g/mol and consists of alternating 1,3-linked β-D-galactopyranose and 1,4-linked 3,6-anhydro-α-L-galactopyranose (Figure 5.1).[23-26] When heated in water, agarose powder dissolves with the polymer chains forming random coils; upon cooling, these chains form water-stabilized double helices, which aggregate to form fibers of 10 to 10^4 helices.[25, 27, 28] The condensed fibers then

physically entangle to form a random network structure.[29] Water remains within the porous network structure, and the resulting homogenous (at the macroscopic scale) material is called a hydrogel.

The dimensions and spacing of agarose fibers in a hydrogel gives a measure of the defect density that might be found within a single crystal when these fibers are incorporated into the crystalline lattice. In the case of the hydrogel, average fiber diameters range from 2 to 30 nanometers[27-30] with larger fibers corresponding to higher concentrations. With increasing gel concentration, average pore diameters of the gaps within the network structure decrease from 2000 nm to 55 nm[24, 27, 29-35] and the average distance between neighboring fibers decreases from 600 to 130 nm (Figure 5.2).[29] These two metrics of fiber spacing are slightly different because they originate from two different testing methods. Average pore diameter is obtained by measuring a diffusion rate though the gel and calculating an effective pore size (pore diameter) needed to restrict diffusion to the measured level. Interfiber distance is measured by microscope images by measuring the average distance between neighboring fibers.[e]

[e] One caveat to the assumption that fiber diameter increases with gel concentration is that Waki et al. state that the diameter and number of fiber shadows increases with gel concentration, yet publish a table showing that the fiber diameter decreases. It is uncertain whether the text or the table is correct.[27]

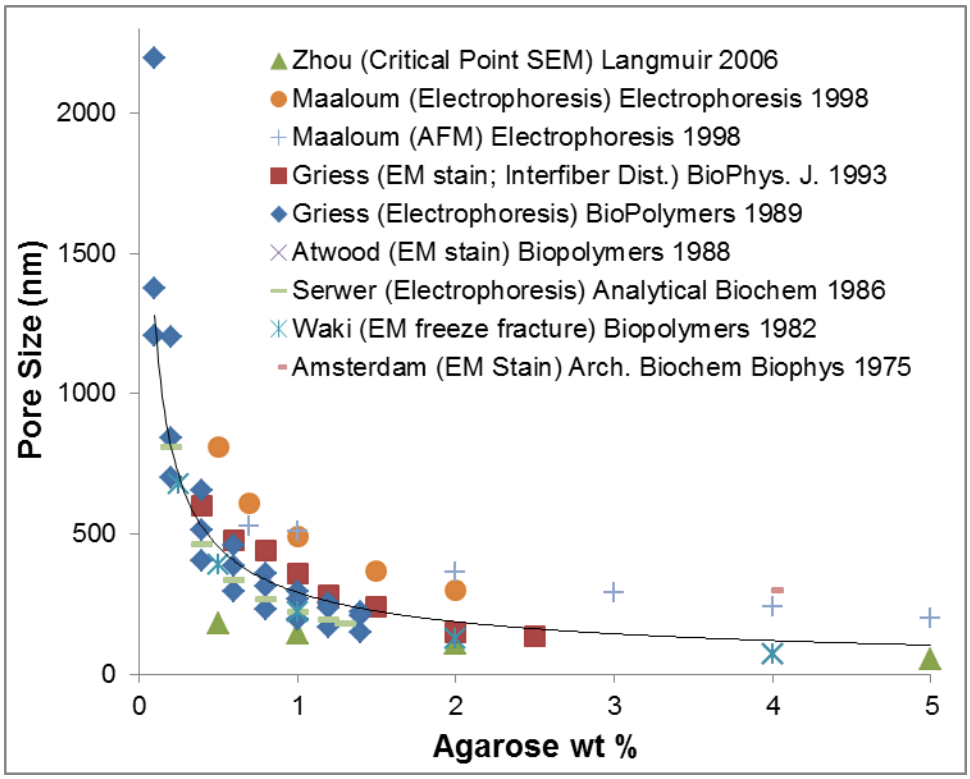

Figure 5.2 Summary of average agarose pore dimensions as a function of gel concentration with characterization method in parenthesis. Griess 1993 is an interfiber distance, rather than a pore diameter. Griess 1989 are data from low, medium and high electroendoosmosis (EEO) gels. Amsterdam 1975 pore size is a maximum 300 nm. The black line is an exponential curve fit to the aggregate data with equation $y = 292.61x^{-0.64}$.

Hardness testing by depth sensing nanoindentation is well-suited to provide insight into the interaction of a polymer fiber with an inorganic crystal. Hardness is a measure of a material's resistance to dislocation motion or plastic deformation. Hardness tests can yield quantitative information about how fibers hinder dislocation motion in a single crystal. Additionally, measurement of variations in hardness as a function of gel content may be able to determine whether the hardening mechanism is similar to

magnesium substitutions (Chapter 3), or if the fibers play an additional role as a non-deforming additive or fiber-reinforced composite.

5.2 Experimental Design

We developed an experimental setup that combines synthetic control over agarose additive content[20, 36] with control over crystallographic orientation necessary for quantitative mechanical testing.[37] Calcite single crystals, ~50 to 100 μm on edge (Figure 5.3), were grown by vapor diffusion of ammonium carbonate into gels containing 0.05 to 1.0 w/v % agarose and 5 mM $CaCl_2$. The calcite crystals nucleate in the gel, incorporate the agarose matrix during growth, and at low gel concentrations (<1 w/v%), retain their rhombohedral morphology. Crystals grown in agarose concentrations above 1 w/v % exhibited hopper or star-shaped morphologies (Figure 5.3e) and were excluded from this experiment because of concern that the samples would not align or be properly supported by the substrate.

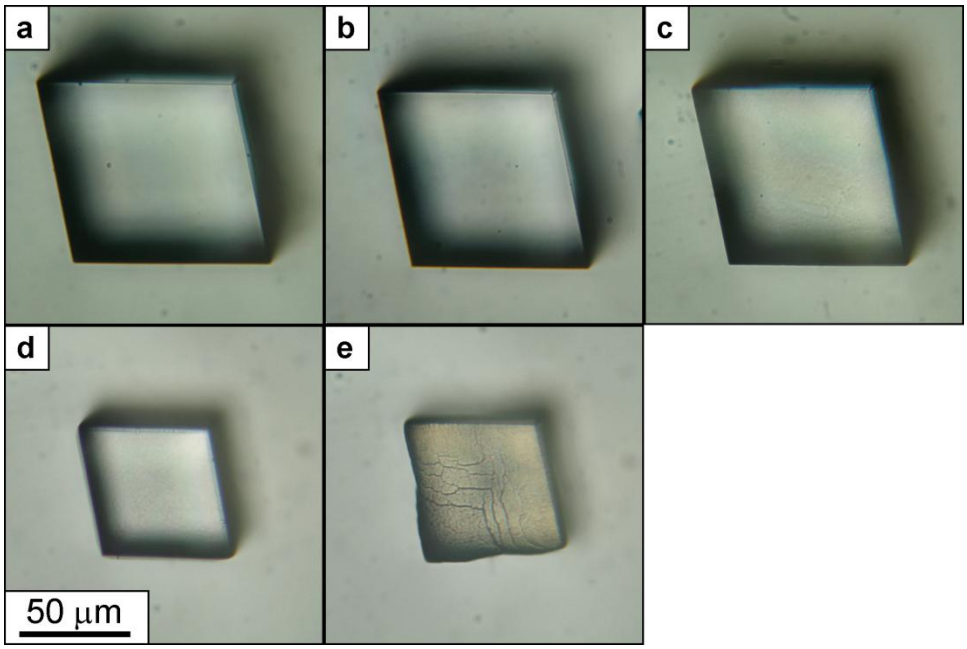

Figure 5.3 Optical micrographs of calcite crystals grown by gas diffusion into 5 mM calcium solutions containing 0.05, 0.1, 0.25, 1.0 or 3.0 w/v % agarose gel (a-e). Scale bar in (d) is for all panels.

Crystals grown in varying concentrations of agarose were extracted from the gels, rinsed, and individually oriented for mechanical testing on a patterned substrate (Figure 5.4a,b). The crystals were then fixed to the substrate by an overgrowth process, and embedded in superglue (Figure 5.4c). Finally, the crystals were polished to expose the (001) faces (Figure 5.4d) and tested by nanoindentation. Further details of the procedure can be found in Chapter 3.

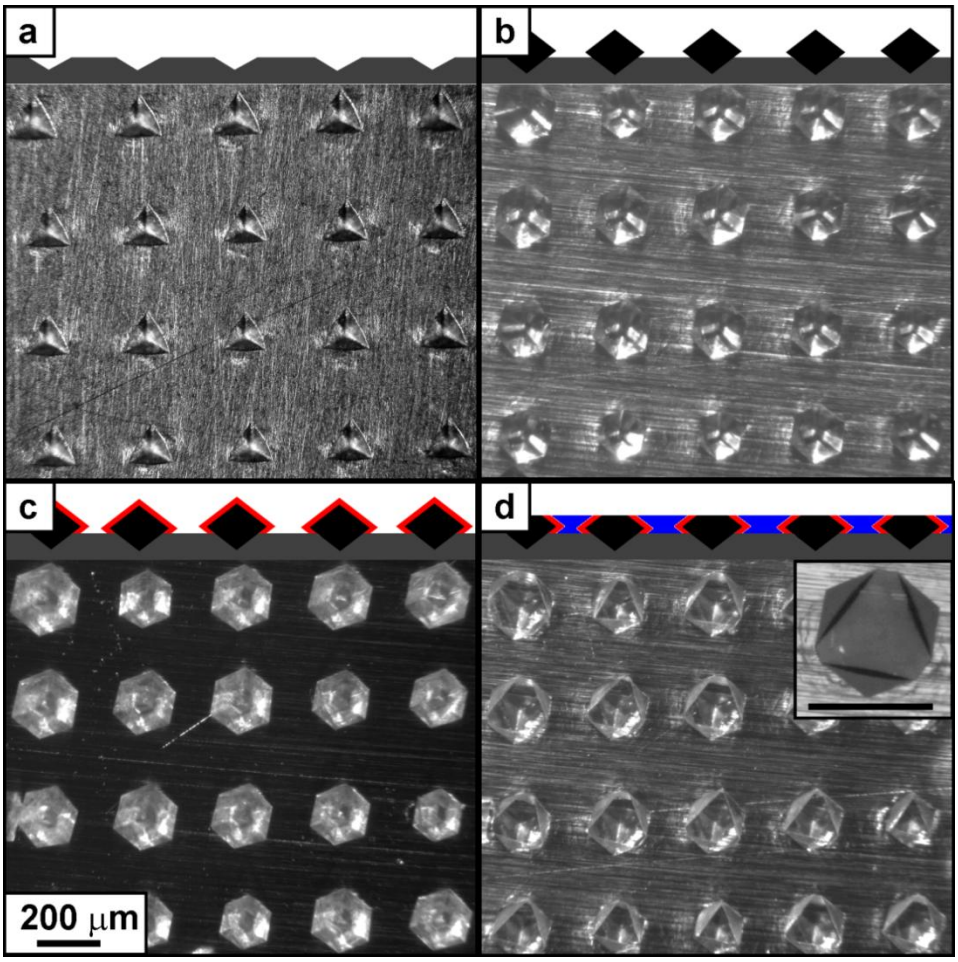

Figure 5.4 Schematic (side view) and light microscope images (top view) of experimental setup. (a) Representative array of impressions in Al substrate made to hold seed crystals with their c axis perpendicular to the substrate. (b) 0.05 w/v % crystals in impressions. (c) 0.05 w/v% crystals after ~10 μm overgrowth layer used to secure crystals to substrate. (d) 0.05 w/v% crystals with overgrowth layer embedded within cyanoacrylate resin and polished to expose (001) face. Inset uses focal plane lighting to show surface contrast. Scale bar in (c) is for all panels (a-d) and scale bar in the inset of (d) is also 200 μm. Schematic coloring: aluminum substrate (gray), calcite with agarose additive (black), calcite overgrowth (red), cyanoacrylate resin (blue).

We also measured the hardness variation due to relative rotation between indenter and sample, as indicated by azimuthal angle (see Chapter 2). Samples were measured in 10 degree increments between 0 and 60 degrees, sufficient to span the symmetry of the Berkovich indenter and (001) face of the calcite crystal. At least 11 indents were done on 3 crystals for all gel concentrations. A 2500 μN maximum load was chosen to ensure that the indents were deep enough (~200 nm) to minimize surface effects and sample a homogeneous distribution of organic material, while small enough to enable multiple indents per sample.

5.3 Results

5.3.1 Hardness

The hardness of calcite increases with the concentration of agarose gel in which the crystals were grown. The lowest hardnesses were found near the lowest agarose growth concentration (0.05 w/v%) and were similar to the values measured for geologic Iceland spar (2.3 to 2.5 GPa).[11] The highest hardness (3.26 ± 0.11 GPa at 60° azimuthal angle) was found near the highest agarose growth concentration (1 w/v %). The hardening rate with growth concentration of agarose gel was non-linear, initially increasing rapidly with increasing growth concentration and then plateauing at a maximum from 0.25 to 1 w/v % agarose. At two and three percent agarose concentrations, the hardness on the {104} faces decreases as compared to the 1 w/v% samples (data not shown).[38]

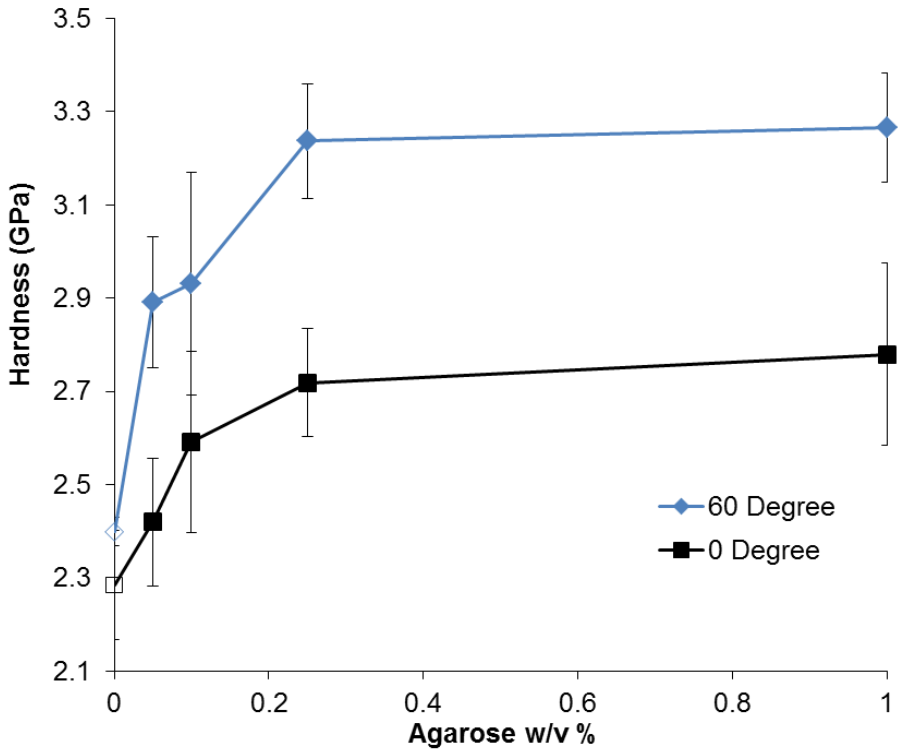

Figure 5.5 Hardness of the (001) face of calcite as a function of the concentration of agarose gel in which the crystals were grown. The black square and blue diamond represent 0 and 60 degree azimuthal angles. The hollow symbols at 0 w/v % correspond to a geologic reference. Each point represents at least 11 measurements on three crystals. The lines are intended as guides to the eye.

Hardness also varies with the relative rotation of the Berkovich indenter tip around the <001> indentation axis of the calcite crystal. Please see chapter 2 for more details on hardness as a function of azimuthal angle. For all concentrations tested, indentations at the 0 degree angle had a lower hardness than the 60 degree azimuthal angle. The hardening rates followed similar trends for the intermediate azimuthal angles from 10 to 50 degrees (Figure 5.6).

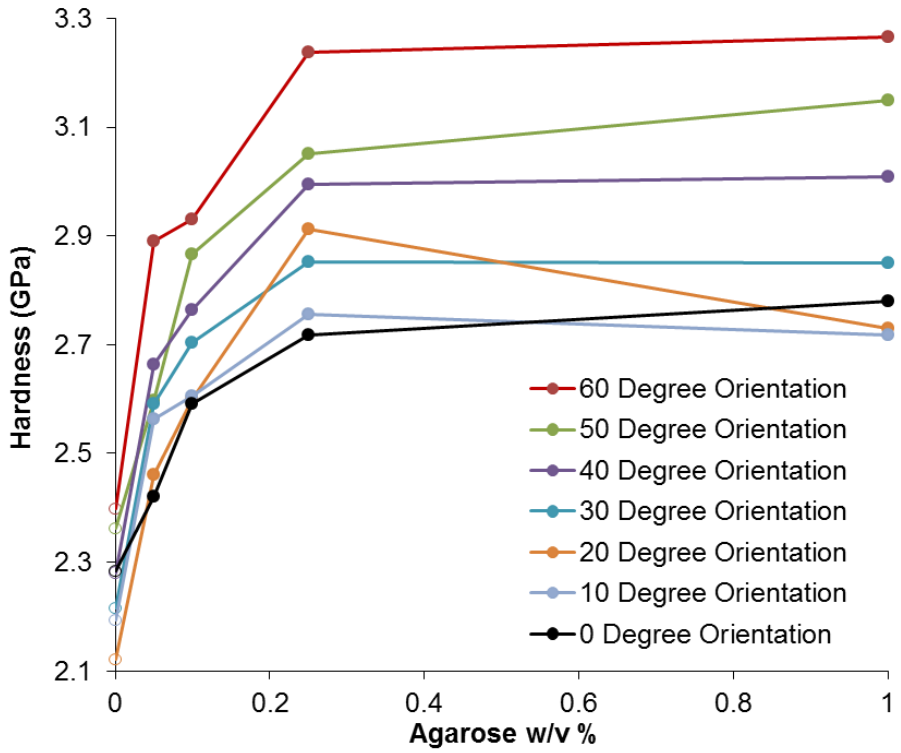

Figure 5.6 Hardness of the (001) face of calcite as a function of the concentration of agarose gel in which the crystals were grown for all tested azimuthal angles. Each point represents at least 11 measurements on three crystals. The hollow symbols at 0 w/v % correspond to a geologic reference. Error bars are not included for clarity but are similar to Figure 5.5.

5.3.2 Modulus

In contrast to the hardness, the plane strain indentation modulus values (Figure 5.7), did not show an increasing trend for the additive concentrations that were tested. The values were also similar to the values measured for the {001} face of pure, geologic Iceland spar, as expected for synthetic samples with small impurity concentrations.

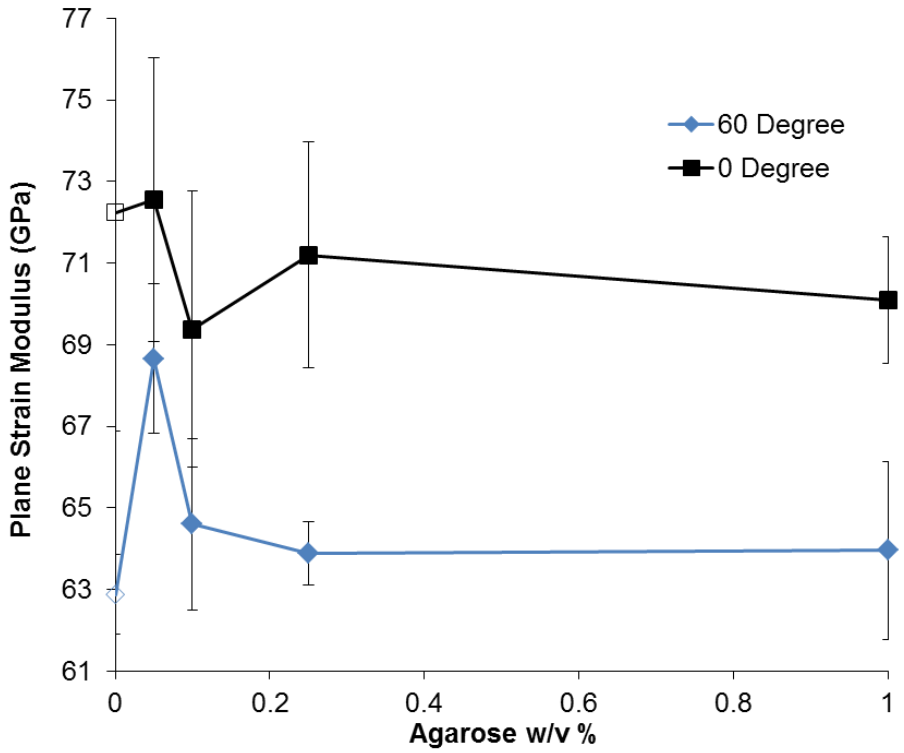

Figure 5.7 Plain strain indentation modulus as a function of concentration of agarose gel in which the crystals were grown. The 0 and 60 degree (black square and blue diamond) azimuthal angles are shown. The hollow symbols at 0 w/v % correspond to a geologic reference. Each point represents at least 11 measurements on three crystals. The lines are intended as guides to the eye.

5.3.3 Fracture

The effect of fracture on the relative hardness of the 0 and 60 degree orientations is visible in SEM images (Figure 5.8) that show the fracture patterns for all tested gel concentrations. Consistent with the results presented in Chapter 2, all crystals tested in the 0 degree azimuthal orientation show fracture patterns after indentation, while there are no crystals in the 60 degree orientation that show residual fracture patterns. Additionally, the SEM images of hybrid crystals grown at 0.25 and 1.0 w/v %, show the

intersections of large fibers with the surface, which leads to some pitting in the surface of the crystal polish.

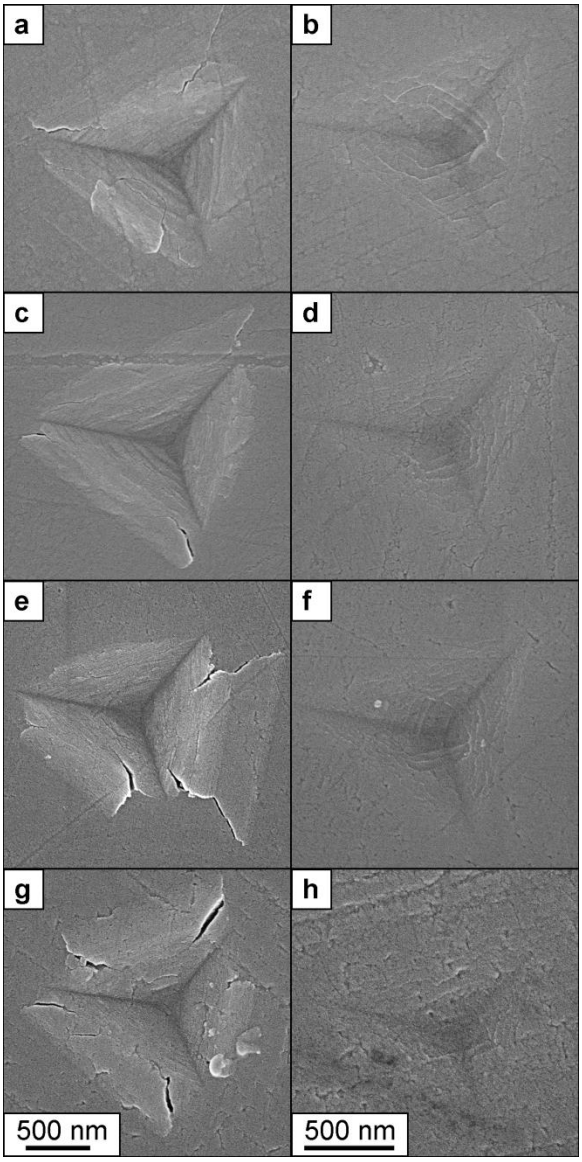

Figure 5.8 SEM images of impressions left after nanoindentation tests at 2500 μN. (a,c,e,and g) Indents at 0 degree orientation in hybrid crystals containing 0.05, 0.1, 0.25 and 1.0 w/v % agarose respectively. (b, d, f, and h) Indents at 60 degree orientation in hybrid crystals containing 0.05, 0.1, 0.25 and 1.0 w/v % agarose respectively.

5.4 Discussion

5.4.1 Hardening rate

The non-linear rate of hardening with growth concentration is different than the linear hardening rate found for magnesium substitutionals in Chapter 3.[37] There are several possible explanations for the non-linear hardening rate with growth concentration. One concern is that the actual agarose concentration inside the crystals is different than the agarose concentration in which the crystals were grown. However, thermal gravimetric analysis (TGA) has shown that the additive content found inside the synthetic calcite crystals is proportional to the gel concentration in which the crystals were grown, for growth conditions between 0.25 and 1.0 w/v% agarose IB.[20] This work includes data from crystals grown in 0.05 and 0.1 w/v % agarose IB, but we assume that the gel incorporation into the crystal is also proportional to growth concentration in this range, and therefore, the hardening rate would be non-linear as a function of either agarose growth concentration, or agarose weight content inside the crystal.

A second possible explanation for the non-linear hardening rate is that there is an indentation size effect that varies with concentration of the impurity. In this theory, the fibers act as a loose net that is easily deformable at small plastic strains, but becomes more rigid at high plastic strains. At low strain, the agarose fibers initially shear as the crystal plastically deforms to accommodate the indenter tip. However, eventually, as the strain at a fiber reaches some critical limit, it becomes impossible for the fibers to continue to shear. It then becomes energetically favorable for the calcite crystals to create dislocation loops around the agarose fibers, rather than shear through the material. At low agarose concentration, the indentation depth of ~200nm could be small enough that the

"high strain" region of the indentation volume never encompasses a fiber. At high agarose concentrations, the spacing between fibers would be small enough that the material acts as a homogeneous sample.[39] This critical limit could vary with the concentration of impurities, resulting in an increased hardening rate for a given indentation depth or strain as impurity concentration increases While there is a slightly larger deviation in hardness values at low concentrations in the 60 degree orientation, this may just be a reflection of inhomogeneity of the sample, and not an indentation size effect.

A third possible explanation is that the ionic concentration of salts during gelation affected the strength of the agarose gel inside the crystal. Higher ionic concentrations during growth have been shown to result in smaller pore diameters.[34] Since all crystals were grown in 5mM $CaCl_2$ solution, the low concentration gels would have a higher relative ionic strength than the high concentration gels. This difference might affect the strength and porosity of the gel in the crystal.

One final possible explanation for the non-linear hardening rate is that the gel structure changes as the concentration of agarose varies, leading to the faster increase in hardness at low gel concentrations. Although we only have HRTEM images of the fibers within the calcite crystals at 1 w/v % growth concentration,[18] we assume that the fiber structure inside the calcite crystal is identical to the fiber structure in the gel state for all growth concentrations. Fiber diameters are known to increase with increasing gel concentration leading to a higher fiber mass per unit length.[27, 28] It has also been proposed that incompletely networked fibers, "dead-ends", are more prevalent at lower gel concentrations.[28] Finally, an analysis of EM staining with computer analysis showed that

at low gel concentrations, the fibers appeared to have a biphasic distribution of distances between fibers.[29] Greiss et al. suggested that one explanation could be a gel composed of branched fiber units, rather than linear fibers. All of these differences may create a non-linear hardening rate with gel concentration.

The increased mass of an individual fiber with increased gel concentration could account for a leveling of the hardness between 0.25 and 1.0 w/v % (Figure 5.5). An increase in volume per fiber would have a negligible effect on calcite hardness, as the spacing between obstacles (~200-500 nm estimate from Figure 5.2) would only decrease minimally due to slightly thicker fibers (2-3 nm).[40] Whytock found that the fiber volume per unit length increased 2.5 fold when gel concentration increased from 4 fold from 0.5 to 2.0%,[28] implying that the pore diameter or should decrease by $(2.5/4)^{1/3}$ or by 16%. Waki found that the fiber volume increased 4 fold when gel concentration increased 16 fold from 0.25 to 4% suggesting a 37% decrease in pore diameter.

However, the increased thickness of fibers at higher gel concentrations conflicts with the rate of change of pore diameter with gel concentration. If fibers do get thicker at higher growth concentrations, then the pore size would be expected to decrease at a slower rate than has been measured. A geometrical argument would suggest that the pore diameter, or spacing between fibers should decrease as the concentration of fibers to the 1/2 or 1/3rd. However, the exponential curve fit from Figure 5.2 suggests that the spacing between fibers decreases at a faster rate; the pore diameter decreases as the concentration of fibers to the 0.64. It is uncertain why these two different methods of characterizing fiber density conflict with each other.

Nevertheless, using the exponential curve fit from Figure 5.2 to estimate fiber spacing at our growth concentrations, we calculated an expected hardness increase with agarose concentration.[41] For this calculation, we aggregated pore size data found by electrophoresis with distances found by electron and atomic force microscopy, into one curve fit that we approximated as distance between fibers. We then calculated the defect concentration as the inverse square of the distance between fibers. Since experimental data has suggested that yield strength and hardness should be proportional to the square root of defect concentration (Equation 2 and Equation 3) we plotted hardness as a function of defect concentration (Figure 5.9) calculated using the best fit data from Figure 5.2.[42] Equation 3 follows from Equation 2 since yield strength and hardness both measure resistance to plastic deformation.

Equation 2, σ_y represents the yield strength, σ_0 represents the defect free yield strength, a is a scaling constant, and c represents the concentration of defects. Equation 3 follows from Equation 2 since yield strength and hardness both measure resistance to plastic deformation.

Equation 2

$$\sigma_y = \sigma_0 + ac^{0.5} \qquad \text{(Equation 2)}$$

Equation 3

$$H = H_0 + ac^{0.5} \qquad \text{(Equation 3)}$$

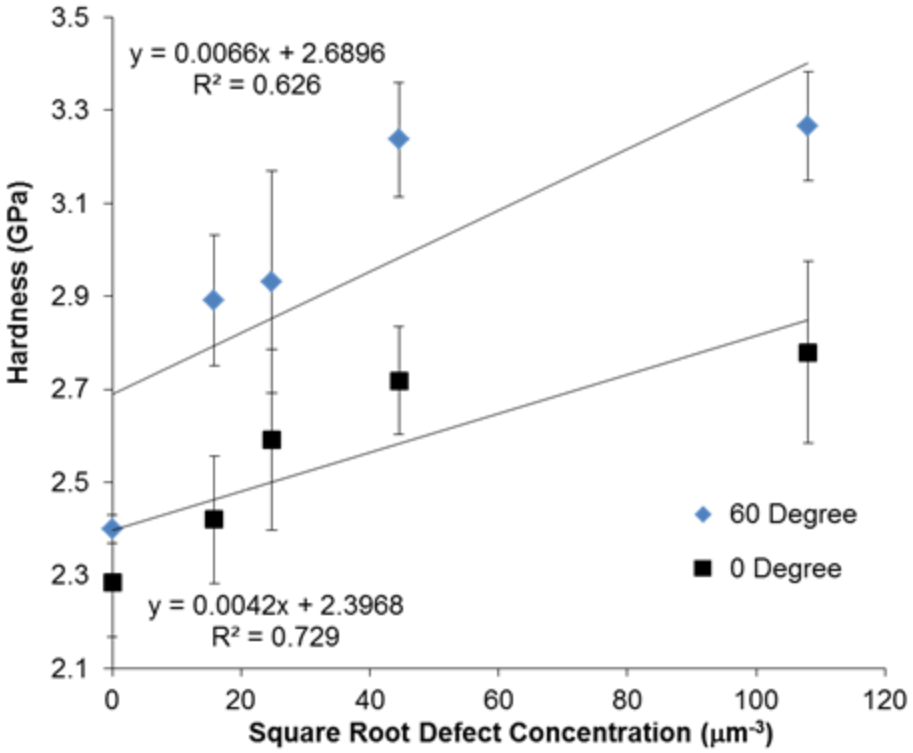

Figure 5.9 Hardness as a function of the square root of defect concentration.

5.4.2 Comparison to other synthetic calcites.

The agarose reinforced calcite crystals are harder than other synthetic calcites that incorporate organic macromolecule additives.[43-45] Furthermore, the incorporated weight percent of agarose is less than other literature examples, suggesting that agarose fibers are more effective at hardening synthetic calcite than the organic macromolecules used in other synthetic systems. One possible explanation for the higher hardness of the agarose incorporated crystals, is that the fibers may have a higher defect density despite a lower weight percent. Since the agarose fiber diameter ranges from 2 to 30 nm in gel systems, at 2 nm diameter, the defect density could be up to 100 times greater than the 20 nm micelles for an equal weight percent.

Table 3 Comparison of mechanical tests of synthetic calcites incorporating organic macromolecules.

Incorporated Macromolecule Additive	Weight % Additive	Hardness (GPa)	Comments	Reference
20 nm anionic diblock copolymer micelles	13 %	3.0 ± 0.16	29 vol %	[43]
Polyelectrolyte PSS	3 %	2.0 ± 0.25 2.4 ± 0.4	Location dependent (high polymer content, lower hardness)	[44]
Acidic glycoproteins from sea urchin spines	Undeter-mined	N/A	Glassy fracture in synthetic crystals vs brittle cleavage in geologic calcite	[45]
Agarose polymer	0.05 to 1.0 %	1.0 w/v % 3.26 ± 0.11	Increasing hardness with additive content	This work

5.4.3 Comparison to biogenic calcites

In comparison with biogenic calcite, the agarose reinforced calcite crystals measured for this chapter (Figure 5.10) are softer than calcite prisms from the mollusk, *Atrina rigida* (see Chapter 2). This result is not that surprising given the ~200 nm spacing between fibers seen in HRTEM of a 1 w/v% crystal[18] and the ~10 nm spacing between organic aggregates seen in *Atrina rigida*.[46] Therefore, it is possible that the decreased spacing between dislocation pinning sites in *Atrina rigida* is the source of the increased hardness when compared with gel grown calcite crystals, however, attempting to predict the hardness of *Atrina rigida* from Equation 3 while using constants found from the agarose data does not yield reasonable results.

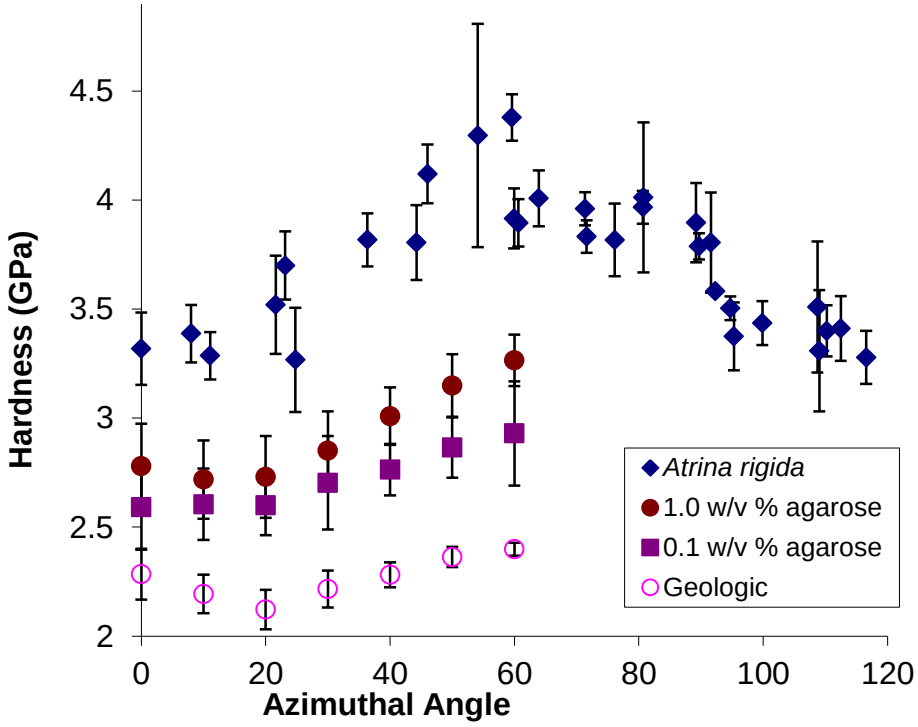

Figure 5.10 Hardness of agarose reinforced calcite crystals in comparison with geologic and biogenic calcite as a function of azimuthal angle. Each data point of geologic calcite consists of at least 9 indents in one crystal (see Chapter 2). The 0.1 and 1.0 w/v % data is from at least 3 crystals with at least 11 data points. The biogenic calcite data comes from 4 to 9 indents in *Atrina rigida* (see Chapter 2).

5.5 Conclusion

We have created synthetic calcite crystals with increased hardness and examined the effect of fiber reinforcement on the hardness of these crystals. We find that hardness increases with the concentration of agarose in which the crystal was grown. Additionally, we find that agarose fibers are not capable of hardening calcite to the level of biogenic calcite, but can harden calcite to the lower limit of substitutional impurities.

Hardness is found to vary with azimuthal angle in a similar manner to biogenic and magnesium doped calcite, and fracture patterns are not noticeably altered by the agarose fibers. We therefore believe that a strengthening mechanism based on the hindered dislocation motion could explain the increased hardness found in these synthetic samples, and would also be consistent with calcite strengthened by substitutional impurities or biogenic impurities.

One alternative viewpoint for the strengthening mechanism of agarose fibers in calcite, is that the mean free path of the dislocations are reduced by the free surfaces created by the agarose fibers. A parallel strengthening mechanism has been demonstrated in the literature for nanoporous metals, where dislocations may be impeded by free surfaces in a polycrystalline material.[47, 48] While voids have been known to impede dislocation motion in twins in calcite,[49] this may be an equivalent view of examining the same dislocation hardening mechanisms that we examine in this chapter. If it were possible to create nanoporous calcite with length scales on the order of 10 to 30nm through block-copolymer directed synthesis, it would be interesting to see if these materials had a similar modulus and hardness trend as that found in nanoporous metals.

5.6 Experimental

Crystal Growth: Calcite single crystals were grown by the gas diffusion method[36] in hydrogels containing 0.05-3.0 w/v% agarose (Type IB, Sigma) and 5 mM $CaCl_2$ ($CaCl_2 \cdot H_2O$, Strem Chemicals 99.999%). The hydrogels with a range of agarose concentrations were prepared by adding 0.05 to 1 gram of dry agarose powder to ~100 mL of 5 mM $CaCl_2$ solution to create a 0.05 to 3.0 w/v% agarose mixture. The agarose

mixture was heated in a microwave with intermittent stirring until all agarose powder dissolved. The solution was then cooled for 20 minutes under ambient conditions and ~15 mL aliquots were poured into 60 mm x 15 mm petri dishes. The petri dishes containing the agarose solutions were then covered with the loosely fitting top half of the petri dish and allowed to gel for approximately one hour at ambient temperature (Agarose 1B gel point ~36C).

Approximately 0.5 grams of $(NH_4)_2CO_3$ powder (Sigma-Aldrich), was then placed in a 20 ml glass scintillation vial and sealed with aluminum foil. A thin strip of parafilm was used to hermetically seal the aluminum foil to the vial. A needle was then used to create a small exit hole in the aluminum foil for the CO_2 and NH_4 gas diffusion.

The petri dishes and scintillation vial were then placed in a closed dessicator (~8L). The polymer reinforced calcite single crystals grew in the bulk gel for 18-24 hours. Crystals randomly nucleate in the gel and are suspended in the gel during growth, resulting in rhombohedral free floating crystals, ~60 to 80 μm on edge. The crystals were extracted by dissolving the agarose gel in two to three volumes of DI water heated to boiling conditions (18.2 MΩ, Barnstead EASYpure RoDI), and then rinsed with DI water followed by 100% ethanol. Upon melting of the gel, the dense crystals fall to the bottom of the solution where they can be physically extracted by pipette. The crystals were then dried under ambient conditions. The final yield of polymer reinforced calcite crystals was approximately 10 mg.

Substrate preparation: An array of impressions ~60 μm deep were made in 1/16 inch thick marine corrosion resistant aluminum 5052 (Speedy Metals) by using a home-built indenter that mimicked the morphology of the calcite rhombohedron. The home-

built cubic zirconia indenter was polished using an Imahashi crystal polisher (Faceting Unit Model FAC-8) to orient the cubic zirconia at the desired angles and polished with a graded set of aluminum oxide lapping films. The crystal polisher is accurate to within 1° and it is estimated from light microscopy that the radius of curvature of the tip of the cubic zirconia was ~3 μm. The polished crystal was then attached perpendicularly to the knife mount of a Sorvall MT 2B ultramicrotome and the manual stepper of the microtome was used to press the cubic zirconia indenter into the aluminum substrate. An array of ~40 impressions with 300 μm spacing was made, using the microtome's stage micrometers to reposition the indenter between impressions.

Sample Preparation: The aluminum substrate was submerged in 3 ml of 5 mM $CaCl_2$ contained in a 30 x 10 mm petri dish. Calcite crystals extracted from 0.05 to 1 w/v% agarose hydrogels, along with the 1 w/v% crystals that were subsequently annealed at different temperatures, were then sprinkled on top of liquid until they came to rest on the aluminum substrate. With the aid of a dissecting microscope, the crystals were then gently pushed into the impressions using a ~50 μm diameter glass fiber drawn by hand. When the crystals are above the impressions, gravity aligns the crystals such that the *c*-axis of each crystal is normal to the surface.

The crystals were then fixed to the aluminum substrate by overgrowing calcite following the gas diffusion process listed above. The substrates were then rinsed with DI water and ethanol.

Cyanoacrylate resin (Krazy Glue) was then poured over the top of the aluminum sample holders to encapsulate the crystals and allowed to dry overnight. The resin and crystals were polished by graded Al_2O_3 lapping films and a final 50 nm Al_2O_3 powder

(Buehler micropolish $\gamma-Al_2O_3$) suspended in a water and 2-methyl-2,4-pentanediol mix (Green Lube, Allied High Tech) until the crystals were exposed for measurement. The surface roughness following this protocol was less than 10 nm RMS.

Nanoindentation: Load-displacement measurements were performed using a Berkovich (~120 nm tip radius) diamond indenter on a commercial nanoindenter system (Hysitron Triboindenter) in quasistatic mode. Prior to data collection, the shape of the tip was calibrated using the method of Oliver and Pharr.[50] Each indent consisted of five second load, hold, and unload segments with a maximum 2500 μN load, with the unloading segment used to calculate the indentation modulus and hardness.[51] The resulting indentations were ~200 nm deep. Surface topography scans were performed with the indenter tip before and after indenting to ensure indentations were located at least 5 μm away from any edges.

Fluorescence Microscopy: Samples were imaged using an Olympus BH2 microscope with reflected light fluorescence attachment. The microscope was equipped with a 20UG1 exciter filter and DM400 dichroic mirror. The mercury arc lamp excitation was primarily at 334 and 365 nm while the dichroic mirror allowed fluorescence light with wavelengths greater than 400 nm to be transmitted. Images were captured on a Olympus C-7070 camera fitted to the microscope.

1. Gordon LM, Joester D. Nanoscale chemical tomography of buried organic-inorganic interfaces in the chiton tooth. *Nature* 2011, **469**(7329)**:** 194-198.

2. Lins U, Farina M, Kurc M, *et al.* The Otoconia of the Guinea Pig Utricle: Internal Structure, Surface Exposure, and Interactions with the Filament Matrix. *J Struct Biol* 2000, **131**(1)**:** 67-78.

3. Towe KM, Lowenstam HA. Ultrastructure and development of iron mineralization in radular teeth of cryptochiton stelleri (mollusca). *Journal of Ultrastructure Research* 1967, **17**(1-2)**:** 1.

4. Gertman R, Ben Shir I, Kababya S, Schmidt A. In Situ Observation of the Internal Structure and Composition of Biomineralized Emiliania huxleyi Calcite by Solid-State NMR Spectroscopy. *J Am Chem Soc* 2008, **130**(40)**:** 13425-13432.

5. Ross MD, Pote KG. Some Properties of Otoconia. *Philosophical Transactions of the Royal Society of London Series B, Biological Sciences* 1984, **304**(1121)**:** 445-452.

6. Nudelman F, Chen HH, Goldberg HA, Weiner S, Addadi L. Spiers memorial lecture: lessons from biomineralization: comparing the growth strategies of mollusc shell prismatic and nacreous layers in *Atrina rigida*. *Faraday Discuss* 2007, **136:** 9-25.

7. Ma YR, Cohen SR, Addadi L, Weiner S. Sea urchin tooth design: an "all-calcite" polycrystalline reinforced fiber composite for grinding rocks. *Adv Mater* 2008, **20**(8)**:** 1555-1559.

8. Fantner GE, Hassenkam T, Kindt JH, Weaver JC, Birkedal H, Pechenik L, *et al.* Sacrificial bonds and hidden length dissipate energy as mineralized fibrils separate during bone fracture. *Nat Mater* 2005, **4**(8)**:** 612-616.

9. Asenath-Smith E, Li H, Keene EC, Seh ZW, Estroff LA. Crystal Growth of Calcium Carbonate in Hydrogels as a Model of Biomineralization. *Adv Funct Mater* 2012, **22**(14)**:** 2891-2914.

10. Wang RZ, Addadi L, Weiner S. Design strategies of sea urchin teeth: structure, composition and micromechanical relations to function. *Phil Trans R Soc B* 1997, **352**(1352)**:** 469-480.

11. Kunitake ME, Mangano LM, Peloquin JM, Baker SP, Estroff LA. Evaluation of strengthening mechanisms in calcite single crystals from mollusk shells. *Acta Biomater* 2013, **9**(2)**:** 5353-5359.

12. Moureaux C, Pérez-Huerta A, Compère P, Zhu W, Leloup T, Cusack M, *et al.* Structure, composition and mechanical relations to function in sea urchin spine. *J Struct Biol* 2010, **170**(1)**:** 41-49.

13. Pérez-Huerta A, Cusack M, Zhu W, England J, Hughes J. Material properties of brachiopod shell ultrastructure by nanoindentation. *J R Soc Interface* 2007, **4**(12)**:** 33-39.

14. Pérez-Huerta A, Cusack M, Zhu W. Assessment of crystallographic influence on material properties of calcite brachiopods. *Mineral Mag* 2008, **72**(2)**:** 563-568.

15. Griesshaber E, Schmahl WW, Neuser R, Pettke T, Blum M, Mutterlose J, *et al.* Crystallographic texture and microstructure of terebratulide brachiopod shell calcite: An optimized materials design with hierarchical architecture. *Am Mineral* 2007, **92**(5-6)**:** 722-734.

16. Aizenberg J, Hendler G. Designing efficient microlens arrays: lessons from Nature. *J Mater Chem* 2004, **14**(14)**:** 2066-2072.

17. Li H, Estroff LA. Porous calcite single crystals grown from a hydrogel medium. *Crystengcomm* 2007, **9**(12)**:** 1153.

18. Li HY, Xin HL, Muller DA, Estroff LA. Visualizing the 3D Internal Structure of Calcite Single Crystals Grown in Agarose Hydrogels. *Science* 2009, **326**(5957)**:** 1244-1247.

19. Paquette J, Reeder RJ. Relationship between surface structure, growth mechanism, and trace element incorporation in calcite. *Geochim Cosmochim Ac* 1995, **59**(4)**:** 735-749.

20. Li HY, Estroff LA. Calcite growth in hydrogels: assessing the mechanism of polymer-network incorporation into single crystals. *Adv Mater* 2009, **21**(4)**:** 470-473.

21. Ritchie R. Mechanisms of fatigue-crack propagation in ductile and brittle solids. *International Journal of Fracture* 1999, **100**(1)**:** 55-83.

22. Launey ME, Ritchie RO. On the fracture toughness of advanced materials. *Adv Mater* 2009, **21**(20)**:** 2103-2110.

23. Lahaye M, Rochas C. Chemical-Structure and Physicochemical Properties of Agar. *Hydrobiologia* 1991, **221:** 137-148.

24. Zhou JF, Zhou MF, Caruso RA. Agarose template for the fabrication of macroporous metal oxide structures. *Langmuir* 2006, **22**(7)**:** 3332-3336.

25. Ratajska-Gadomska B, Gadomski W. Water structure in nanopores of agarose gel by Raman spectroscopy. *J Chem Phys* 2004, **121**(24)**:** 12583-12588.

26. Griess GA, Edwards DM, Dumais M, Harris RA, Renn DW, Serwer P. Heterogeneity of the Pores of Polysaccharide Gels - Dependence on the Molecular-Weight and Derivatization of the Polysaccharide. *J Struct Biol* 1993, **111**(1)**:** 39-47.

27. Waki S, Harvey JD, Bellamy AR. Study of agarose gels by electron microscopy of freeze-fractured surfaces. *Biopolymers* 1982, **21**(9)**:** 1909-1926.

28. Whytock S, Finch J. The Substructure of Agarose Gels as Prepared for Electrophoresis. *Biopolymers* 1991, **31**(9)**:** 1025-1028.

29. Griess GA, Guiseley KB, Serwer P. The Relationship of Agarose-Gel Structure to the Sieving of Spheres during Agarose-Gel Electrophoresis. *Biophysical Journal* 1993, **65**(1)**:** 138-148.

30. Amsterdam A, Erel Z, Shaltiel S. Ultrastructure of Beaded Agarose. *Archives of Biochemistry and Biophysics* 1975, **171**(2)**:** 673-677.

31. Griess GA, Moreno ET, Easom RA, Serwer P. The Sieving of Spheres during Agarose-Gel Electrophoresis - Quantitation and Modeling. *Biopolymers* 1989, **28**(8)**:** 1475-1484.

32. Attwood TK, Nelmes BJ, Sellen DB. Electron microscopy of beaded agarose gels. *Biopolymers* 1988, **27**(2)**:** 201-212.

33. Serwer P, Hayes SJ. Exclusion of spheres by agarose gels during agarose gel electrophoresis: dependence on the sphere's radius and the gel's concentration. *Anal Biochem* 1986, **158**(1)**:** 72-78.

34. Maaloum M, Pernodet N, Tinland B. Agarose gel structure using atomic force microscopy: Gel concentration and ionic strength effects. *Electrophoresis* 1998, **19**(10)**:** 1606-1610.

35. Pernodet N, Maaloum M, Tinland B. Pore size of agarose gels by atomic force microscopy. *Electrophoresis* 1997, **18**(1)**:** 55-58.

36. Aizenberg J, Black AJ, Whitesides GM. Control of crystal nucleation by patterned self-assembled monolayers. *Nature* 1999, **398**(6727)**:** 495-498.

37. Kunitake ME, Baker SP, Estroff LA. The effect of magnesium substitution on the hardness of synthetic and biogenic calcite. *MRS Communications* 2012, **2**(03)**:** 113-116.

38. Peloquin JM. Mechanical properties of calcite/agarose single crystal composites: a model system for biogenic minerals. 2009.

39. Tabor D. Hardness of solids. *Endeavour* 1954, **13**(49)**:** 27-32.

40. Courtney TH. *Mechanical behavior of materials*. McGraw-Hill, 1990.

41. Ashby MF. The deformation of plastically non-homogeneous materials. *Philosophical Magazine* 1970, **21**(170)**:** 399-424.

42. Gilman JJ. Theory of Solution Strengthening of Alkali-Halide Crystals. *J Appl Phys* 1974, **45**(2)**:** 508-509.

43. Kim YY, Ganesan K, Yang P, Kulak AN, Borukhin S, Pechook S, *et al.* An artificial biomineral formed by incorporation of copolymer micelles in calcite crystals. *Nat Mater* 2011, **10**(11)**:** 890-896.

44. Schenk AS, Zlotnikov I, Pokroy B, Gierlinger N, Masic A, Zaslansky P, *et al.* Hierarchical Calcite Crystals with Occlusions of a Simple Polyelectrolyte Mimic Complex Biomineral Structures. *Adv Funct Mater* 2012**:** n/a-n/a.

45. Berman A, Addadi L, Weiner S. Interactions of sea urchin skeleton macromolecules with growing calcite crystals- a study of intracrystalline proteins. *Nature* 1988, **331**(6156)**:** 546-548.

46. Li H, Xin HL, Kunitake ME, Keene EC, Muller DA, Estroff LA. Calcite prisms from mollusk shells (*Atrina rigida*): swiss-cheese-like organic–inorganic single-crystal composites. *Adv Funct Mater* 2011**:** 2028-2034.

47. Biener J, Hodge AM, Hamza AV, Hsiung LM, Satcher JH. Nanoporous Au: A high yield strength material. *J Appl Phys* 2005, **97**(2)**:** 024301-024304.

48. Biener J, Hodge AM, Hayes JR, Volkert CA, Zepeda-Ruiz LA, Hamza AV, *et al.* Size effects on the mechanical behavior of nanoporous Au. *Nano Letters* 2006, **6**(10)**:** 2379-2382.

49. Boĭko VS. *Reversible crystal plasticity*. American Institute of Physics: New York :, 1994.

50. Oliver WC, Pharr GM. Measurement of hardness and elastic modulus by instrumented indentation: advances in understanding and refinements to methodology. *J Mater Res* 2004, **19**(1)**:** 3-20.

51. Oliver WC, Pharr GM. An improved technique for determining hardness and elastic modulus using load and displacement sensing indentation experiments. *J Mater Res* 1992, **7**(6)**:** 1564-1583.

CHAPTER 6

6 CONCLUSIONS

This thesis presented a quantitative assessment of the factors that affect the hardness and modulus of biogenic calcite. In Chapter 2, we demonstrated the effect of crystallographic orientation on the measured values of biogenic and geologic calcite. We then examined the effect of impurities ranging from atomic substitutions (Chapter 3) to amino acids (Chapter 4) to long chain polymers (Chapter 5). Finally, we began to explore the effect of crystal quality (Appendices). By individually examining the effect of each factor, we have a better understanding of the strengthening mechanism responsible for the increased hardness found in biogenic calcite.

We find that all of the results are consistent with a standard materials science model of hardening due to hindered dislocation motion (Chapter 1). This standard model proposes that hardness is a measure of the difficulty of a material to plastically deform and rearrange its relative atomic position. Chapter 2 showed that certain crystallographic directions in calcite are more difficult to deform than others, consistent with the standard model that hardness is dependent on the stress state applied to crystallographic planes. Chapters 3, 4 and 5 showed that the hardness of calcite increases with impurity concentration, whether the impurity is due to magnesium, cysteine, glycine, aspartic acid, or agarose. This is consistent with the standard model that impurities and their associated stress fields pin the relative motion of crystalline atoms. Finally, the appendices and chapter 4 begin to suggest that hardness can be altered by crystal defects in general and that impurities alone are one subcategory of defects in crystal quality. The variation in hardness caused by changes in crystallographic orientation and impurity or defect

concentration, are all consistent with a strengthening mechanism based on hindered dislocation motion.

In previous chapters, the results from synthetic samples and biogenic samples from the mollusks *Atrina rigida* and *Pinna nobilis* were compared with a reference geologic Iceland spar. Summarizing the results in Figure 6.1 shows two distinct trends. For all samples with controlled orientation, the relative increase in hardness at the 60° orientation is larger than at the 0° orientation. Even though the reference geologic Iceland spar is already harder at the 60° orientation, when dividing the hardness of the 0° orientation of the sample by the 0° orientation of the reference, and the hardness of the 60° orientation of the sample by the 60° orientation of the reference, all measured samples increase in hardness at a faster rate in the 60° orientation. Secondly, the harder the sample, the larger the percentage difference between the 0° and 60° orientations.

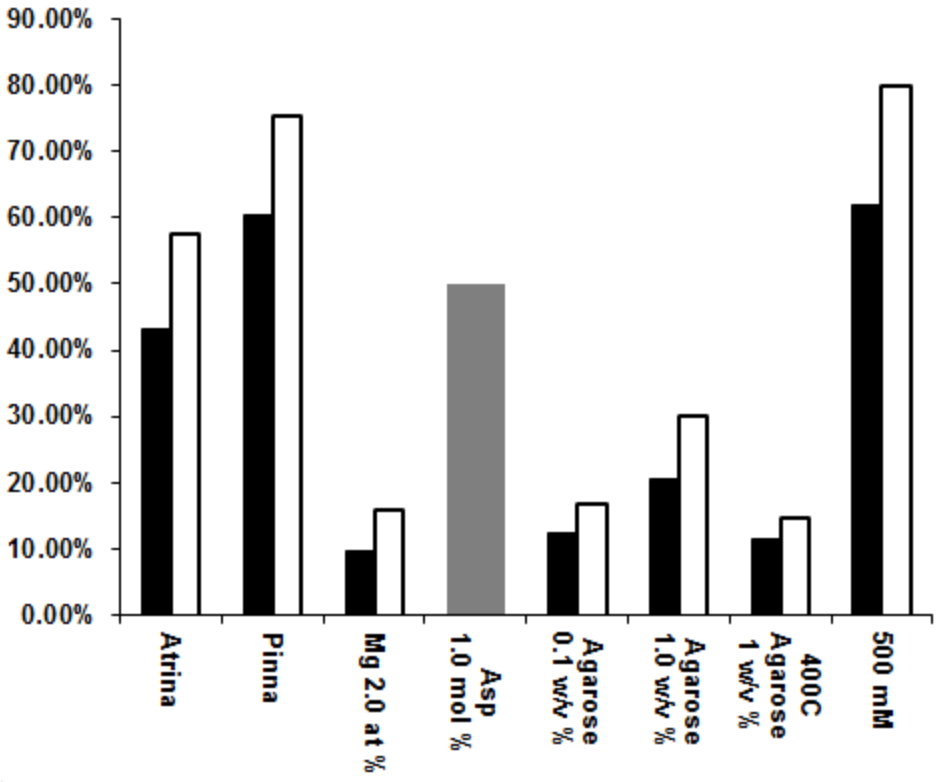

Figure 6.1 Percentage hardness increase relative to geologic Iceland spar at the 0° orientation (filled) and 60° orientation (empty). Aspartic acid is an average of all orientations (shaded).

Based upon the aggregated results of these hardness tests, we can begin to understand why biogenic calcite is harder than geologic calcite. We have determined the relative importance of impurities such as magnesium, amino acids, and polymer chains to the increased hardness of biogenic calcite. We have also quantified the variation in measured results due to changes in crystallographic orientation.

However, further research is needed to answer whether the biomineralization process is responsible in some way for the increased hardness of biogenic samples. While geologic and synthetic calcite is typically formed through classical nucleation and growth, it is thought that biogenic calcite is via and amorphous precursor. If biogenic

crystals are formed through an amorphous calcium carbonate (ACC) precursor, does this growth mechanism result in a higher impurity concentration? Does an ACC precursor lead to kinetically trapped defects and a higher defect density? Since hardness is a material property that is dependent on the history of the sample, it is important to understand how the biomineralization process affects hardness. We may then hope to use mechanical property tests to shed light on the biomineralization process.

APPENDIX 1

A1 FRACTURE MORPHOLOGY OF BIOGENIC AND GEOLOGIC CALCITE

A1.1 Introduction

Conchoidal fracture has been proposed in the literature to be a distinctive hallmark of biogenic calcite as opposed to cleavage along {104} planes seen in geologic calcite.[1-3] However, the paper by Towe, often cited to demonstrate this difference,[4] noted that conchoidal fracture can also be seen in geologic calcite.[4, 5] Much of the fracture differences noted between geologic and biogenic calcite and even within biogenic calcite measurements may be due to differences in the stress state applied during the fracture experiment.[3, 4]

To emphasize the similarities in fracture morphology between geologic and biogenic calcite that had been demonstrated in the paper by Towe, we oriented geologic calcite in the form of Iceland spar and biogenic calcite from the prismatic layer of the mollusk *Atrina rigida* in the same crystallographic direction and scratched the surface of both crystals (Figure A6.2). Although these results may not be applicable to comparisons between geologic calcite and sea urchin spines, in this particular instance, it is possible to see similar fracture patterns as well as residual twin lamellae, indicative of plastic deformation in both geologic and biogenic calcite (Figure A6.2c).

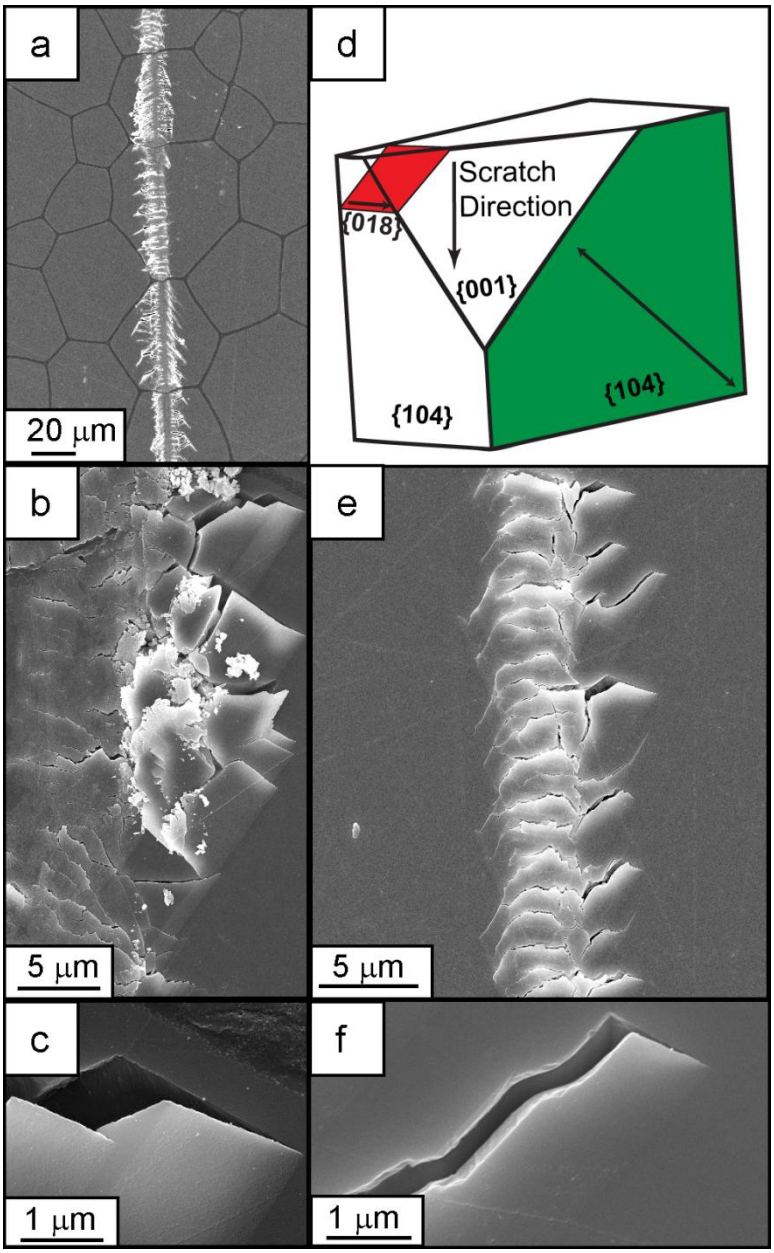

Figure A6.2 Scratch tests on the (001) face of the prismatic layer of *Atrina rigida* and geologic calcite. (a-c) Low to high magnification scanning electron microscope images of *Atrina rigida* fracture. Panel c shows the twinning planes extend across several microns. (d) Schematic illustrating direction of scratch on geologic sample. (e-f) Low and high magnification images of scratches on geologic calcite.

1. Berman A, Addadi L, Weiner S. Interactions of sea urchin skeleton macromolecules with growing calcite crystals- a study of intracrystalline proteins. *Nature* 1988, **331**(6156)**:** 546-548.

2. Seto J, Ma Y, Davis SA, Meldrum F, Gourrier A, Kim Y-Y, *et al.* Structure-property relationships of a biological mesocrystal in the adult sea urchin spine. *Proc Natl Acad Sci* 2012, **109**(10)**:** 3699-3704.

3. O' Neill PL. Polycrystalline echinoderm calcite and its fracture mechanics. *Science* 1981, **213**(4508)**:** 646-648.

4. Towe KM. Echinoderm calcite: single crystal or polycrystalline aggregate. *Science* 1967, **157**(3792)**:** 1048-1050.

5. Currey JD, Nichols D. Absence of organic phase in echinoderm calcite. *Nature* 1967, **214**(5083)**:** 81.

APPENDIX 2

A2 THERMAL GRAVIMETRIC ANALYSIS OF ATRINA RIGIDA

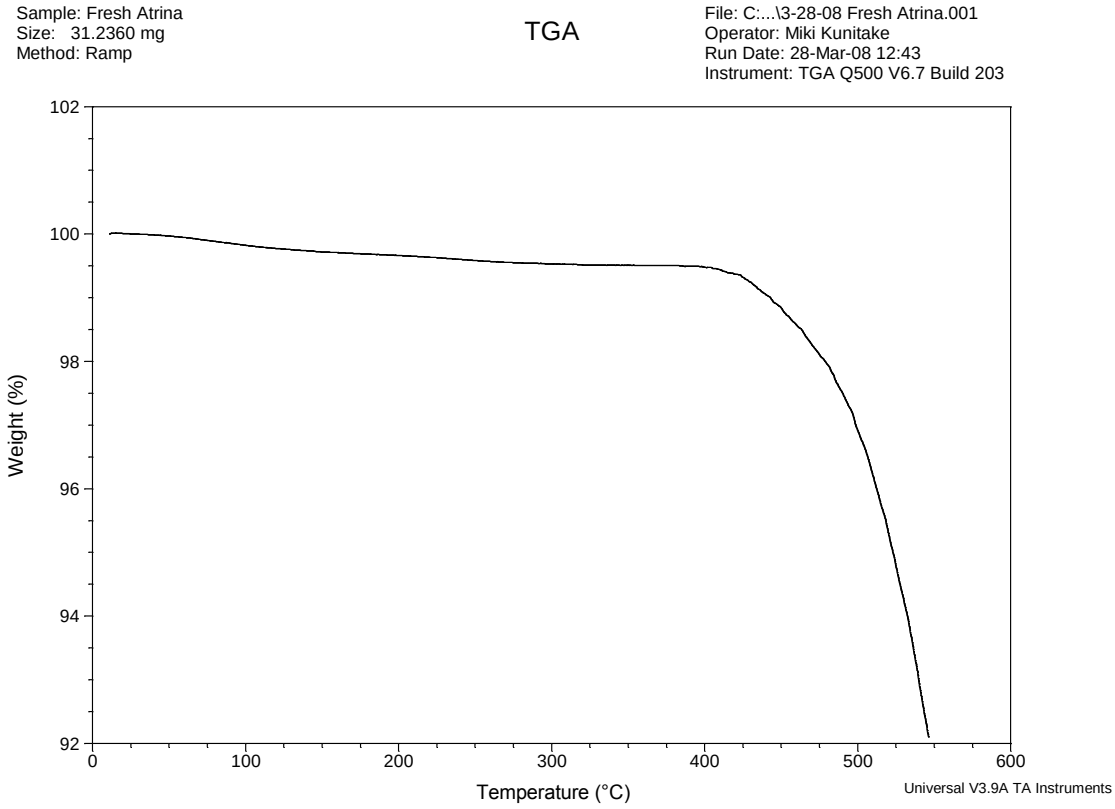

Figure A6.3 TGA data showing weight loss of *Atrina rigida* prisms heated at 5° C/min under air atmosphere.

APPENDIX 3

A3 THE EFFECTS OF HEATING ON THE HARDNESS OF POLYMER REINFORCED CALCITE

A3.1 Introduction

We would like to know if the fiber-like structure of agarose affects its ability to alter the mechanical properties of calcite. If the same amount of agarose were incorporated inside single crystal calcite as disconnected spheres, rather than as connected fibers, would the calcite be as hard? Fortunately, agarose decomposes at a lower temperature than calcite, allowing selective decomposition and removal of organic fibers from the crystal matrix.[1] By measuring the hardness of single crystal calcite containing agarose as a function of annealing temperature, we can gain some insight into the role of fiber structure on the hardness of calcite.

Several methods can be used to track the agarose fiber structure after heating. Previous thermal gravimetric analysis (TGA) of dried agarose shows an initial pyrolysis at about 250 °C, losing 70% of its weight, followed by a final 30% loss at about 450 °C.[2] Numerous decomposition byproducts were detected including monomer sugar units, and acidic small molecules.[3] Under a nitrogen atmosphere, TGA of calcite crystals with occluded agarose fibers shows a similar decomposition temperature for the first and second stages, though the second decomposition at 450 °C is relatively smaller in magnitude in the calcite crystals (Figure A6.4).[4] HRTEM tomography of 1 w/v % calcite crystals shows that between 300 and 400 °C, channels left behind by decomposed fibers collapse to form spheres, minimizing their surface energy.[1]

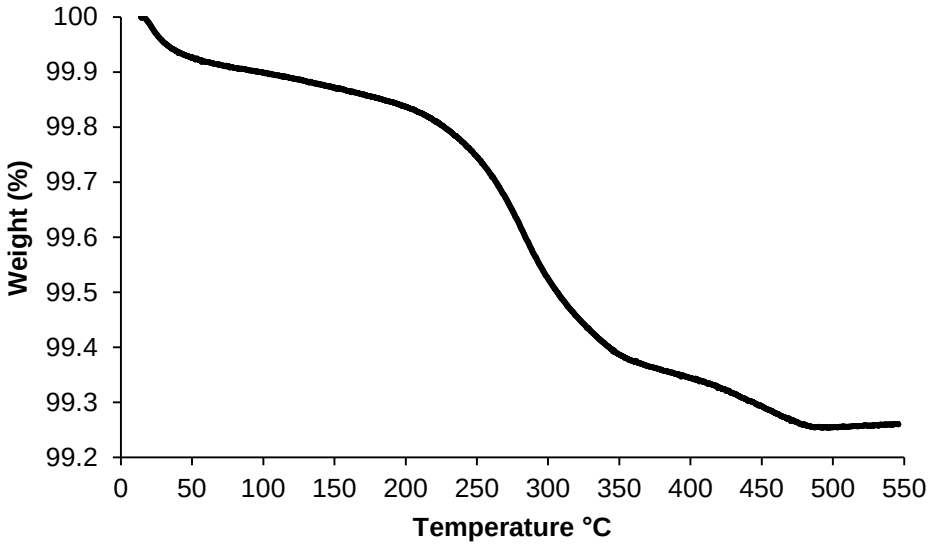

Figure A6.4 Representative TGA curve for calcite crystals grown in 1 w/v% Agarose IB and 5 mM $CaCl_2$. The sample was heated at 5 °C / minute under nitrogen atmosphere.

Fluorescence microscopy can also track the decomposition of agarose (Figure A6.5). Agarose natively fluoresces,[5] which enables us to track the condition of the fiber within calcite crystals as a function of temperature.

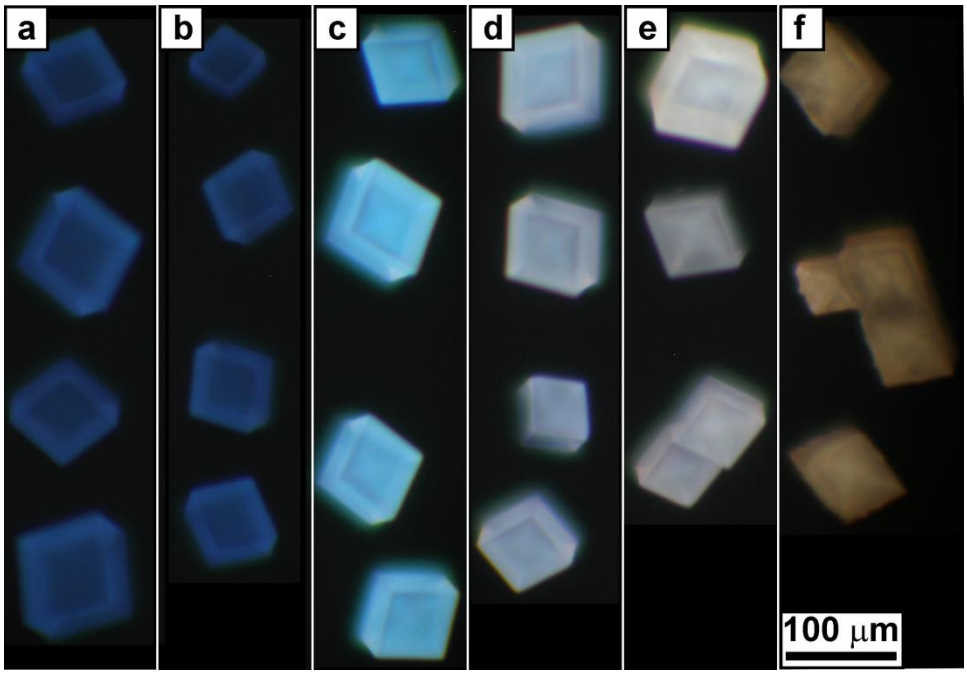

Figure A6.5 Fluorescence microscope images of 1 w/v % calcite crystals heated for 1 hour under ambient atmosphere. (a) As prepared (b) 100 °C (c) 200 °C (d) 300 °C (e) 400 °C (f) 500 °C.

A3.2 Experimental Design

Crystal Heating and Polymer Removal: 1 w/v% polymer reinforced calcite crystals were sprinkled onto glass slides and placed in a furnace (Thermo Scientific F6000) under ambient atmosphere. Each sample was then heated from ambient conditions at a 5 °C per minute ramp rate and held at the annealing temperature for 1 hour. Five target temperatures were used ranging from 100 to 500 °C in 100 degree increments. However, the 500 °C crystals appeared to have an oily coating on the crystals, and so were not tested. The as-prepared to 400 °C samples were tested by nanoindentation and imaged by fluorescence microscopy to examine the effect of organic removal.

A3.3 Conclusions

The hardness of 1 w/v % calcite crystals is greatest as prepared, and decreases with increased heating temperature (Figure A6.6). However, the plane strain indentation modulus was unchanged upon heating (Figure A6.4).

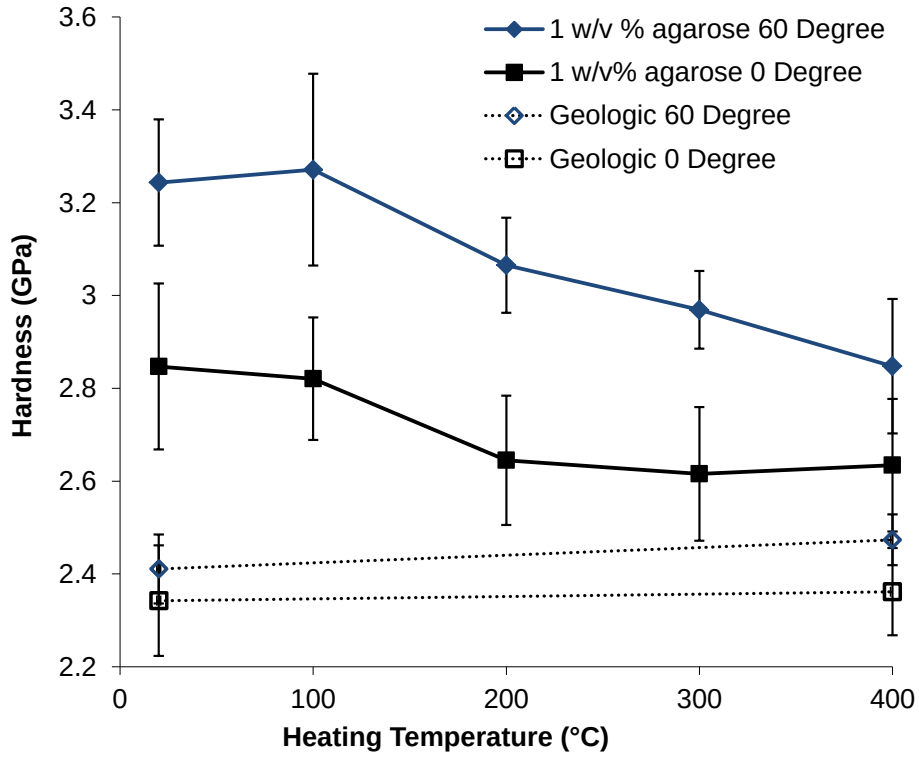

Figure A6.3 Hardness of 1 w/v % calcite crystals annealed for one hour (solid figures) and measured at the 0 and 60 degree azimuthal orientations. Geologic crystals (open figures) were also tested at room temperature and after annealing at 400C. For the 1 w/v % crystals, each data point is an average of 5 crystals totaling 45 measurements. The geologic data points each represent 16 measurements on 1 crystal. The connecting lines are intended as guides for the eye.

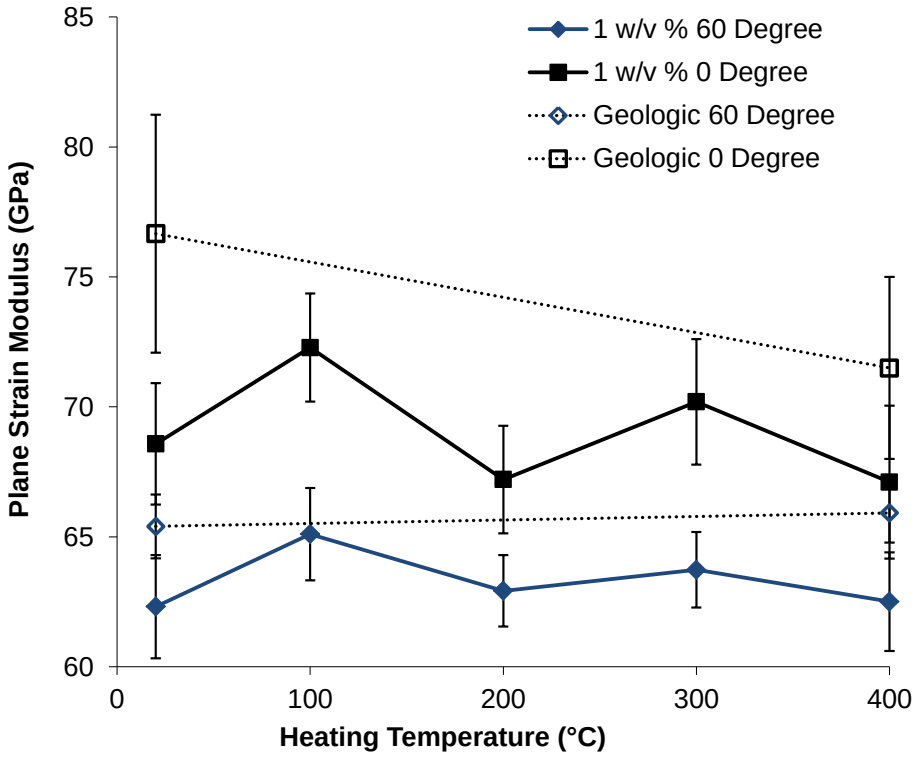

Figure A6.4 Plane strain indentation modulus of 1 w/v % calcite crystals annealed for one hour (solid figures) and measured at the 0 and 60 degree azimuthal orientations. Geologic crystals (open figures) were also tested at room temperature and after annealing at 400C. For the 1 w/v % crystals, each data point is an average of 5 crystals totaling 45 measurements. The geologic data points each represent 16 measurements on 1 crystal. The connecting lines are intended as guides for the eye.

A3.4 Discussion

It is interesting to note that the decrease in agarose hardness coincides with the decrease in weight by TGA as well as changes in fluorescent intensity; all three have marked changes between 100 and 300C.

The decreased hardness upon heating may be due to two effects. The fibers may be directly related to strengthening the calcite crystals as non-deforming obstacles and

this additional strengthening mechanism is lost upon heating (See chapter 1). A non-deforming additive has a greater yield strength than that of the dislocations that interact with it. Therefore, instead of moving to accommodate the dislocation, the dislocation moves to accommodate the second phase resulting in secondary dislocations which can then interact to further strengthen the material. Alternatively, the dislocation density (ie. distance between dislocations) may decrease with heating. HRTEM of as prepared crystals vs. heated crystals, shows that the spacing increases between fibers (as prepared) and voids (heated). When these fibers convert to voids upon heating, we assume that the conversion is volume conserving and so does not affect the percentage of the crystal that contains an additive (i.e. the volume of the crystal does not decrease upon fiber removal) but the spacing between defects increases as the high surface area fibers coalesce into three dimensional spheres.

One possible concern about annealing the samples is that the voids inside the crystals may be under pressure and therefore assist in making the crystal more brittle. Nanoindentation of these samples might read a lower hardness due to fracture during the indentation. However, both the 0 and 60 degree data do not appear to have any trend nor are they distinguishable from the as prepared samples ranging from 0 to 1 w/v %. We therefore believe that the similar modulus values for all annealed temperatures indicates that the voids do not cause or hinder fracture in any significant manner.

Fibers have been shown to act as crack branching toughenners in brittle materials, however, we do not believe that crack arrest is responsible for the increased hardness of agarose occluded calcite. An increased R-curve or toughening rate in a brittle ceramic when reinforced with niobium wires versus niobium particles,[18-20] and response of

collagen fibrils under AFM loading,[21] shows that fibers can act extrinsically,[19] and toughen a material after a crack has occurred. However, in the case of nanoindentation hardness, the agarose fibers act as an intrinsic strengthener, resisting plastic deformation before cracks appear. The smaller hardness difference between 0° and 60° orientations when the crystals are heated and fibers removed, is contrary to what might be expected from a crack branching toughener. Since visual cracking as imaged by SEM occurs only in the 0° orientation, we would expect the 0° orientation to be closer in hardness to the 60° orientation when fibers are present. In fact, when fibers are not present (at high annealing temperatures), the hardness difference is smallest between 0° and 60° orientation is the smallest. This would suggest that crack bridging does not occur with agarose fibers or that the effect on hardness is not measurable.

One alternative viewpoint for the strengthening mechanism of agarose fibers in calcite, is that the mean free path of the dislocations are reduced by the free surfaces created by the agarose fibers. A parallel strengthening mechanism has been demonstrated in the literature for nanoporous metals, where dislocations may be impeded by free surfaces in a polycrystalline material.[22, 23] While voids have been known to impede dislocation motion in twins in calcite,[24] this may be an equivalent view of examining the same dislocation hardening mechanisms that we examine in this chapter. If it were possible to create nanoporous calcite with length scales on the order of 10 to 30nm through block-copolymer directed synthesis, it would be interesting to see if these materials had a similar modulus and hardness trend as that found in nanoporous metals.

1. Li HY, Xin HL, Muller DA, Estroff LA. Visualizing the 3D Internal Structure of Calcite Single Crystals Grown in Agarose Hydrogels. *Science* 2009, **326**(5957)**:**

1244-1247.

2. Zhou JF, Zhou MF, Caruso RA. Agarose template for the fabrication of macroporous metal oxide structures. *Langmuir* 2006, **22**(7)**:** 3332-3336.

3. Fabbri D, Chiavari G. Analytical pyrolysis of carbohydrates in the presence of hexamethyldisilazane. *Anal Chim Acta* 2001, **449**(1)**:** 271-280.

4. Li HY, Estroff LA. Calcite growth in hydrogels: assessing the mechanism of polymer-network incorporation into single crystals. *Adv Mater* 2009, **21**(4)**:** 470-473.

5. Koch CA, Li PCH, Utkhede RS. Evaluation of thin films of agarose on glass for hybridization of DNA to identify plant pathogens with microarray technology. *Anal Biochem* 2005, **342**(1)**:** 93-102.

6. Griess GA, Guiseley KB, Serwer P. The Relationship of Agarose-Gel Structure to the Sieving of Spheres during Agarose-Gel Electrophoresis. *Biophysical Journal* 1993, **65**(1)**:** 138-148.

7. Courtney TH. *Mechanical behavior of materials*. McGraw-Hill, 1990.

8. Turner FJ, Griggs DT, Heard H. Experimental deformation of calcite crystals. *Geol Soc Am Bull* 1954, **65**(9)**:** 883-933.

9. Barber DJ, Wenk HR, Gomez-Barreiro J, Rybacki E, Dresen G. Basal slip and texture development in calcite: new results from torsion experiments. *Phys Chem Miner* 2007, **34**(2)**:** 73-84.

10. Barber DJ, Wenk HR. Deformation twinning in calcite, dolomite, and other rhombohedral carbonates. *Phys Chem Miner* 1979, **5**(2)**:** 141-165.

11. DeBresser JHP, Spiers CJ. Strength characteristics of the r, f, and c slip systems in calcite. *Tectonophysics* 1997, **272**(1)**:** 1-23.

12. Parke M, Adams I. The motile (Crystallolithus hyalinus Gaarder & Markali) and non-motile phases in the life history of Coccolithus pelagicus (Wallich) Schiller. *J Mar Biol Assoc UK* 1960, **39**(02)**:** 263-274.

13. Young JR, Henriksen K. Biomineralization within vesicles: The calcite of coccoliths. *Reviews in mineralogy and geochemistry* 2003, **54**(1)**:** 189-215.

14. Funnell BM, Riedel WR. *The Micropalaeontology of Oceans: Proceedings of the Symposium Held in Cambridge from 10 to 17 September 1967 Under the Title'Micropalaeontology of Marine Bottom Sediments'*. Cambridge University Press, 1971.

15. Young JR, Davis SA, Bown PR, Mann S. Coccolith Ultrastructure and Biomineralisation. *J Struct Biol* 1999, **126**(3)**:** 195-215.

16. Okazaki M, Sato T, Mutho N, Wada N, Umegaki T. Calcified scales (coccoliths) of *Pleurochrysis carterae* (Haptophyta): Structure, crystallography, and acid polysaccharides. *J Mar Biotechnol* 1998, **6**(1)**:** 16-22.

17. Asenath-Smith E, Li H, Keene EC, Seh ZW, Estroff LA. Crystal Growth of Calcium Carbonate in Hydrogels as a Model of Biomineralization. *Adv Funct Mater* 2012, **22**(14)**:** 2891-2914.

18. Badrinarayanan K, McKelvey A, Ritchie R, Venkateswara Rao K. Fracture and fatigue-crack growth behavior in ductile-phase toughened molybdenum disilicide: Effects of niobium wire <i>vs particulate reinforcements. *Metallurgical and Materials Transactions A* 1996, **27**(12)**:** 3781-3792.

19. Ritchie R. Mechanisms of fatigue-crack propagation in ductile and brittle solids. *International Journal of Fracture* 1999, **100**(1)**:** 55-83.

20. Launey ME, Ritchie RO. On the fracture toughness of advanced materials. *Adv Mater* 2009, **21**(20)**:** 2103-2110.

21. Fantner GE, Hassenkam T, Kindt JH, Weaver JC, Birkedal H, Pechenik L*, et al.* Sacrificial bonds and hidden length dissipate energy as mineralized fibrils separate during bone fracture. *Nat Mater* 2005, **4**(8)**:** 612-616.

22. Biener J, Hodge AM, Hamza AV, Hsiung LM, Satcher JH. Nanoporous Au: A high yield strength material. *J Appl Phys* 2005, **97**(2)**:** 024301-024304.

23. Biener J, Hodge AM, Hayes JR, Volkert CA, Zepeda-Ruiz LA, Hamza AV*, et al.* Size effects on the mechanical behavior of nanoporous Au. *Nano Letters* 2006, **6**(10)**:** 2379-2382.

24. Boĭko VS. *Reversible crystal plasticity*. American Institute of Physics: New York :, 1994.

APPENDIX 4

A4 THE EFFECTS OF GROWTH RATE ON THE HARDNESS OF CALCITE

A4.1 Introduction

Increased growth rates have been shown to lead to an increased concentration of defects in synthetic calcite.[1-4] In the case of impurity defects, a higher concentration of impurities is found inside synthetic calcite grown at higher calcium and carbonate precursor concentrations, even at constant impurity concentrations. Higher growth rates also lead to a higher concentration of impurity-free defects such as screw dislocations at the center of spiral hillocks, and voids seen in AFM scans under high supersaturation.[1]

Since the concentration of defects should affect the hardness of a material by hindering plastic dislocation, changes in growth rate may produce crystals with altered mechanical properties. Here, we measure the hardness of single crystal calcite grown at different solute concentrations and compare the results with biogenic calcite.

A4.2 Experimental Design

Calcite crystals containing 0.1 w/v % agarose were placed in oriented holders, overgrown with high-growth-rate calcite, polished to expose the (001) face, and the seed and overgrowth were measured for hardness by nanoindentation. We used seed crystals isolated from a 0.1 w/v % agarose gel because of their ready availability, uniform size, and previously measured hardness and modulus (Chapter 5). Following the mounting procedure for magnesium overgrowth[5], 0.1 w/v % seed crystals were manually placed into an aluminum or nickel holder such that *c*-axis of the crystal was normal to the substrate. The oriented crystals were then placed into growth chambers containing 15

mM, 100 mM, 175 mM, 250 mM or 500 mM $CaCl_2$ solutions and overgrown using gas diffusion of $(NH_4)_2(CO_3)$. Due to unwanted random spontaneous nucleation at higher growth concentrations, the 175, 250 and 500 mM sets were grown in a small (~100 μL) diffusion chamber while the 15 and 100 mM sets were grown in a large (~4L) chamber. The concentration of CO_2 was not monitored during the growth. All samples were then polished to expose the (001) face and measured by nanoindentation at two azimuthal angles.

A4.3 Results

The hardness of the overgrowth region is dependent on the concentration in which the crystal was grown. The overgrown calcite is similar in hardness to geologic Iceland spar when grown in 15 and 100 mM $CaCl_2$ solutions (Figure A6.7). However, the overgrown calcite is harder than geologic calcite when grown in 175, 250 or 500 mM $CaCl_2$ solution. The non-linear increase in hardness between crystals grown below 100 mM $CaCl_2$ and those grown above 175 mM $CaCl_2$ is likely due to differences in the growth chambers; the higher concentration samples were grown in smaller chambers so the gas diffusion of the $(NH_4)_2(CO_3)$ was much more rapid in these samples.

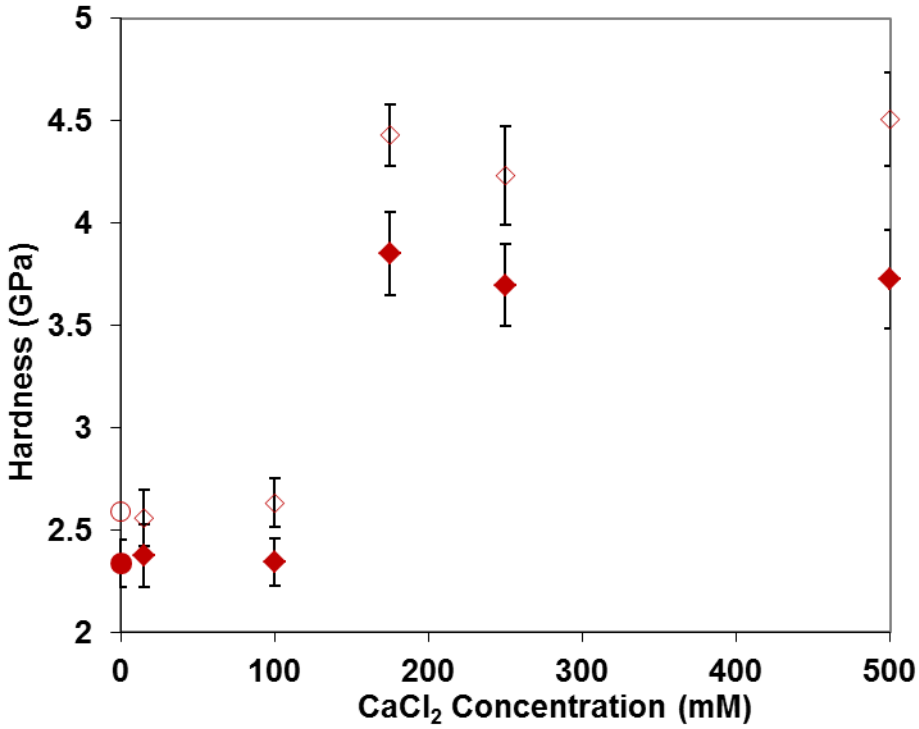

Figure A6.7 Hardness of calcite as a function of growth concentration. Geologic Iceland spar (circles) and overgrown calcite (diamonds). Filled symbols represent the 0 degree orientation while unfilled symbols represent the 60 degree orientation. Each data set represents at least 19 measurements on at least 4 crystals.

The hardness of the overgrowth region was also mapped for one crystal grown at 250 mM $CaCl_2$ (Figure A6.8). The hardness of the seed crystal is 3.0 ± 0.29 GPa while the hardness of the overgrowth region is 4.1 ± 0.23 GPa. There is a slight increase in hardness with distance from the seed crystal as seen by increasing hardness with indent number for each row.

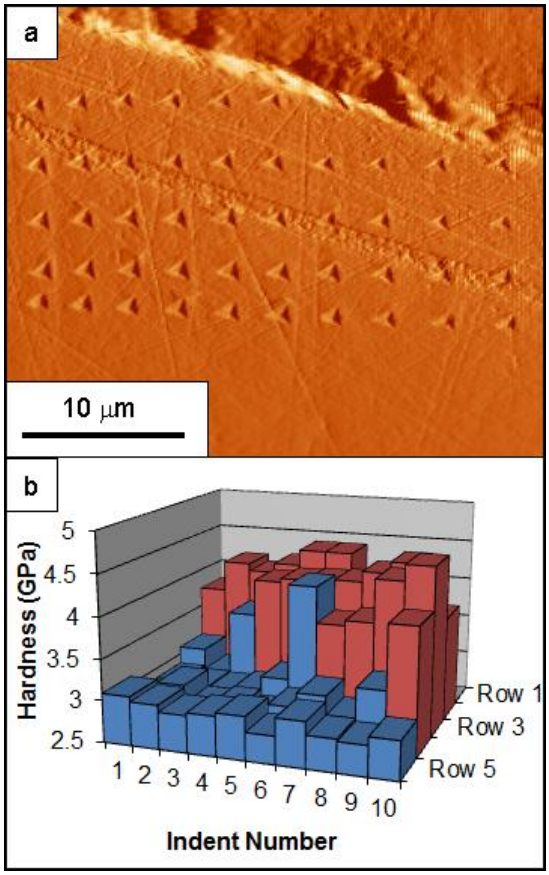

Figure A6.8 a. Surface scan using nanoindenter tip. b. Corresponding hardness of the overgrown high-growth-rate calcite (250 mM $CaCl_2$) (red) and 0.1 w/v % calcite seed crystal (blue). The spacing between indents is 3 μm.

The plane strain indentation modulus is similar for all growth concentrations (data not shown).

A4.4 Discussion

Calcite grown at high supersaturations and high growth rates is harder than calcite grown at low precursor concentrations. Since higher growth rates have been shown to lead to more defects, these results are consistent with the theory that the hardness of calcite is increased due to defects which hinder plastic dislocation motion.

The hardness of calcite grown at very high growth rates is equivalent to the

hardness found in *Atrina rigida* and *Pinna nobilis*. If the defects found in synthetic high-growth-rate calcite are intrinsic dislocations and not due to impurities, then it is possible that a significant portion of the increased hardness of biogenic calcite may result from changes in crystal quality rather than biogenic impurities.

1. Teng HH, Dove PM, DeYoreo JJ. Reversed calcite morphologies induced by microscopic growth kinetics: insight into biomineralization. *Geochim Cosmochim Ac* 1999, **63**(17)**:** 2507-2512.

2. Teng HH, Dove PM, Orme CA, De Yoreo JJ. Thermodynamics of calcite growth: baseline for understanding biomineral formation. *Science* 1998, **282**(5389)**:** 724-727.

3. Wasylenki LE, Dove PM, Wilson DS, De Yoreo JJ. Nanoscale effects of strontium on calcite growth: An in situ AFM study in the absence of vital effects. *Geochim Cosmochim Ac* 2005, **69**(12)**:** 3017-3027.

4. Paquette J, Reeder RJ. Relationship between surface structure, growth mechanism, and trace element incorporation in calcite. *Geochim Cosmochim Ac* 1995, **59**(4)**:** 735-749.

5. Kunitake ME, Baker SP, Estroff LA. The effect of magnesium substitution on the hardness of synthetic and biogenic calcite. *MRS Communications* 2012, **2**(03)**:** 113-116.

APPENDIX 5

A5 HARDNESS AND MICROSTRUCTURE OF PINNA NOBILIS[f]

A5.1 Introduction

Pinna nobilis is a mollusk that has been used as a model subject for studies of growth patterning, mineral anisotropic lattice distortions and crystalline nanostructure.[1-3] Here we examine the hardness, modulus, and microstructure of the outer prismatic layer and compare the results with the mollusk *Atrina rigida.*

A5.2 Experimental Process

All samples were obtained from a large, ~25 year old, *Pinna nobilis* shell. (Figure A6.9) The *Pinna nobilis* shell is composed of an inner nacreous layer and an outer calcite prismatic layer. The prismatic layer is comprised of calcite prisms up to a few millimeters long, all oriented with the *c*-axis normal to the shell surface.

[f] I would like to thank Dr. Stephan E. Wolf for his collaboration in designing experiments, preparing samples and collecting experimental data for this section.

Figure A6.9 Fragment of a *Pinna nobilis* shell. Samples were taken from the region of the inset box.

Five samples, each approximately 1 cm by 1 cm by 0.6cm (shell thickness), were excised from the shell and embedded in epoxy. One sample was oriented and polished such that the naturally occurring outer prismatic layer was exposed for crystallographic orientation determination, hardness measurement and quantitative elemental analysis. A second sample was oriented so that a cross section of the shell would be exposed for elemental analysis. The other samples were preserved as backup samples.

The mechanical properties of calcite are dependent on crystallographic orientation,[4, 5] and magnesium content.[6] We therefore determined the absolute crystallographic orientation of the prisms by electron backscatter diffraction (EBSD) to prior to measuring the hardness and modulus by nanoindentation (Figure A6.10). The

relative in-plane rotation of the calcite to the three-fold symmetry of the indenter tip was also controlled for during the measurement. Magnesium content was measured by wavelength dispersive spectroscopy on the indentation surface as well as down the length of the prism.

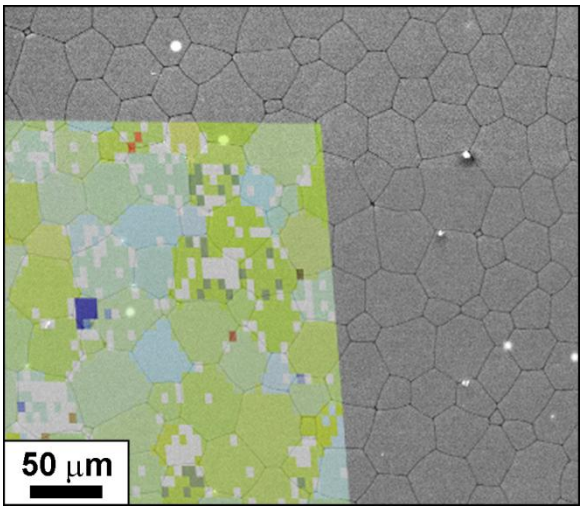

Figure A6.10 Top view of a polished prismatic layer with an overlay of the EBSD map used to determine crystallographic orientation. The color of each 5 μm by 5 μm pixel is generated by plotting the three Euler angles that correlate the calcite crystal orientation at that location to a constant reference coordinate system as red, green, and blue color intensities.

A5.3 Results

The hardness of the prismatic layer of *Pinna nobilis* indented on the {001} face, varies with azimuthal angle and ranges from 3.7 to 4.4 GPa (Figure A6.11) The lowest values are found near $\varphi = 0°$ and the highest at $\varphi = 60°$. The hardness values are ~0.3 GPa higher than *Atrina rigida* and ~2 GPa harder than geologic Iceland spar.

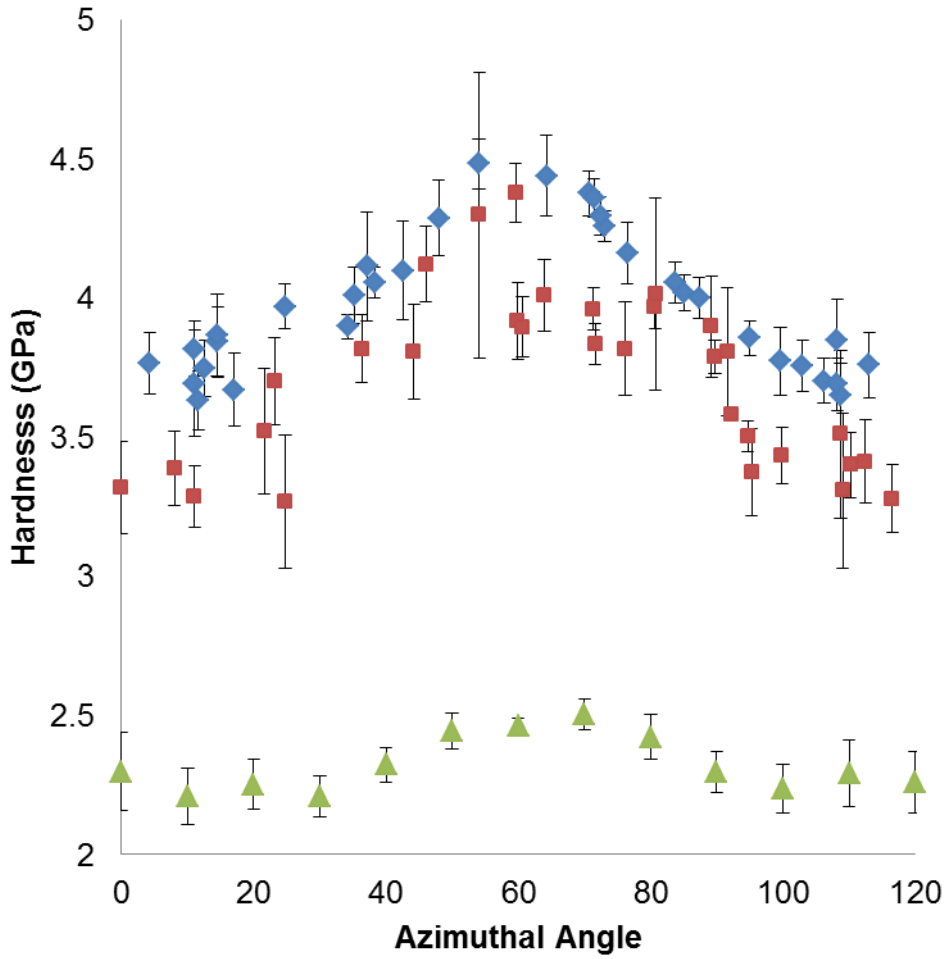

Figure A6.11 Plot of hardness as a function of azimuthal angle for *Pinna nobilis* (blue diamonds), *Atrina rigida* (red squares) and geologic calcite (green triangles). Each azimuthal angle is an average of 8 indents for *Pinna nobilis*, 4 to 8 indents for *Atrina rigida* and 9 to 27 indents for the geologic sample. Error bars represent one standard deviation.

The modulus values are similar for *Pinna nobilis*, *Atrina rigida* and geologic Iceland spar (Figure A6.12). There appears to be a slight decrease in modulus at $\varphi = 60°$ which is more pronounced in the geologic sample.

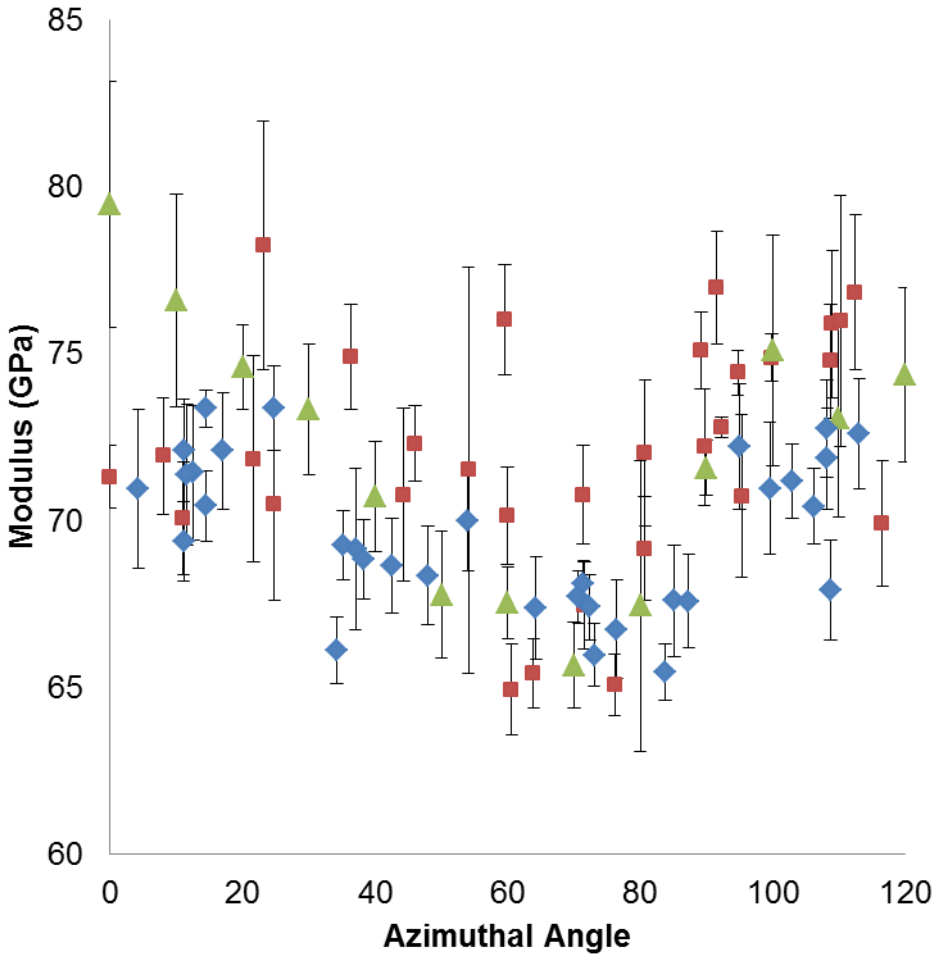

Figure A6.12 Plot of plane strain indentation modulus as a function of azimuthal angle for *Pinna nobilis* (blue diamonds), *Atrina rigida* (red squares) and geologic calcite (green triangles).

The magnesium content of *Pinna nobilis* as measured on seven prisms ranged from 0.6 to 1.4 weight percent MgO (1.15 to 2.94 at. %) with an average of 0.79 weight percent (1.64 at. %). The magnesium is not evenly distributed within the prismatic layer; scans down the length of the prism showed that magnesium content is partitioned into zones on the order of 100μm in spacing (Figure A6.13). The magnitude and zoned distribution of magnesium content are consistent with previous literature data.[1, 2]

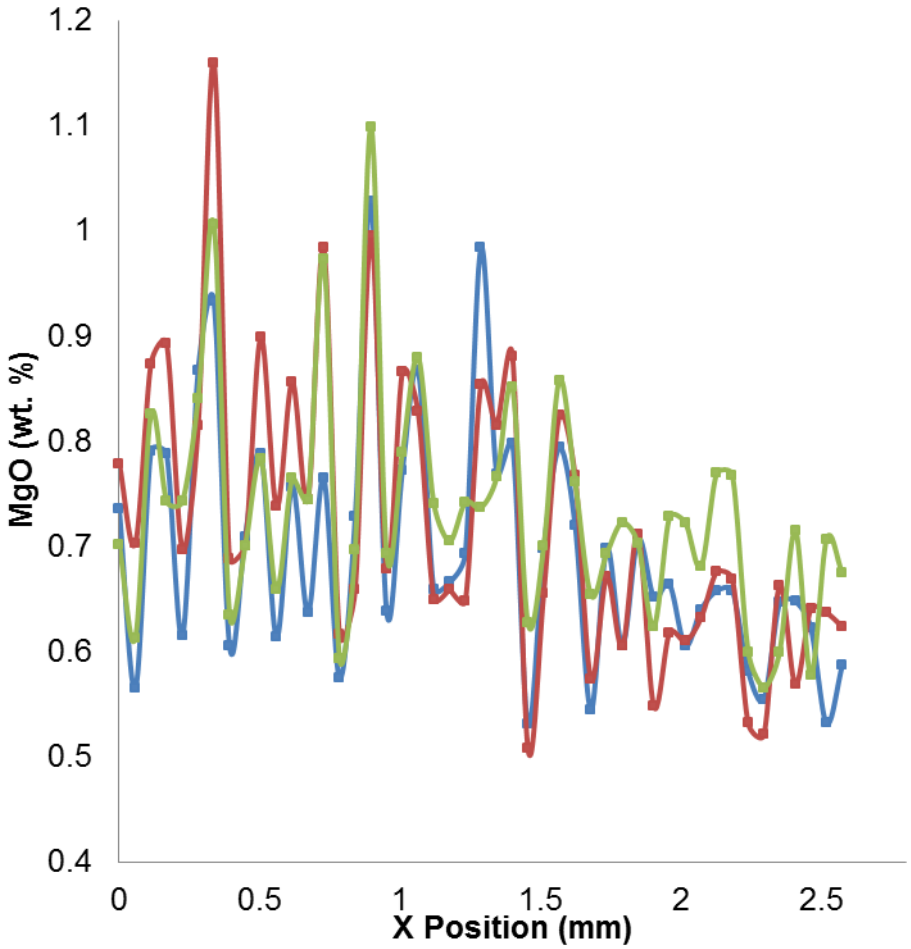

Figure A6.13 Magnesium content parallel to the long axis of a single prism as measured by quantitative wavelength dispersive spectroscopy. Data was measured in a 3 X 47 grid, with 58μm spacing in the x direction and 10μm spacing between the three parallel traces.

A5.4 Discussion

Calcite hardness increases with magnesium content.[6] Prisms from the mollusk *Pinna nobilis* have approximately twice the magnesium content found in *Atrina rigida*, therefore some of the increased hardness of *Pinna nobilis* may be attributed to increased magnesium content over *Atrina rigida.* However, magnesium impurities

alone, cannot account for the absolute hardness of calcite. (Figure A6.14)

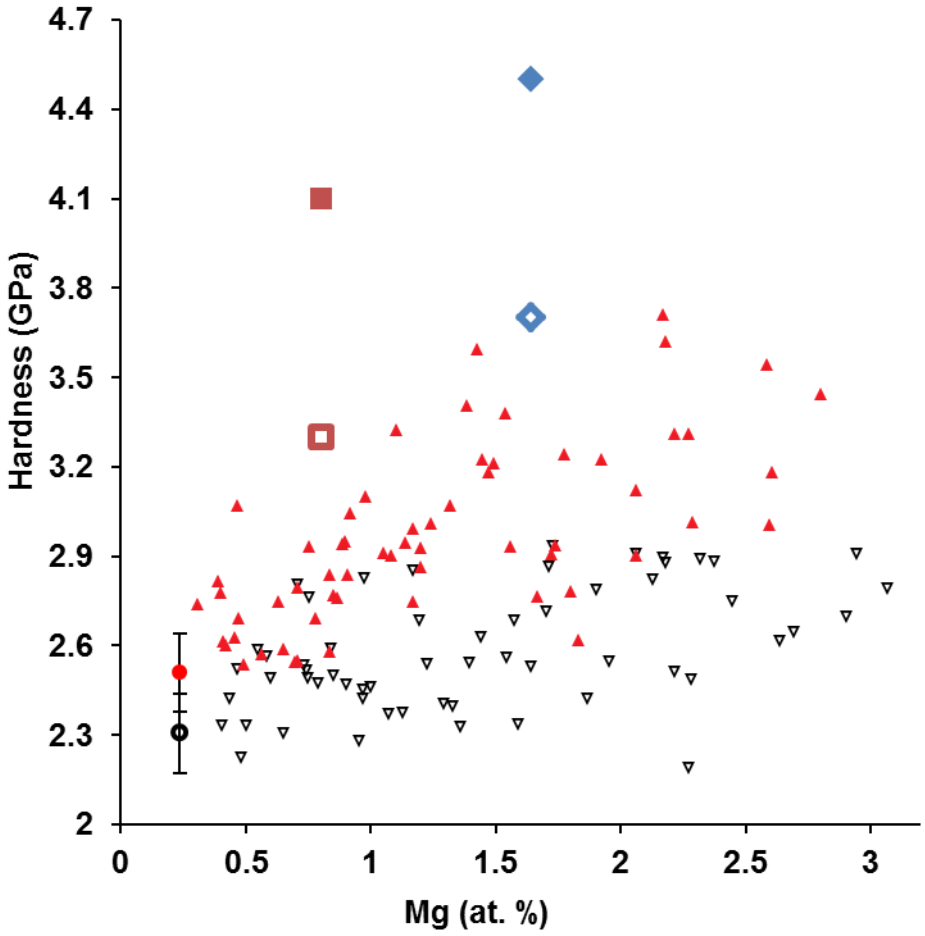

Figure A6.14 Hardness of geologic calcite (circle), magnesium doped synthetic calcite (triangle), *Atrina rigida* (square), and *Pinna nobilis* (diamond) as a function of magnesium content. 0 degree orientations are solid, and 60 degree orientations are hollow.

The zoned distribution of magnesium content within a single prism in *Pinna nobilis* may also result in regions of hard and soft calcite within a single prism. It is unknown at this time whether this magnesium content distribution will affect the overall strength and toughness of the shell. However, further hardness measurements

should be done to quantitatively measure the effect of hardness zoning within a single prism.

1. Pokroy B, Fitch AN, Marin F, Kapon M, Adir N, Zolotoyabko E. Anisotropic lattice distortions in biogenic calcite induced by intra-crystalline organic molecules. *J Struct Biol* 2006, **155**(1)**:** 96-103.

2. Dauphin YD, Cuif JC, Doucet JD, Salomé MS, Susini JS, Williams CW. In situ mapping of growth lines in the calcitic prismatic layers of mollusc shells using X-ray absorption near-edge structure (XANES) spectroscopy at the sulphur K-edge. *Marine Biology* 2003, **142**(2)**:** 299-304.

3. Gilow C, Zolotoyabko E, Paris O, Fratzl P, Aichmayer B. Nanostructure of biogenic calcite crystals: a view by small-angle x-ray scattering. *Cryst Growth Des* 2011, **11**(6)**:** 2054-2058.

4. Kunitake ME, Mangano LM, Peloquin JM, Baker SP, Estroff LA. Evaluation of strengthening mechanisms in calcite single crystals from mollusk shells. *Acta Biomater* 2013, **9**(2)**:** 5353-5359.

5. Turner FJ, Griggs DT, Heard H. Experimental deformation of calcite crystals. *Geol Soc Am Bull* 1954, **65**(9)**:** 883-933.

6. Kunitake ME, Baker SP, Estroff LA. The effect of magnesium substitution on the hardness of synthetic and biogenic calcite. *MRS Communications* 2012, **2**(03)**:** 113-116.